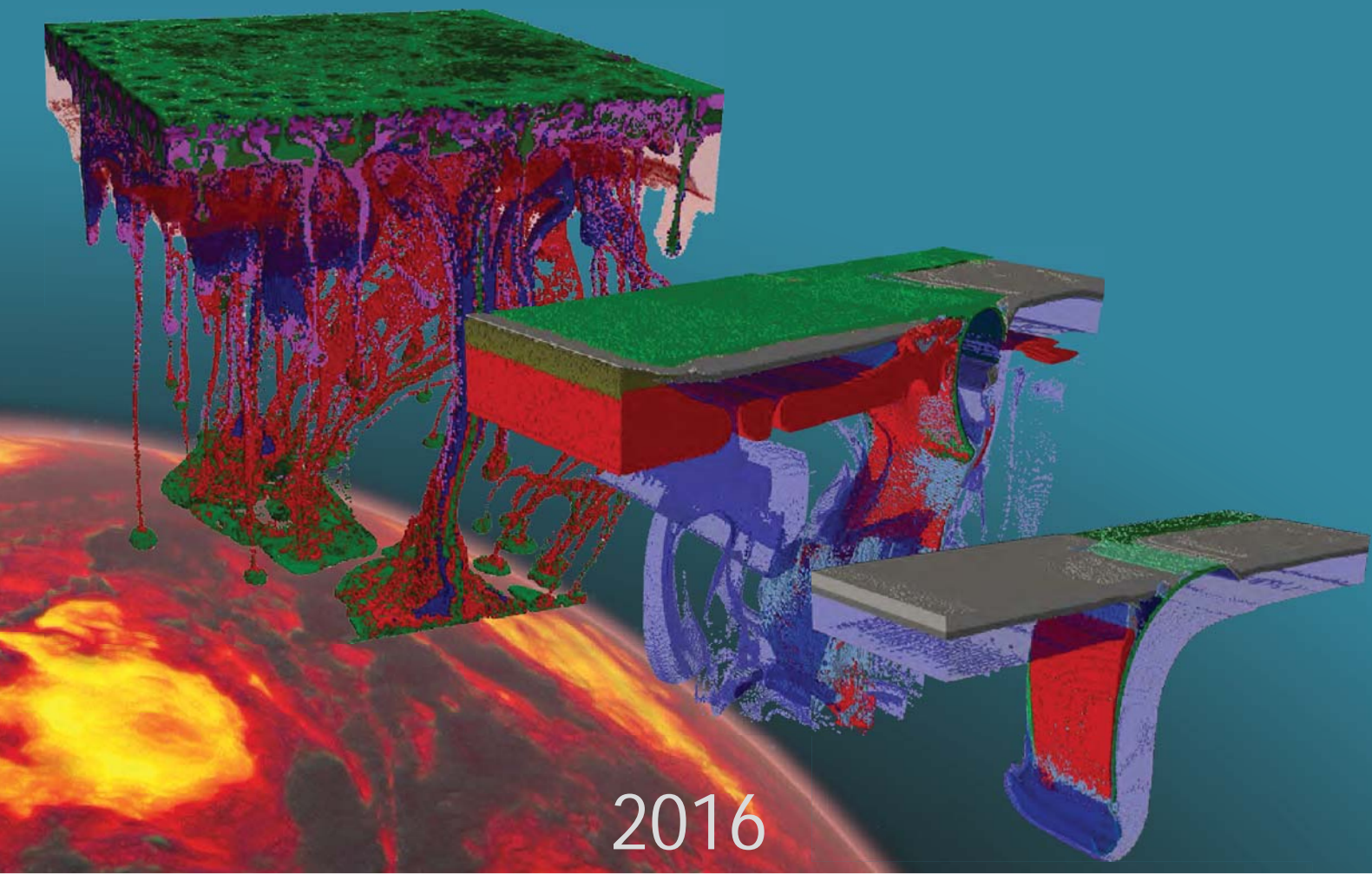


DISS. ETH NO. 23337

From early Earth plume-lid tectonics to present-day plate tectonics: A high-resolution 3D numerical modelling approach

Ria Fischer



Artist's impression of exoplanet 55 Cancri e.
Credit: ESA/Hubble (M. Kornmesser)

Diss. ETH No. 23337

From early Earth plume-lid tectonics to present-day plate tectonics: A high-resolution 3D numerical modelling approach

A thesis submitted to attain the degree of
DOCTOR OF SCIENCES of ETH ZURICH
(Dr. sc. ETH Zurich)

presented by

RIA FISCHER

MSc ETH Earth Sc, ETH Zurich, Switzerland

born on 11th July 1985

citizen of Bäretswil ZH - Switzerland

accepted on the recommendation of

Prof. Dr. Taras Gerya, examiner

Prof. Dr. Paul Tackley, co-examiner

Dr. Jeroen van Hunen, co-examiner

2016

Contents

List of figures	vi
List of tables	vii
Abstract	ix
Kurzfassung	xi
1 Introduction	1
1.1 The plate tectonics system	1
1.2 Precambrian tectonics	3
1.2.1 Short outline of the formation of planet Earth	3
1.2.2 Time-temperature relationship and secular cooling	4
1.2.3 The Precambrian rock record	5
1.2.4 Necessity of a new paradigm	7
1.2.5 Previous work done	8
1.2.6 Scientific and economic value	9
1.3 Thesis structure	10
2 Numerical techniques	17
2.1 I3ELVIS code	17
2.2 Governing conservation equations	18
2.3 Initial and boundary conditions	19
2.4 Modelling of erosion and sedimentation	20
2.5 Modelling of dehydration, hydration and water transport	20
2.6 Modelling of melting and crustal growth	21
2.7 Density changes due to phase transitions and mantle depletion	23
2.8 Rheological model	24
2.9 Abbreviations and units	28
3 Regimes of subduction and lithospheric dynamics in the Precambrian	33
3.1 Introduction	34
3.2 Methods	36
3.2.1 Model design	36
3.2.2 Variations in the mantle temperature	42
3.2.2.1 Development of the mantle geotherm during Earth history	42
3.2.2.2 Reference model series	42
3.2.3 Numerical constraints and setup dependencies	44
3.3 Results	44
3.3.1 Reference model for present-day subduction ($\Delta T_p = 0$ K)	44

3.3.2	Influence of mantle potential temperature increase ΔT_p	50
3.3.2.1	Variations in the retreating speed of the subducting slab and trench	50
3.3.2.2	Variations in slab geometry and behaviour	52
3.3.2.3	Variations in geometry and composition of the accretionary prism	54
3.3.2.4	Variations in geometry and composition of the forearc region	56
3.3.2.5	Variations in arc and backarc region	57
3.3.2.6	Relationship between fluid-fluxed and decompression mantle melting	58
3.3.2.7	Variations in volume and composition of newly formed crust	60
3.3.2.8	Variation in structural behaviour of the crust and mantle lithosphere	61
3.3.2.9	Variations in the mantle flow pattern	62
3.4	Discussion	64
3.4.1	Geodynamic regimes of subduction and lithospheric dynamics in numerical experiments	64
3.4.1.1	Regime I: Present-day subduction $\Delta T_p = 0$ K	64
3.4.1.2	Regime II: Dripping subduction $\Delta T_p = 50 - 100$ K	64
3.4.1.3	Regime III: Transitional mode $\Delta T_p = 150 - 200$ K	65
3.4.1.4	Regime IV: Plume-lid tectonics $\Delta T_p > 200$ K	66
3.4.2	Linking temperature and plate strength	67
3.4.3	Consequences of wide-spread mantle-derived magmatism	68
3.4.4	Formation of small plates	69
3.4.5	Slab break-off and initiation of cold downwellings	69
3.4.6	Factors inhibiting the subduction process	70
3.4.7	The onset of subduction	71
3.4.8	Setup dependencies and model limitations	72
3.5	Conclusion	73
	Supplementary materials	74
4	Early Earth plume-lid tectonics	91
4.1	Introduction	92
4.2	Methods	94
4.2.1	Model design	94
4.2.2	Reference model series	97
4.3	Results	99
4.3.1	Reference model <i>D100b</i>	99
4.3.2	Influence of eruption efficiency χ_{volc}	101
4.3.3	Influence of felsic crust	105
4.3.4	Influence of melt-induced weakening	110
4.3.5	Influence of layered crust	112

4.4 Discussion	118
4.4.1 Magmatic processes, short-term crustal thickening and over-turn, crustal tectonics	118
4.4.2 Crustal thickening, destabilisation and recycling into the mantle . . .	119
4.4.3 Long-term tectonic processes	119
4.4.4 Mantle convection patterns and lithospheric growth	120
4.4.5 PT-conditions for generation of TTG-crust	122
4.4.6 Consequences for subduction initiation	124
4.5 Conclusion	124
Supplementary materials	125
5 Evolution of TTG source regions in plume-lid tectonics	133
5.1 Introduction	133
5.2 Methods	134
5.3 Results and discussion	136
5.3.1 Occurrence of mafic hydrated partial melt and TTG source regions .	136
5.3.2 Distribution of TTG source regions into distinct PT-windows	137
5.3.3 Interpretation of TTG source region development with regard to geo- dynamic model development	139
5.4 Conclusion	143
6 Conclusion and outlook	145
6.1 Main achievements	145
6.2 Areas of future research	147
6.2.1 Implementation of felsic crust formation in I3ELVIS	147
6.2.2 Outlook II: Refertilisation of depleted mantle by delamination of eclogite	149
6.2.3 Outlook III: Long-term global models	150
Acknowledgements	153
Curriculum Vitae	155

List of Figures

1.1	Hutton unconformity	1
1.2	Wilson cycle	2
1.3	MgO-age-temperature relationship	4
1.4	Distribution of Archean and Hadean rocks	5
1.5	Dome-and-keel structure	6
2.1	Flow chart for I3ELVIS code	17
2.2	3D staggered grid stencil	18
2.3	Available material types and their colour code	25
3.1	Top view of the subduction model setup	37
3.2	Initial subduction model setup	38
3.3	Imposed side boundary conditions in the subduction setup	39
3.4	Temperature profiles for the subduction reference models	43
3.5	Evolution of the model <i>A0</i> (reference model)	46
3.6	Evolution of the model <i>A2</i>	47
3.7	Evolution of the model <i>A5</i>	48
3.8	Evolution of the model <i>A6</i>	49
3.9	Observations of trench retreat at different ΔT_p	50
3.10	Variation of the slab geometry with increasing ΔT_p	52
3.11	Variation of the viscosity with increasing ΔT_p	53
3.12	Variation of accretionary prism and mantle wedge with increasing ΔT_p	55
3.13	Development of melt volume with time at different ΔT_p	58
3.14	Volume of newly formed crust with time at different ΔT_p	59
3.15	Evolution of the passive margin with increasing ΔT_p	61
3.16	Mantle flow patterns for different ΔT_p	63
3.17	Effective viscosity profiles for continental and oceanic lithosphere	67
3.18	Summary of the occurring regimes at different ΔT_p	70
3.19	Sketch of Precambrian tectonics	71
3.S1	Evolution of melting for model <i>A0</i> (reference model)	75
3.S2	Evolution of melting for model <i>A2</i>	76
3.S3	Evolution of melting for model <i>A5</i>	77
3.S4	Evolution of melting for model <i>A6</i>	78
3.S5	Evolution of the model <i>B4h</i>	79
3.S6	Evolution of melting for model <i>B4h</i>	80
3.S7	Evolution of topography for model <i>A0</i> (reference model)	81
3.S8	Evolution of topography for model <i>A2</i>	81
3.S9	Evolution of topography for model <i>A5</i>	82
3.S10	Evolution of topography for model <i>A6</i>	82
3.S11	Marker volume change for solid rock types	83
3.S12	Marker volume change for fluid rock types	84

4.1	Initial plume-lid tectonics model setup	95
4.2	Evolution of the model <i>D100b</i> (reference model)	100
4.3	Evolution of the model <i>D0b</i>	102
4.4	Evolution of the model <i>D20</i>	103
4.5	Evolution of the model <i>D100b</i>	107
4.6	Evolution of the model <i>B100b</i>	108
4.7	Viscosity, temperature and density evolution of the model <i>B100b</i> . . .	109
4.8	Comparison between models with and without melt-induced weakening	110
4.9	Evolution of the model <i>D100</i>	111
4.10	Evolution of the model <i>C20</i>	115
4.11	Evolution of the model <i>A20</i>	116
4.12	Evolution of the model <i>B20</i>	117
4.13	Mantle convection patterns	121
4.14	TTG-source regions	122
5.1	PT-conditions for TTG source melt	135
5.2	Volume of partially molten hydrated basalt and TTG source regions . .	138
5.3	Stacked percentages of HP/MP/LP TTG source regions	141
5.4	Stacked percentages of TTG source regions for reference models	142
6.1	Implementation of felsic crust formation in I2ELVIS	148
6.2	Mantle refertilisation by eclogite dripping	149

List of Tables

2.1	Abbreviations and units	28
3.1	Material properties, rheology and melting model for subduction models .	41
3.2	List of all subduction reference models <i>A0</i> to <i>A6</i>	42
3.S1	Full list of all subduction models	74
4.1	Material properties, rheology and melting model for plume-lid tectonics models	98
4.2	List of all plume-lid tectonics reference models	99
4.S1	Material properties, rheology and melting model for alternative plume- lid tectonics models	125

Abstract

“The present is the key to the past” is taught to every geology student around the globe. This view of uniformitarianism holds up well when explaining the concept of modern geodynamics and the paradigm of plate tectonics. However, geological-geochemical evidence points towards higher mantle potential temperature and a different type of tectonics in the early Earth compared to present day. The directly accessible surface rock record of the Precambrian age is sparse and geophysical data is unavailable, which amplifies the role of quantitative geodynamic modelling approaches for the integration of observational constraints from a wide range of disciplines in order to further our understanding of Precambrian geodynamics. One could therefore say that “Intuition and modelling is the key to the past”.

In this context the three questions which are most strongly debated are (1) the timing, onset mechanism and further development of subduction, (2) the predominant tectonic style in the early (Archean) Earth and (3) the timing and mechanism of the formation of continents or felsic crust. To answer these important questions we conduct two series of 3D high-resolution petrological-thermomechanical numerical modelling experiments. The first model series features a subduction setup with compressional side boundary conditions for oceanic plate subduction under an active continental margin at a wide range of mantle potential temperature T_p ($\Delta T_p = 0 - 250$ K, compared to present-day conditions). A second model series features a plume-lid setup with no external forcing but an initial thermal perturbation, giving rise to mantle convection and tectono-magmatic plume-lithosphere interactions. Mantle potential temperature is set to a high value of $\Delta T_p = 250$ K and crustal composition is varied for different experiments. Results from the subduction setup can be roughly divided into four different regimes. For $\Delta T_p = 0 - 50$ K numerical experiments correspond to modern-style subduction. For $\Delta T_p = 50 - 100$ K a regime of dripping subduction emerges which is still very similar to present-day subduction but is characterised by frequent dripping from the slab tip and a loss of coherence of the slab, suggesting a close relationship between dripping subduction and episodic subduction. At further increasing $\Delta T_p = 150 - 200$ K dripping subduction is observed together with unstable dripping lithosphere which corresponds to a transitional regime. For $\Delta T_p > 200$ K we found that subduction is no longer possible and model evolution is driven by intense tectono-magmatic plume-lithosphere interactions instead. Even though the initial setup is still defined by present-day subduction, this final regime shows many characteristics of plume-lid tectonics. We conclude that tectonics, starting out from plume-lid tectonics,

evolved gradually into what we can observe today as plate tectonics and subduction. Therefore it is very likely that no abrupt geodynamic regime transition point can be specified.

Results from the plume-lid setup show two distinct phases in coupled crust-mantle evolution: (1) A longer (80 – 100 Myr) and relatively quiet ‘growth phase’ which is marked by growth of crust and lithosphere, followed by (2) a short (~ 20 Myr) and catastrophic ‘removal phase’ where unstable parts of the crust and mantle lithosphere are removed by eclogitic dripping and later delamination. We therefore conclude that the early Earth plume-lid tectonic regime followed a pattern of episodic growth and removal also called episodic overturn with a periodicity of ~ 100 Myr.

Further detailed analysis of the plume-lid tectonics models suggests a conclusion concerning the potential of the formation of different types of TTGs. We have assessed the potential source regions of low-, medium- and high-pressure TTGs according to their PT-conditions, assuming mafic hydrate partially molten crust as source melt. Results of the detailed model analysis suggest that TTGs mainly form during the overturn event and values for percentages of source regions during the overturn event come close to natural values. We therefore conclude that TTGs are produced in a plume-lid tectonics setup during overturn phases and in pulses of ~ 100 Myr.

Kurzfassung

“Die Gegenwart ist der Schlüssel zur Vergangenheit” wird jedem Geologiestudenten rund um den Erdball beigebracht. Dieses Aktualitätsprinzip funktioniert gut zur Erklärung des Konzepts der modernen Geodynamik und des Paradigmas der Plattentektonik. Geologische und geochemische Anhaltspunkte weisen jedoch auf eine höhere potentielle Manteltemperatur und eine andere Art von Tektonik in der frühen Erde hin. Direkt zugängliches präkambrisches Oberflächengestein ist selten und geophysikalische Daten für das Präkambrium fehlen. Quantitative geodynamische Modellierungsansätze für die Integration von Beobachtungen aus einer breiten Palette von Disziplinen spielen eine verstärkte Rolle zum tieferen Verständnis der präkambrischen Geodynamik. Man könnte deshalb auch sagen: “Intuition und Modellierung ist der Schlüssel zur Vergangenheit”.

Die in diesem Zusammenhang am häufigsten aufgeworfenen Fragen betreffen (1) den Stil, sowie den Mechanismus zum Einsatz und der weiteren Entwicklung der Subduktion, (2) den vorherrschenden tektonischen Stil in der frühen (Archaischen) Erde und (3) die zeitliche Regulierung und den Mechanismus zur Bildung von Kontinenten und felsischer Kruste. Zur Beantwortung dieser Fragen haben wir zwei Serien von hochauflösend petrologisch-thermomechanischen numerischen 3D-Modellen durchgeführt. Die erste Modellserie bietet ein Subduktionssetup mit seitlichen Druck-Randbedingungen für die Subduktion einer ozeanischen Platte unter einen aktiven Kontinentalrand mit einer breiten Palette von potentiellen Manteltemperaturen T_p ($\Delta T_p = 0-250$ K, im Vergleich zur Gegenwart). Eine zweite Modellserie untersucht ein Plume-Lid-Setup ohne externe Krafteinwirkung dafür mit einer thermischen Anfangsperturbation, die zur Bildung von Mantelkonvektion und tektono-magmatischer Plume-Lithosphäreinteraktion führt. Die potentielle Manteltemperatur ist auf einem hohen Wert von $\Delta T_p = 250$ K fixiert und stattdessen wird in verschiedenen Modellen die Zusammensetzung der Kruste variiert. Resultate des Subduktionssetups können grob in vier unterschiedliche Regimes unterteilt werden. Für $\Delta T_p = 0 - 50$ K entsprechen die numerischen Modelle der modernen Subduktion. Für $\Delta T_p = 50 - 100$ K bildet sich ein Regime der Abtropfungssubduktion aus, das immer noch starke Ähnlichkeit aufweist mit der modernen Subduktion, jedoch ausgezeichnet wird durch häufiges Abtropfen von der Slabspitze und einem Verlust der Bindigkeit des Slabs, was einen engen Zusammenhang zwischen Abtropfungssubduktion und episodischer Subduktion nahelegt. Bei einem weiteren Anstieg der Manteltemperatur $\Delta T_p = 150 - 200$ K tritt Abtropfungssubduktion auch zusammen mit instabiler, abtropfender Lithosphäre auf, was hier als Übergangsregime bezeichnet

wird. Für $\Delta T_p > 200$ K fanden wir, dass Subduktion nicht mehr möglich ist und die weitere Entwicklung des Modells stattdessen durch intensive tektono-magmatische Plume-Lithosphäreinteraktion angetrieben wird. Obwohl die Anfangsbedingungen immer noch ein Subduktionssetup vorschreiben, zeigt dieses letzte Regime viele Charakteristika der Plume-Lid-Tektonik. Wir folgern deshalb, dass Tektonik, angefangen bei Plume-Lid-Tektonik, sich sukzessive entwickelt hat zu der Art von Plattentektonik und Subduktion, die heute beobachtet werden kann. Deshalb lässt sich wahrscheinlich auch kein abrupter Übergangspunkt zwischen den geodynamischen Regimen finden.

Resultate des Plume-Lid-Setups zeigen zwei eigenständige Phasen der gekoppelten Krusten-Mantel-Entwicklung: (1) Eine längere (80 – 100 Myr) und relativ ruhige ‘Wachstumsphase’, die gekennzeichnet ist durch Wachstum von Kruste und Lithosphäre. Gefolgt von (2) einer kürzeren (~ 20 Myr) und katastrophalen ‘Abtragungsphase’ wo instabile Teile der Kruste und der Mantellithosphäre durch eklogitische Abtropfungen und später Delamination entfernt werden. Deshalb folgern wir, dass das Regime der Plume-Lid-Tektonik in der frühen Erde ein Muster von episodischem Wachstum gefolgt von episodischer Abtragung zeigt, häufig auch episodische Kippung (‘episodic overturn’) genannt, mit einer Periodizität von ~ 100 Myr.

Weiterführende detaillierte Analysen der Plume-Lid-Tektonik-Modelle schlagen eine Schlussfolgerung bezüglich dem Potential zur Bildung verschiedener Typen von TTGs vor. Wir haben die potentiellen Quellenregionen von Niedrig-, Mittel- und Hochdruck-TTGs entsprechend ihren PT-Bedingungen analysiert, unter der Annahme dass mafische, hydratisierte Schmelze als Quelle fungiert. Resultate der detaillierten Modellanalysen weisen daraufhin, dass TTGs mehrheitlich während der Kippungsphase gebildet werden und Prozentwerte für Quellregionen kommen Messwerten sehr nahe. Wir folgern deshalb, dass TTGs in einem Plume-Lid-Tektonik-Setup während der Kippungsphase und in Pulsen von ~ 100 Myr gebildet wurden.

Chapter 1

Introduction

1.1 The plate tectonics system

In the late 18th century, the celebrated Scottish geologist James Hutton, father of modern geology, introduced the idea of uniformitarianism. He understood that the land we see today (Fig. 1.1) was shaped by various processes which will continue to act in the same manner (Hutton, 1788). In the early 19th century Sir Charles Lyell rephrased this idea into what is still taught to geology students all around the globe, “The present is the key to the past”. This uniformitarian view holds up well when explaining modern geodynamics and the successful paradigm of plate tectonics.

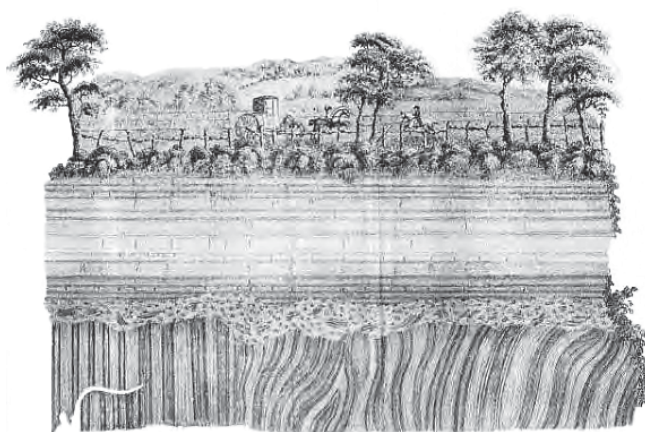


Figure 1.1: Hutton unconformity at Jedburgh, Scotland (Hutton, 1788).

Alfred Wegener was the first to introduce a global dynamic system with the ‘Continental Drift’ hypothesis (Wegener, 1912). He noticed that the continents and shelf areas in their present form would fit together quite well, forming one large supercontinent, which he called Gondwanaland. To support this revolutionary claim of moving continents he also went on several expeditions to Greenland studying fauna, flora and geology. From there he concluded that several landmasses which are split by sea today have similar fauna, flora, geology and even coastline, and must have been in one piece (Wegener, 1912).

Following Wegener several researchers helped to put together the plate tectonics paradigm. The outer shell of the Earth, the lithosphere, is broken up into several thin rigid plates. There are two different types of plates. Continental plates have a lower density granitic crust whereas oceanic plates have a higher density basaltic crust. These plates float on the hot plastic asthenosphere.

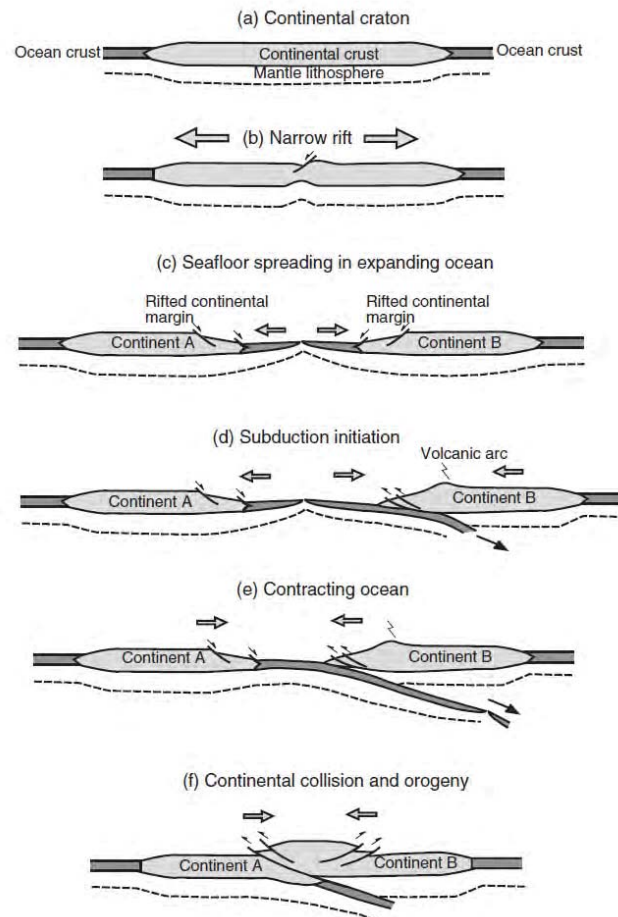


Figure 1.2: Wilson cycle (Kearey et al., 2009).

In 1965 and 1966 Tuzo Wilson described what became known as the Wilson cycle: The global recycling of oceanic crust and continent formation. A general form of the Wilson cycle is shown in Fig. 1.2. At first, rifting starts at the centre of a continental craton (Fig. 1.2a). The continent breaks up into pieces forming a new seafloor and spreading centre (Fig. 1.2b). At the spreading centre new oceanic crust is formed continually (Fig. 1.2c). After further seafloor spreading and expanding of the ocean basin, the direction of movement of continent B is reversed (e.g. due to an adjacent

plate) and subduction is initiated at the former passive continental margin (Fig. 1.2d). The oceanic crust is subducted below the continental crust, closing the oceanic basin in the process (Fig. 1.2e). When all of the oceanic crust is subducted, the two continents collide as they are both unsubductable and form an orogen (Fig. 1.2f).

Paleomagnetic plate reconstructions confirm the existence of a supercontinent, named Pangea, at ~ 260 Ma. Combining paleomagnetic data, sea level changes, biotic diversification and the record of detrital zircons, several distinct peaks appear which are interpreted as times of supercontinent assembly: Superia and Sclavia formed at 2.7 – 2.4 Ga, Nuna at 2.1 – 1.7 Ga, Rodinia at 1.3 – 0.95 Ga, Gondwana at 0.7 – 0.5 Ga and Pangea at 0.35 – 0.18 Ga (Nance et al., 1988, 2014; Cawood et al., 2013).

1.2 Precambrian tectonics

The current Phanerozoic eon (541 – 0 Ma) receives its name due to its abundant plant and animal life starting with the Cambrian explosion. Life was already present in the Precambrian era (4.6 – 0.5 Ga) but less prevalent. The Precambrian is roughly divided into Hadean (4.6 – 4.0 Ga), Archean (4.0 – 2.5 Ga) and Proterozoic (2.5 – 0.5 Ga).

1.2.1 Short outline of the formation of planet Earth

Earth was formed from matter which was previously dispersed in the solar nebula. Giant impact events, e.g. the moon-forming event (Canup, 2004), added a tremendous amount of energy to the early Earth (Jaupart et al., 2007). Another important heat source was the initially higher concentration in radiogenic elements mainly U, Th and K (Wasserburg et al., 1964; Jaupart et al., 2007). The following gravitational core-mantle differentiation and crystallisation of the inner core present further heat sources (Jaupart et al., 2007). The moon-forming giant impact led to a period of fully molten surface, the magma ocean (Jaupart et al., 2007; Elkins-Tanton, 2012). However, the magma ocean must have already started to crystallise at 4.4 Ga (Elkins-Tanton, 2012). With further cooling, the magma ocean fully crystallised and during this continuous process of cooling the crust was formed and the mantle solidified and started to convect by solid state creep. At some point during further cooling subduction processes and plate tectonics must have initiated.

1.2.2 Time-temperature relationship and secular cooling

If the adiabatic mantle gradient is elongated to the surface, this surface temperature is defined as the mantle potential temperature T_p . From petrological constraints, its value can be estimated by measuring the composition of mid-ocean ridge basalts (MORB) (McKenzie and Bickle, 1988) and is found to be between 1280 – 1400 °C (Herzberg et al., 2007, and references therein). In places of hot mantle upwelling such as Hawaii or Iceland the mantle potential temperature can easily be increased by 200 – 300 °C (Herzberg et al., 2007, and references therein). In basaltic lavas a relationship between MgO content and mantle potential temperature exists, meaning that with increasing MgO content, T_p is increasing as well (Herzberg et al., 2007, 2010). Modern MORB crust contains 10 – 13 % of MgO, whereas hot spot and plateau basalts erupting from hotter mantle show a higher MgO content of 18 – 19 % Herzberg et al. (2010).

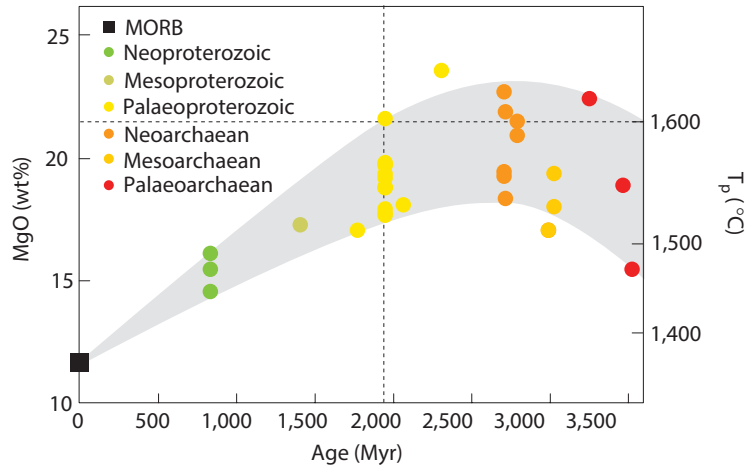


Figure 1.3: MgO-age-temperature relationship (Fig. by Johnson et al., 2014 with data by Herzberg et al., 2010).

Following this line of thought and assuming the relationship between MgO content and age given in Fig. 1.3, a maximum $T_p = 1500 - 1600$ °C is found at ~ 3 Ga (Herzberg et al., 2010; Johnson et al., 2014) for Archean ambient mantle. However, some Archean ultramafic lavas known as komatiites can have an MgO content of 27 – 30 % requiring a potential temperature of 1700 – 1900 °C (Herzberg et al., 2007). It is unclear whether ambient Archean mantle temperature ever reached such high temperatures or komatiites were formed in mantle plumes with an excess temperature of up to ~ 250 °C (Herzberg et al., 2007; Jaupart et al., 2007).

Estimates for T_p before 3.0 Ga are usually highly uncertain because they depend either on the assumed tectonic style for numerical thermal evolution models (Labrosse et al., 2007; Korenaga, 2008) or the assumed petrology and the rock record for petrological models (Herzberg et al., 2007, 2010).

1.2.3 The Precambrian rock record



Figure 1.4: Distribution of Archean and Hadean rocks (Condie, 2005).

Major outcrops of Precambrian rocks are mainly found in cratons and continental shields (see Fig. 1.4). A craton is defined as a segment of continental crust that has attained and maintained long-term stability with tectonic reworking being confined to its margins. Although there is no strict age connotation in this definition, e.g. some segment of crust could have attained ‘cratonic’ stability during Proterozoic time, the term is typically applied to stable segments of Archean crust. Long-term stability is thought to be a function of thicker, stronger lithosphere, involving a cool but compositionally buoyant keel of Fe-depleted upper mantle (Jordan, 1978, 1988). Examples of cratons (mainly Archean age) are the Slave province in Canada (Bleeker et al., 1999), the Pilbara craton in Australia (Collins et al., 1998; Hickman, 2004; Van Kranendonk et al., 2004) or the Kaapvaal craton in South Africa.

Granite-greenstone terrains (GGT) are a general structural element in cratons. Greenstones form circular networks (Van Kranendonk et al., 2004) or winding belts of tholeiitic basalts and komatiites, often accompanied by metasediments and banded iron formations (Bleeker et al., 1999). For most cratons a felsic basement comprised of tonalite-

trondhjemite-granodiorite (TTG) has been shown (e.g. Slave province: Bleeker et al. (1999), Pilbara craton: Van Kranendonk et al. (2004), Kaapvaal craton: Kisters and Anhaeusser (1995); Van Kranendonk (2011a)). This basement usually shows a characteristic dome-and-keel structure with large TTG domes intruding into the overlying greenstone cover (Hamilton, 1998; Van Kranendonk et al., 2004; François et al., 2014). Often several generations of granitoid intrusions can be found, sometimes within one dome with the oldest suit on the outside (Van Kranendonk et al., 2004).

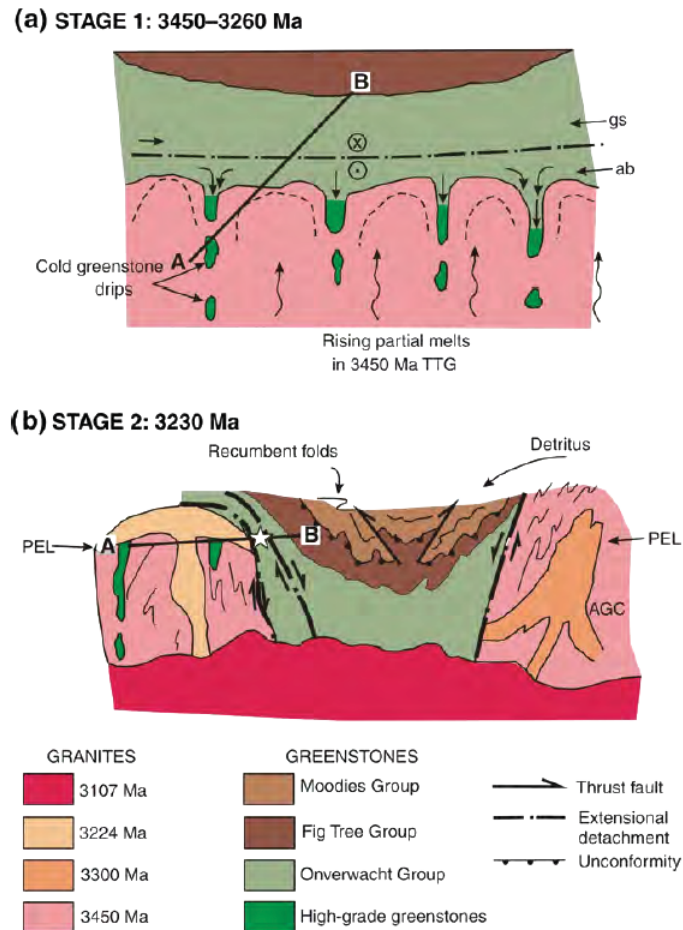


Figure 1.5: Dome-and-keel structure (Van Kranendonk, 2011a).

Several different mechanisms have been proposed to generate these patterns. Many authors discuss the similarities of greenstone belts to modern ophiolite zones both structurally (de Wit, 1998) and chemically (Furnes et al., 2014). This leads to the conclusion that plate tectonics and with it subduction might have been already operable in the Eoarchean or even Hadean (Furnes et al., 2014). Another possibility is the

formation of the TTG domes by diapirism or sagduction (e.g. Hill et al., 1991; Vlaar et al., 1994; François et al., 2014). The layering of mafic greenstones on top of felsic TTGs creates a density instability which results in partial convective overturn (Collins et al. (1998); Van Kranendonk (2011a) and Fig. 1.5). The typical pattern of TTG domes with greenstone belts in-between emerges which is best conserved in the East Pilbara (François et al., 2014). The process of sagduction does not necessarily require active plate tectonics and can therefore be seen as an alternative to an early onset of the subduction process (Hamilton, 1998).

Several different ideas and models have already been proposed to describe Precambrian tectonics. For example it has been suggested that Precambrian Earth and its tectonic style was similar to present-day Venus (e.g. Van Kranendonk, 2010; Harris and Bédard, 2014, 2015). These authors argue that the two planets are relatively similar in many ways, however, Venus has preserved not only a higher surface temperature but also a higher internal temperature due to its closer distance to the sun (Breuer and Moore, 2007). Venusian surface tectonics is marked by an absence of plates and striking coronae and novae features (Gerya, 2014b, and references therein). The common theory is that these features are formed by mantle plumes and that the planet experiences episodic overturn events rather than the style of plate tectonics that we observe at present day (Strom et al., 1994; Armann and Tackley, 2012).

The hypothesis of plume-induced tectonics, plume-lid tectonics, is often invoked for the Precambrian. In this case, tectonic deformation of crust and lithosphere is not produced by plate tectonics and its major driving force, the slab pull force (van Hunen and Mosen, 2012), but by mantle plumes and various other active mantle and crustal upwellings and downwellings. The Archean plume-lid tectonics regime was described by Van Kranendonk (2011b), who suggests a Precambrian geodynamic style (before 3 Ga) with small mobile plates and rapid upper mantle convection. Continental crust is formed by volcanism over upwelling mantle or by imbrication over downwelling mantle (Van Kranendonk, 2011b).

1.2.4 Necessity of a new paradigm

From our present-day understanding of geodynamics we struggle to understand processes older than 0.5 – 1 Ga (Gerya, 2014a, and references therein), such as the for-

mation of cratons or even the dominant tectonic style in the Hadean and Archean. What is needed is a global working paradigm for Archean geodynamics comparable to plate tectonics (Benn et al., 2006). The directly accessible surface rock record of the Precambrian age is sparse and geophysical data is unavailable which amplifies the role of quantitative geodynamic modelling approaches for the integration of observational constraints from a wide range of disciplines in order to further our understanding of Precambrian geodynamics (Gerya, 2014a). Instead of, “The present is the key to the past” one could, therefore, say that “Intuition and modelling is the key to the past”.

In this context, the three questions which are most strongly debated are (1) the timing, onset mechanism and further development of subduction, (2) the predominant tectonic style in the early (Archean) Earth and (3) the timing and mechanism of the formation of continents or felsic crust. To answer these important questions, numerical geodynamic models should be used in addition to restricted natural data (e.g. Vlaar et al., 1994; van Hunen and van den Berg, 2008; Sizova et al., 2010, 2014, 2015; Gerya, 2014a; Gerya et al., 2015; Fischer and Gerya, submitted for publication, and references therein).

1.2.5 Previous work done

Despite the fact that Precambrian crustal deformation processes are typically characterised by three-dimensional mass redistribution (Chardon et al., 2009; Perchuk and Gerya, 2011; François et al., 2014), no 3D numerical modelling studies of Precambrian subduction have been carried out to date. Previous studies focused on 2D numerical models of Precambrian subduction. Van Hunen and van den Berg (2008) found in particular that an increase of 200 – 300 K in the mantle potential temperature T_p leads to episodic subduction interrupted by frequent slab break-off. Sizova et al. (2010) were able to identify several geodynamic regimes mainly depending on mantle potential temperature. They found a transition from ‘no-subduction’ to ‘pre-subduction’ for a mantle 200 – 250 K hotter, where ‘pre-subduction’ is characterised by shallow underthrusting and two-sided lithospheric downwellings. A second transition from ‘pre-subduction’ to present-day subduction was found at 160 – 175 K increased mantle potential temperature.

Johnson et al. (2014) and Sizova et al. (2015) modelled Precambrian plume-lid tectonics in 2D, where they showed that continued melting and dripping of over-thickened crust

under Archean conditions in combination with fractionation could lead to the necessary source magmas for TTG melts. Van Thienen et al. (2005) discussed 2D models of the whole mantle under Archean conditions, concluding that the Archean mantle shows strong heterogeneity and different reservoirs produced by convective instabilities and resurfacing events.

1.2.6 Scientific and economic value

The questions outlined above, briefly summarised by “How did tectonics work in the early Earth?”, are of great importance not only to the geodynamic community but to science in general as they cover no less than 4 out of 10 “Research questions for a changing planet” in the 21st century as listed by DePaolo et al. (2008). The models presented here go back to a time close to the magma ocean stage, investigating the question, “What happened during Earth’s ‘dark age’?”, or at least towards the end of it. Models of the crust and mantle with successively lower mantle temperature will not only address the question, “Why does Earth have plate tectonics and continents?” but also link crustal and mantle dynamics and in turn speak about “How does Earth’s interior work, and how does it affect the surface?”.

This work is even linked, at least indirectly, to the question of “How did life begin?”. The study of earliest lifeforms such as blue-green algae and stromatolites requires detailed knowledge of the dominant geological setting and climate conditions (Westall and Southam, 2013; Shen et al., 2013).

From an economic perspective, Precambrian rocks contain many valuable resources. Greenstone belts are sometimes also referred to as ‘gold belts’ and are host to Cu-Ni-PGM-Au-sulphides (Anhaeusser, 2014). Diamond mines are mainly found in cratons. A better understanding of the structure and formation process of Archean cratons could increase the prospect of finding these important resources.

1.3 Thesis structure

Chapter 2 – Numerical techniques

Chapter 2 describes the numerical code I3ELVIS used in this work as well as the fundamental thermodynamic principals.

Chapter 3 – Regimes of subduction and lithospheric dynamics in the Precambrian

Chapter 3 describes changes in a subduction zone model if it is subjected to higher mantle potential temperature which corresponds to earlier times in the Earth's history.

Chapter 4 – Early Earth plume-lid tectonics

Chapter 4 focuses on the tectonic end-member which was present in the early Earth: plume-lid tectonics. Different crustal compositions and varying magmatic parameters are explored describing the dynamics of plume-lid tectonics.

Chapter 5 – Evolution of TTG source regions in plume-lid tectonics

Chapter 5 discusses the formation of three different types of TTG source regions with regard to PT-conditions in time and possible consequences for the formation of high-, medium- and low-pressure TTGs.

Chapter 6 – Conclusion and outlook

Chapter 6 draws some conclusions and provides an outlook.

References

- C. R. Anhaeusser. Archaean greenstone belts and associated granitic rocks – A review. *Journal of African Earth Sciences*, 100:684–732, 2014.
- M. Armann and P. J. Tackley. Simulating the thermochemical magmatic and tectonic evolution of Venus’s mantle and lithosphere: Two-dimensional models. *Journal of Geophysical Research: Planets*, 117(E12):E12003, 2012.
- K. Benn, J.-C. Mareschal, and K. C. Condie. Introduction: Archean Geodynamics and Environments. In *Archean Geodynamics and Environments*, pages 1–5. American Geophysical Union, 2006.
- W. Bleeker, J. W. Ketchum, V. A. Jackson, and M. E. Villeneuve. The Central Slave Basement Complex, Part I: its structural topology and autochthonous cover. *Canadian Journal of Earth Sciences*, 36(7):1083–1109, 1999.
- D. Breuer and W. B. Moore. Dynamics and Thermal History of the Terrestrial Planets, the Moon, and Io. In S. Gerald, editor, *Treatise on Geophysics*, pages 299–348. Elsevier, Amsterdam, 2007.
- R. M. Canup. Origin of Terrestrial Planets and the Earth–Moon System. *Physics Today*, 57(4):56–62, 2004.
- P. Cawood, C. Hawkesworth, and B. Dhuime. The continental record and the generation of continental crust. *Geological Society of America Bulletin*, 125(1-2):14–32, 2013.
- D. Chardon, D. Gapais, and F. Cagnard. Flow of ultra-hot orogens: A view from the Precambrian, clues for the Phanerozoic. *Tectonophysics*, 477(3-4):5–118, 2009.
- W. Collins, V. Kranendonk, MJ, and C. Teyssier. Partial convective overturn of Archaean crust in the east Pilbara Craton, Western Australia: driving mechanisms and tectonic implications. *Journal of Structural Geology*, 20(9):1405–1424, 1998.
- K. C. Condie. 8 - Crustal and Mantle Evolution. In *Earth as an Evolving Planetary System*, pages 265–VI. Academic Press, Burlington, 2005.
- M. J. de Wit. On Archean granites, greenstones, cratons and tectonics: does the evidence demand a verdict? *Precambrian research*, 91(1):181–226, 1998.
- D. J. DePaolo, T. Cerling, S. Hemming, A. Knoll, F. Richter, L. Royden, R. Rud-

- nick, L. Stixrude, and J. Trefil. Origin and evolution of earth: research questions for a changing planet. *Committee on Grand Research Questions in the Solid-Earth Sciences, Board on Earth Sciences and Resources, Division on Earth and Life Studies, National Research Council of the National Academies, The National Academies Press, Washington, DC, 2008.*
- L. T. Elkins-Tanton. Magma Oceans in the Inner Solar System. *Annual Review of Earth and Planetary Sciences*, 40(1), 2012.
- R. Fischer and T. Gerya. Early Earth plume tectonics: A high-resolution 3D numerical modelling approach. *Journal of Geodynamics*, in press.
- R. Fischer and T. Gerya. Regimes of subduction and lithospheric dynamics in the Precambrian: 3D thermomechanical modelling. *Gondwana Research*, submitted for publication.
- C. François, P. Philippot, P. Rey, and D. Rubatto. Burial and exhumation during Archean sagduction in the East Pilbara Granite-Greenstone Terrane. *Earth and Planetary Science Letters*, 396(0):235–251, 2014.
- H. Furnes, Y. Dilek, and M. de Wit. Precambrian greenstone sequences represent different ophiolite types. *Gondwana Research*, 2014.
- T. Gerya. Precambrian geodynamics: Concepts and models. *Gondwana Research*, 25(2):442–463, 2014a.
- T. V. Gerya. Plume-induced crustal convection: 3D thermomechanical model and implications for the origin of novae and coronae on Venus. *Earth and Planetary Science Letters*, 391:183–192, 2014b.
- T. V. Gerya, R. J. Stern, M. Baes, S. V. Sobolev, and S. A. Whattam. Plate tectonics on the Earth triggered by plume-induced subduction initiation. *Nature*, 527(7577):221–225, 2015.
- W. B. Hamilton. Archean magmatism and deformation were not products of plate tectonics. *Precambrian Research*, 91(1):143–179, 1998.
- L. B. Harris and J. H. Bédard. Crustal evolution and deformation in a non-plate-tectonic Archean Earth: Comparisons with Venus. In *Evolution of Archean Crust and Early Life*, pages 215–291. Springer, 2014.

- L. B. Harris and J. H. Bédard. Interactions between continent-like ‘drift’, rifting and mantle flow on Venus: gravity interpretations and Earth analogues. *Geological Society, London, Special Publications*, 401(1):327–356, 2015.
- C. Herzberg, P. D. Asimow, N. Arndt, Y. Niu, C. M. Lesher, J. G. Fitton, M. J. Cheddle, and A. D. Saunders. Temperatures in ambient mantle and plumes: Constraints from basalts, picrites, and komatiites. *Geochemistry Geophysics Geosystems*, 8(2):n/a–n/a, 2007.
- C. Herzberg, K. Condie, and J. Korenaga. Thermal history of the Earth and its petrological expression. *Earth and Planetary Science Letters*, 292(1–2):79–88, 2010.
- A. Hickman. Two contrasting granite-greenstone terranes in the Pilbara Craton, Australia: evidence for vertical and horizontal tectonic regimes prior to 2900Ma. *Precambrian Research*, 131(3):153–172, 2004.
- R. I. Hill, I. H. Campbell, and R. W. Griffiths. Plume Tectonics and the Development of Stable Continental Crust. *Exploration Geophysics*, 22(1):185–188, 1991.
- J. Hutton. Theory of the Earth; or an Investigation of the Laws observable in the Composition, Dissolution, and Restoration of Land upon the Globe. *Earth and Environmental Science Transactions of the Royal Society of Edinburgh*, 1(02):209–304, 1788.
- C. Jaupart, S. Labrosse, and J. C. Mareschal. 7.06 - Temperatures, Heat and Energy in the Mantle of the Earth. In G. Schubert, editor, *Treatise on Geophysics*, chapter 7, pages 253–303. Elsevier, Amsterdam, 2007.
- T. E. Johnson, M. Brown, B. J. P. Kaus, and J. A. VanTongeren. Delamination and recycling of Archaean crust caused by gravitational instabilities. *Nature Geoscience*, 7(1):47–52, 2014.
- T. H. Jordan. Composition and development of the continental tectosphere. *Nature*, 274(5671):544–548, 1978.
- T. H. Jordan. Structure and Formation of the Continental Tectosphere. *Journal of Petrology*, Special Volume(1):11–37, 1988.
- P. Kearey, K. A. Klepeis, and F. J. Vine. *Global tectonics*. John Wiley and Sons, 2 edition, 2009.

- A. F. M. Kisters and C. R. Anhaeusser. Emplacement features of Archaean TTG plutons along the southern margin of the Barberton greenstone belt, South Africa. *Precambrian Research*, 75(1–2):1–15, 1995.
- J. Korenaga. Plate tectonics, flood basalts and the evolution of Earth’s oceans. *Terra Nova*, 20(6):419–439, 2008.
- S. Labrosse, J. W. Hernlund, and N. Coltice. A crystallizing dense magma ocean at the base of the Earth’s mantle. *Nature*, 450(7171):866–869, 2007.
- D. McKenzie and M. J. Bickle. The Volume and Composition of Melt Generated by Extension of the Lithosphere. *Journal of Petrology*, 29(3):625–679, 1988.
- R. D. Nance, T. R. Worsley, and J. B. Moody. The supercontinent cycle. *Scientific American*, 259(1):72–79, 1988.
- R. D. Nance, J. B. Murphy, and M. Santosh. The supercontinent cycle: A retrospective essay. *Gondwana Research*, 25(1):4–29, 2014.
- L. L. Perchuk and T. V. Gerya. Formation and evolution of Precambrian granulite terranes: a gravitational redistribution model. *Geological Society of America Memoirs*, 207:289–310, 2011.
- Y. Shen, D. L. Pinti, and K. Hashizume. Biogeochemical Cycles of Sulfur and Nitrogen in the Archean Ocean and Atmosphere. In *Archean Geodynamics and Environments*, chapter 18, pages 305–320. American Geophysical Union, 2013.
- E. Sizova, T. Gerya, M. Brown, and L. L. Perchuk. Subduction styles in the Precambrian: Insight from numerical experiments. *Lithos*, 116(3–4):209–229, 2010.
- E. Sizova, T. Gerya, and M. Brown. Contrasting styles of Phanerozoic and Precambrian continental collision. *Gondwana Research*, 25(2):522–545, 2014.
- E. Sizova, T. Gerya, K. Stüwe, and M. Brown. Generation of felsic crust in the Archean: A geodynamic modeling perspective. *Precambrian Research*, 271:198–224, 2015.
- R. Strom, G. Schaber, and D. Dawson. The global resurfacing of Venus. *Journal of Geophysical Research*, 99(E5):10,899–10,926, 1994.
- J. van Hunen and J.-F. Moyen. Archean Subduction: Fact or Fiction? *Annual Review of Earth and Planetary Sciences*, 40(1):195–219, 2012.

- J. van Hunen and A. P. van den Berg. Plate tectonics on the early Earth: Limitations imposed by strength and buoyancy of subducted lithosphere. *Lithos*, 103(1–2):217–235, 2008.
- M. J. Van Kranendonk. Two types of Archean continental crust: Plume and plate tectonics on early Earth. *American Journal of Science*, 310(10):1187–1209, 2010.
- M. J. Van Kranendonk. Cool greenstone drips and the role of partial convective overturn in Barberton greenstone belt evolution. *Journal of African Earth Sciences*, 60(5):346–352, 2011a.
- M. J. Van Kranendonk. Onset of Plate Tectonics. *Science*, 333(6041):413–414, 2011b.
- M. J. Van Kranendonk, W. Collins, A. Hickman, and M. J. Pawley. Critical tests of vertical vs. horizontal tectonic models for the Archaean East Pilbara granite–greenstone terrane, Pilbara craton, western Australia. *Precambrian Research*, 131(3):173–211, 2004.
- P. van Thienen, J. van Summeren, R. Van der Hilst, A. Van den Berg, and N. Vlaar. Numerical study of the origin and stability of chemically distinct reservoirs deep in Earth’s mantle. *Geophysical monograph*, 2005.
- N. J. Vlaar, P. E. van Keken, and A. P. van den Berg. Cooling of the earth in the Archaean: Consequences of pressure-release melting in a hotter mantle. *Earth and Planetary Science Letters*, 121(1):1–18, 1994.
- G. J. Wasserburg, J. F. M. Gordon, F. Hoyle, and W. A. Fowler. Relative Contributions of Uranium, Thorium, and Potassium to Heat Production in the Earth. *Science*, 143(3605):465–467, 1964.
- A. Wegener. Die Entstehung der Kontinente. *Geologische Rundschau*, 3(4):276–292, 1912.
- F. Westall and G. Southam. The Early Record of Life. In *Archean Geodynamics and Environments*, chapter 17, pages 283–304. American Geophysical Union, 2013.
- J. T. Wilson. A New Class of Faults and their Bearing on Continental Drift. *Nature*, 207(4995):343–347, 1965.
- J. T. Wilson. Did the Atlantic Close and then Re-Open? *Nature*, 211(5050):676–681, 1966.

Chapter 2

Numerical techniques

2.1 I3ELVIS code

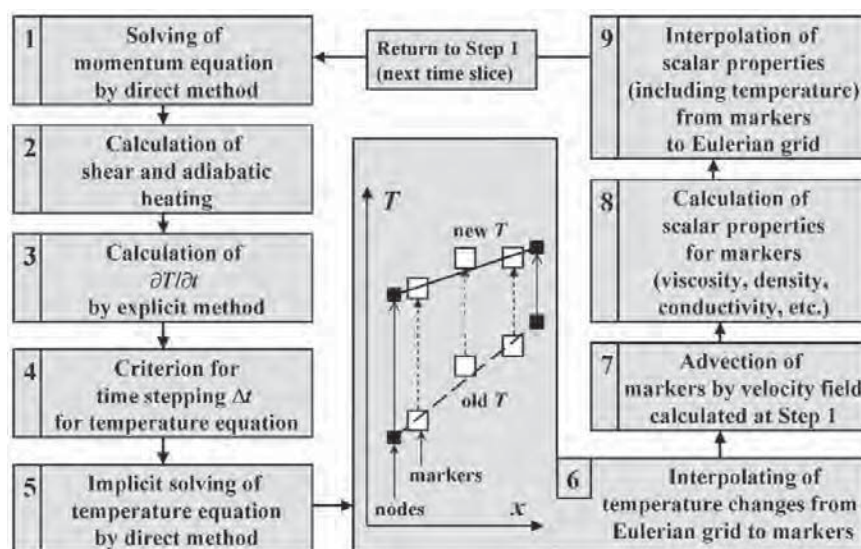


Figure 2.1: Flow chart representing the adopted computational strategy used in the programming of the computer code I3ELVIS. The central panel shows the scheme for interpolating the calculated temperature changes from the Eulerian grid to the moving markers in Step 6 (Gerya and Yuen, 2003).

To model three-dimensional creeping flow under extended Boussinesq approximation with both thermal and chemical buoyancy, the conservative finite-difference code I3ELVIS (Gerya and Yuen, 2003, 2007) as described in Fig. 2.1 is used which operates on a staggered grid (Fig. 2.2) and uses a non-diffusive marker-in-cell approach to simulate multi-phase flow and a multigrid solver (Gerya and Yuen, 2007). All rock types have temperature-, pressure-, strain-rate and melt fraction-dependant viscoplastic rheology and additionally, the 3D code features melting of crustal and mantle rocks and volcanic and plutonic addition of primordial crust from silicate melt, eclogitic phase changes as well as hydration and dehydration (Zhu et al., 2013; Gerya et al., 2015).

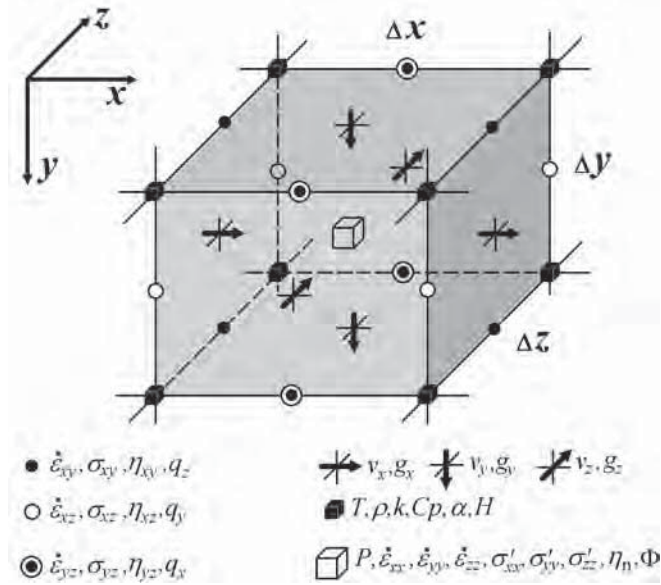


Figure 2.2: Elementary volume (cell) of 3D staggered grid used for discretisation of momentum, continuity, Poisson's and temperature equations in the case of incompressible viscous flow with variable viscosity and thermal conductivity (Gerya, 2010).

2.2 Governing conservation equations

Momentum, mass and heat conservation equation for 3D creeping flow all need to be satisfied simultaneously.

The conservation of momentum is described by the 3D Stokes equation with the extended Boussinesq approximation. Density is assumed to be constant except in the buoyancy force term where temperature and volatile content play an important role and density therefore varies locally as a function of temperature, pressure, composition and melt fraction:

$$\frac{\partial \sigma'_{ij}}{\partial x_j} = \frac{\partial P}{\partial x_i} - g_i \rho(T, P, c, M) \quad (2.1)$$

Conservation of mass is approximated by the incompressible continuity equation:

$$\nabla \cdot \vec{v} = 0. \quad (2.2)$$

The temperature equation satisfies the conservation of energy:

$$\rho C_p \left(\frac{DT}{Dt} \right) = -\nabla \cdot \vec{q} + H_r + H_a + H_s, \quad (2.3a)$$

$$H_r = \text{const. (depends on composition)} \quad (2.3b)$$

$$H_a = T \alpha \vec{v} \nabla P, \quad (2.3c)$$

$$H_s = \sigma'_{ij} \dot{\epsilon}'_{ij}, \quad (2.3d)$$

where heat flux is denoted by $\vec{q} = -k(T, p, c) \nabla T$ with k being the thermal conductivity. H_r, H_a, H_s denote radiogenic, adiabatic and shear heating respectively. Latent heating is included implicitly by means of equilibrium melting/crystallisation which will change the effective heat capacity ($C_{P\text{eff}}$) and the effective thermal expansion (α_{eff}) (Burg and Gerya, 2005; Sizova et al., 2010) of the melting/crystallising rock as follows,

$$C_{P\text{eff}} = C_P + H_L \left(\frac{\partial M}{\partial T} \right)_{P=\text{const}}, \quad (2.4a)$$

$$\alpha_{\text{eff}} = \alpha + \rho \frac{H_L}{T} \left(\frac{\partial M}{\partial P} \right)_{T=\text{const}}, \quad (2.4b)$$

where heat capacity C_P and thermal expansion α denote properties of the solid rock.

2.3 Initial and boundary conditions

A compositional field is inscribed initially which defines a crust which can be either one- or two-layered, of mafic or felsic composition, and of variable thickness. All velocity boundary conditions are free slip. In the subduction setup, compressional side boundary conditions are applied and material is allowed to flow out through the bottom boundary to maintain conservation of volume. The uppermost part of the model domain is filled with ‘sticky air’ which acts as an internal free surface boundary condition (Crameri et al., 2012). The initial temperature structure of the model is adjusted to the increased temperature conditions in the Precambrian (Sizova et al., 2010, 2015; Fischer and Gerya, submitted for publication,i). The mantle has a linear adiabatic temperature gradient of 0.5 K/km and the mantle potential temperature T_p is increased by values between $\Delta T_p = 0-250$ K compared to present-day reference mantle potential temperature $T_p = T_{\text{initial}} = 1556$ K. The crust has a hot initial geotherm

with a fixed temperature of 273 K at the surface and meets the mantle geotherm at depth.

2.4 Modelling of erosion and sedimentation

An instantaneous erosion and sedimentation model is implemented. Rock markers of any type which are found above the erosion level $y_{eroslev}$ are eroded instantaneously and converted to air whereas water markers below the sedimentation layer $y_{sedilev}$ are deposited instantaneously and converted to layered sediments. The sea level is fixed at $y_{waterlev}$.

2.5 Modelling of dehydration, hydration and water transport

The dehydration and mantle hydration model is based on the water markers approach by Gerya and Meilick (2011). The equilibrium mineralogical water content is computed for the crust and the mantle as a function of pressure and temperature from thermodynamic data by free energy minimisation (Connolly, 2005; Gerya and Meilick, 2011). In addition, water is present as pore fluid with concentrations of up to 2 wt% in the upper oceanic crust (basalt). The pore water content $X_{H_2O}(P)$ (wt%) decreases linearly from the maximal value of $X_{H_2O}(P_0) = 2$ wt% at the surface to 0 wt% at 75 km depth:

$$X_{H_2O}(P) = (1 - 0.013 \cdot \Delta y) \cdot X_{H_2O}(P_0), \quad (2.5)$$

where y is depth (0 – 75 km). The pore water release also mimics effects of low-temperature ($T < 573$ K) reactions which are not included in the thermodynamic database (Gerya and Meilick, 2011). The oceanic crust dehydrates as it sinks. The timing of H₂O release by dehydration reactions is determined by the physicochemical conditions of the model and the assumption of thermodynamic equilibrium. Water propagates upwards into the mantle wedge. Water propagation is modelled in the form of water markers: dehydration reactions lead to a release of water, the amount of which is stored in a newly generated water marker. Water markers move through the

rocks with the following velocity:

$$v_{x,water} = v_x, \quad (2.6a)$$

$$v_{y,water} = v_y - v_{y,percolation} \quad (2.6b)$$

v_x and v_y describe the local velocity of the mantle and $v_{y,percolation}$ indicates the relative velocity of upward percolation ($v_{y,percolation} = 10$ cm/yr in our experiments) (Gerya and Meilick, 2011). The water marker releases its water as soon as it encounters a rock capable of absorbing water by hydration or melting reactions at given PT-conditions and rock composition (Gerya and Meilick, 2011).

2.6 Modelling of melting and crustal growth

In order to account for changes in melting conditions (e.g. solidus and liquidus temperatures – $T_{solidus}$ and $T_{liquidus}$) with varying rock composition, four different melting models are used. For sediments and felsic rocks such as dry or hydrated upper continental crust, a granite melting model is applied (Johannes, 1985; Poli and Schmidt, 2002; Gerya et al., 2006):

$$T_{solidus} = \begin{cases} 889 + \frac{17900}{P + 54} + \frac{20200}{(P + 54)^2} & \text{at } P < 1200 \text{ MPa} \\ 831 + 0.06 \cdot P & \text{at } P \geq 1200 \text{ MPa} \end{cases} \quad (2.7a)$$

$$T_{liquidus} = 1262 + 0.09 \cdot P \quad (2.7b)$$

For all hydrated mafic rocks such as upper oceanic crust, hydrated lower continental crust and newly formed volcanic and plutonic rocks, a basalt melting model is applied (Hess, 1989; Schmidt and Poli, 1998; Gerya et al., 2006):

$$T_{solidus} = \begin{cases} 973 + \frac{70400}{P + 354} + \frac{77800000}{(P + 354)^2} & \text{at } P < 1600 \text{ MPa} \\ 935 + 3.5 \times 10^{-3} \cdot P + 6.2 \cdot 10^{-6} \cdot P^2 & \text{at } P \geq 1600 \text{ MPa} \end{cases} \quad (2.8a)$$

$$T_{liquidus} = 1423 + 0.105 \cdot P \quad (2.8b)$$

A gabbro melting model (Hess, 1989; Gerya et al., 2006) is applied to the lower part

of both oceanic and continental crust:

$$T_{solidus} = 1327 + 0.091 \cdot P \quad (2.9a)$$

$$T_{liquidus} = 1423 + 0.105 \cdot P \quad (2.9b)$$

For mantle peridotite in various stages of hydration, a P-T-H₂O-dependent melting model of Katz et al. (2003) is applied:

$$T_{solidus} = 1359 + 0.133 \cdot P - 5.1 \cdot 10^{-6} \cdot P^2 - 43 \cdot (X_{H_2O})^{0.75} \quad (2.10a)$$

$$T_{liquidus} = 2053 + 0.045 \cdot P - 2.0 \cdot 10^{-6} P^2 - 43 \cdot (X_{H_2O})^{0.75} \quad (2.10b)$$

Dry mantle melting is only activated at pressures less than a maximum pressure $P_{max} = 10$ GPa to avoid unrealistic results arising from the melting model extrapolation. See Tables 3.1 and 4.1 for material properties and melting parameters.

For all crustal lithologies, the standard melt fraction is calculated according to a simplified linear melting model (Gerya et al., 2006),

$$M_0 = \begin{cases} 0, & \text{if } T < T_{solidus} \\ \frac{T - T_{solidus}}{T_{liquidus} - T_{solidus}}, & \text{if } T_{solidus} < T < T_{liquidus} \\ 1, & \text{if } T > T_{liquidus} \end{cases} \quad (2.11)$$

where M_0 is the standard volumetric degree of melting before melt extraction. For the mantle, the non-linear melting model of Katz et al. (2003) is used to calculate M_0 . In both crustal and mantle rocks, the actual amount of melt M is defined as the difference between the standard melt fraction M_0 and the amount of previously extracted melt $\sum_n M_{ext}$ which is accumulated for each marker in the course of the model where n is the number of melt extraction episodes,

$$M = M_0 - \sum_n M_{ext}. \quad (2.12)$$

To simulate melt extraction, an extraction threshold M_{max} (see Tables 3.S1 and 3.2) is defined. If the total amount of melt M on a marker surpasses this threshold (i.e.

when $M > M_{max}$) all melt except for a non-extractable part M_{min} (see Tables 3.S1 and 3.2) is extracted: $\sum_{n+1} M_{ext} = \sum_n M_{ext} + M - M_{min}$. The amount of extracted melt is then instantaneously transported upwards and randomly chosen to be deposited as either volcanic or plutonic crust. Volcanic rocks are deposited at the surface while plutonic rocks are deposited at the LAB and where no lithosphere is present, the LAB is equal to the Moho.

The eruption efficiency of volcanic compared to plutonic eruption can be freely varied via the parameter χ_{volc} . Eruption efficiency on present-day Earth is estimated to be around 5 – 20% (Crisp, 1984). However, it is not clear whether this also holds true for Precambrian tectonic settings. In the heat-pipe mode suggested by Moore and Webb (2013), it is assumed to be 100%. We therefore vary χ_{volc} between 0% and 100%.

Another consequence of the implemented melting and crustal growth approach is that the total volume of rock is not conserved. Melt removal will not lead to a decrease in volume of the depleted mantle rock but to an additional increase in volume by the newly formed crust. In the subduction models this discrepancy is addressed by allowing mantle rock to escape through the bottom of the model and forcing inflow of rock and ‘sticky air’ material at the left and right model boundary. In the plume-lid model setup, ‘sticky air’ material is consumed.

2.7 Density changes due to phase transitions and mantle depletion

For the basalts of the upper and lower oceanic crust, a phase transition from basalt to garnet-granulite and then eclogite (Ito and Kennedy, 1971) is taken into account. Eclogitisation of subducted crust is implemented as a linear density increase with pressure and temperature from 0% to 16% in the PT-region between the experimentally determined garnet-in and plagioclase-out phase transitions in basalt (Ito and Kennedy,

1971):

$$P_{Ga-In} = \begin{cases} -9213.25 + T \cdot 15.25, & \text{if } P \geq 3000 \text{ bar} \\ 3000.0, & \text{if } P < 3000 \text{ bar} \end{cases} \quad (2.13a)$$

$$P_{Pl-Out} = \begin{cases} -1560 + 20 \cdot T, & \text{if } P \geq 15000 \text{ bar} \\ 15000.0, & \text{if } P < 15000 \text{ bar} \end{cases} \quad (2.13b)$$

$$\rho_e = \begin{cases} \rho_b, & P \leq P_{Ga-In} \\ \rho_b \cdot \left(1.0 + 0.16 \cdot \frac{P - P_{Ga-In}}{P_{Pl-Out} - P_{Ga-In}} \right), & P_{Ga-In} < P < P_{Pl-Out} \\ \rho_b \cdot 1.16, & P \geq P_{Pl-Out}, \end{cases} \quad (2.14)$$

where P_{Ga-In} (bar) is the temperature dependent basalt to garnet-granulite transition pressure, P_{Pl-Out} (bar) is the temperature dependent garnet-granulite to eclogite transition pressure and ρ_b and ρ_e are the basalt and eclogite densities respectively.

Depending on the accumulated amount of extracted melt $\sum_n M_{ext}$, the density of solid peridotite and the solid fraction of partially molten peridotite is adjusted in the following way:

$$\rho_{s,depleted} = \rho_s \cdot \left(1.0 - 0.04 \cdot \sum_{n=1} M_{ext} \right). \quad (2.15)$$

With increasing amount of extracted melt, the density of the residue is decreasing (Schutt and Lesher, 2006). For mantle peridotite with an accumulated amount of extracted melt $\sum_n M_{ext} > 0.3$, the mantle is assumed to be strongly depleted and will be considered and visualised as lithospheric instead of asthenospheric peridotite. However further depletion is still possible.

2.8 Rheological model

Several different rock types are available in both solid and partially molten state (see Fig. 2.3). To each of these rock types, one of four different visco-plastic flow laws is applied. A wet quartzite flow law (Ranalli, 1995) is applied to sediments and upper crustal material. The lower crust follows a plagioclase An₇₅ flow law and dry or wet mantle follow a respective (i.e. dry or wet) olivine flow law (Ranalli, 1995). See

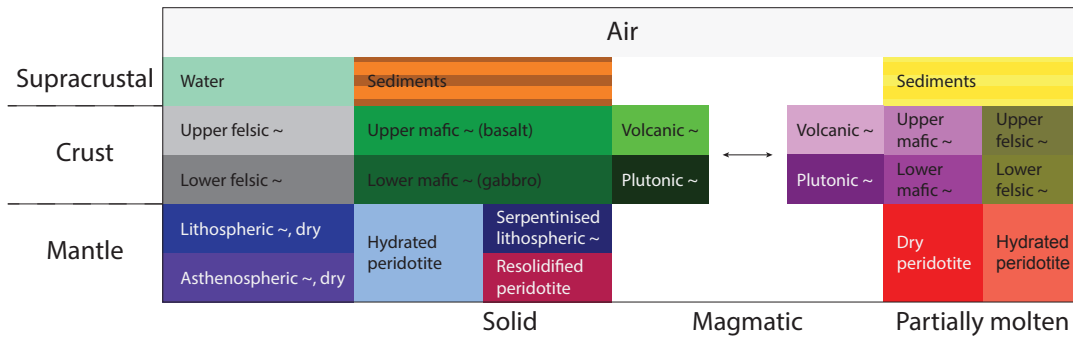


Figure 2.3: All available material types and their colour code in both solid and partially molten state, as will be used throughout this thesis.

Tables 3.1 and 4.1 for a full compilation of material properties.

A visco-plastic rheology is employed, where the relationship between the deviatoric stress σ'_{ij} and strain-rate $\dot{\epsilon}_{ij}$ is described by the visco-plastic constitutive law. For incompressible viscous deformation, this results in the law of viscous friction,

$$\sigma'_{ij} = 2\eta_{eff}\dot{\epsilon}_{ij}, \quad (2.16)$$

where

$$\dot{\epsilon}_{ij} = \frac{1}{2} \left(\frac{\partial v_i}{\partial x_j} + \frac{\partial v_j}{\partial x_i} \right), \quad (2.17)$$

where η_{eff} denotes the effective viscosity which depends on pressure, temperature, composition, strain rate and degree of melting.

For the ductile creep regime, contributions from different flow laws, such as dislocation and diffusion creep, are taken into account using the inverse average ductile viscosity $\eta_{ductile}$,

$$\frac{1}{\eta_{ductile}} = \frac{1}{\eta_{newt}} + \frac{1}{\eta_{powl}}, \quad (2.18)$$

where η_{newt} and η_{powl} are effective viscosities for Newtonian diffusion and power-law

dislocation creep, respectively, calculated as

$$\eta_{newt} = \frac{1}{2} A_D \sigma_{crit}^{1-n} \exp\left(\frac{E_a + PV_a}{RT}\right), \quad (2.19a)$$

$$\eta_{powl} = \frac{1}{2} A_D^{\frac{1}{n}} (\dot{\epsilon}_{II})^{\frac{1-n}{n}} \exp\left(\frac{E_a + PV_a}{nRT}\right), \quad (2.19b)$$

where $\dot{\epsilon}_{II} = \sqrt{1/2 (\epsilon_{ij})^2}$ is the second invariant of the strain rate tensor, E_a, V_a represent activation energy and volume respectively, A_D is an experimentally defined material constant, n is the stress exponent and σ_{crit} is the diffusion-dislocation transition stress (see Tables 3.1 and 4.1).

In high stress regions where $\sigma_{II} > 10^8$ MPa, the Peierls creep mechanism is invoked additionally (Katayama and Karato, 2008),

$$\dot{\epsilon}_{II,Peierls} = A_{Peierls} \sigma_{II}^2 \exp\left\{-\frac{E_a + PV_a}{RT} \left[1 - \left(\frac{\sigma_{II}}{\sigma_{Peierls}}\right)^k\right]^q\right\}, \quad (2.20a)$$

$$\eta_{Peierls} = \frac{\sigma_{II}}{2\dot{\epsilon}_{II,Peierls}}, \quad (2.20b)$$

where $\sigma_{II} = \sqrt{1/2 (\sigma_{ij})^2}$ is the second stress invariant, $A_{Peierls} = 10^{-4.2} \text{ s}^{-1} \text{ MPa}^{-2}$ is a material constant for Peierls creep, $\sigma_{Peierls} = 9.1 \cdot 10^9$ MPa is the dry Peierls stress which defines the maximum strength of the material similar to the yield stress. The two exponents $k = 1.0$ and $q = 2.0$ are influenced by limiting factors of the dislocation motion (Katayama and Karato, 2008).

A brittle Drucker-Prager yield criterion with strain weakening and fracture healing is implemented (following Gerya, 2013, and references therein). For brittle or plastic deformation, a yield stress σ_{yield} is defined which depends on the cohesion C_{eff} , the internal friction coefficient ϕ_{eff} , and the melt-induced weakening factor λ_{melt} (Gerya et al., 2015). The melt-induced weakening factor itself depends on the melt pressure P_{melt} and the total pressure P .

$$\sigma_{yield} = C_{eff} + \phi_{eff} P \lambda_{melt}, \quad (2.21a)$$

$$\lambda_{melt} = 1 - \frac{P_{melt}}{P}, \quad (2.21b)$$

Melt-induced weakening (see Table 4.2) is only applied locally to lithospheric rock markers above areas of melt extraction. For all other rocks, no weakening is assumed ($\lambda_{melt} = 1$).

Internal friction coefficient ϕ_{eff} and cohesion C_{eff} are defined as follows:

$$\phi_{eff} = \begin{cases} \phi_0, & \text{if } \gamma \leq \gamma_0 \\ \phi_0 + (\phi_1 - \phi_0) \frac{\gamma - \gamma_0}{\gamma_1 - \gamma_0}, & \text{if } \gamma_0 < \gamma \leq \gamma_1 \\ \phi_1, & \text{if } \gamma > \gamma_1, \end{cases} \quad (2.22)$$

$$C_{eff} = \begin{cases} C_0, & \text{if } \gamma \leq \gamma_0 \\ C_0 + (C_1 - C_0) \frac{\gamma - \gamma_0}{\gamma_1 - \gamma_0}, & \text{if } \gamma_0 < \gamma \leq \gamma_1 \\ C_1, & \text{if } \gamma > \gamma_1, \end{cases} \quad (2.23)$$

where ϕ_0 and ϕ_1 are the initial and final values for the friction coefficient, C_0 and C_1 are the initial and final values for the cohesion, $\gamma \geq 0$ is the integrated plastic strain and γ_0 and γ_1 are the lower and upper strain limits for fracture related weakening respectively. Values for all different rock types can be found in Table 4.1. The integrated plastic strain γ is calculated in the following way:

$$\gamma = \int \sqrt{\frac{1}{2}(\dot{\epsilon}_{ij(plastic)})^2} dt - \int \dot{\epsilon}_{healing} dt, \quad (2.24)$$

where $\dot{\epsilon}_{ij(plastic)}$ is the plastic strain rate tensor and $\dot{\epsilon}_{healing}$ is the fracture healing rate (see Table 4.2).

An upper viscosity limit $\eta_{plastic}$ of the yielding material can now be calculated by using the second strain rate invariant $\dot{\epsilon}_{II}$:

$$\eta_{plastic} = \frac{\sigma_{yield}}{2\dot{\epsilon}_{II}}, \quad (2.25)$$

Finally the effective viscosity $\eta_{eff}(T, P, c, M)$, depending on temperature, pressure, composition and melt fraction, is the minimum of all viscosity values,

$$\eta_{eff} = \min \{ \eta_{ductile}, \eta_{Peierls}, \eta_{plastic} \}. \quad (2.26)$$

2.9 Abbreviations and units

Table 2.1: Abbreviations and units

Symbol	Meaning
A_D	material constant [$\text{Pa}^{-n}\text{s}^{-1}$]
C_P	isobaric heat capacity [$\text{J}/\text{kg}/\text{K}$]
C_{eff}	effective cohesion [Pa]
c	composition
E_a	activation energy [J/mol]
g	gravitational acceleration [m/s^2]
H_r, H_a, H_s	radiogenic, adiabatic and shear heating [W/m^3]
H_L	latent heating coefficient [J/kg]
k	thermal conductivity [$\text{W}/\text{m}/\text{K}$]
M	volumetric fraction of melting
n	stress exponent
P	dynamic pressure [Pa]
P_{melt}	melt pressure [Pa]
\vec{q}	heat flux
R	gas constant [$\text{J}/\text{K}/\text{mol}$]
T	temperature [K]
V_a	activation volume [$\text{J}/\text{Pa}/\text{mol}$]
v_x, v_y, v_z	components of velocity vector [m/s]
X_{H_2O}	pore water content [wt%]
α	thermal expansion coefficient [K^{-1}]
γ	integrated plastic strain
$\dot{\epsilon}_{ij}$	strain rate tensor [s^{-1}]
$\dot{\epsilon}'_{ij}$	deviatoric strain rate tensor [s^{-1}]
$\dot{\epsilon}_{II}$	second invariant of the deviatoric strain rate tensor [s^{-1}]
$\dot{\epsilon}_{healing}$	fracture healing rate [s^{-1}]
η	viscosity [$\text{Pa} \cdot \text{s}$]
λ_{melt}	melt-induced weakening factor
ρ	material density [kg/m^3]
σ_{ij}	stress tensor [Pa]
σ'_{ij}	deviatoric stress tensor [Pa]
σ_{II}	second invariant of the deviatoric stress tensor [Pa]

ϕ_{eff}	effective dry internal friction coefficient
χ_{volc}	volcanic eruption efficiency

References

- J. P. Burg and T. V. Gerya. The role of viscous heating in Barrovian metamorphism of collisional orogens: thermomechanical models and application to the Lepontine Dome in the Central Alps. *Journal of Metamorphic Geology*, 23(2):75–95, 2005.
- J. A. D. Connolly. Computation of phase equilibria by linear programming: A tool for geodynamic modeling and its application to subduction zone decarbonation. *Earth and Planetary Science Letters*, 236(1–2):524–541, 2005.
- F. Cramer, H. Schmeling, G. J. Golabek, T. Duretz, R. Orendt, S. J. H. Buiter, D. A. May, B. J. P. Kaus, T. V. Gerya, and P. J. Tackley. A comparison of numerical surface topography calculations in geodynamic modelling: an evaluation of the ‘sticky air’ method. *Geophysical Journal International*, 189(1):38–54, 2012.
- J. A. Crisp. Rates of magma emplacement and volcanic output. *Journal of Volcanology and Geothermal Research*, 20(3–4):177–211, 1984.
- R. Fischer and T. Gerya. Early Earth plume tectonics: A high-resolution 3D numerical modelling approach. *Journal of Geodynamics*, in press.
- R. Fischer and T. Gerya. Regimes of subduction and lithospheric dynamics in the Precambrian: 3D thermomechanical modelling. *Gondwana Research*, submitted for publication.
- T. V. Gerya. *Introduction to Numerical Geodynamic Modelling*. Cambridge University Press, 2010.
- T. V. Gerya. Three-dimensional thermomechanical modeling of oceanic spreading initiation and evolution. *Physics of the Earth and Planetary Interiors*, 214:35–52, 2013.
- T. V. Gerya and F. I. Meilick. Geodynamic regimes of subduction under an active margin: effects of rheological weakening by fluids and melts. *Journal of Metamorphic Geology*, 29(1):7–31, 2011.
- T. V. Gerya and D. A. Yuen. Characteristics-based marker-in-cell method with conser-

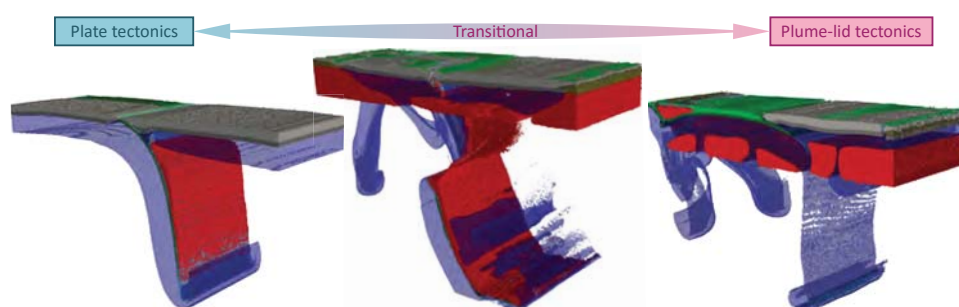
- vative finite-differences schemes for modeling geological flows with strongly variable transport properties. *Physics of the Earth and Planetary Interiors*, 140(4):293–318, 2003.
- T. V. Gerya and D. A. Yuen. Robust characteristics method for modelling multiphase visco-elasto-plastic thermo-mechanical problems. *Physics of the Earth and Planetary Interiors*, 163(1-4):83–105, 2007.
- T. V. Gerya, J. A. D. Connolly, D. A. Yuen, W. Górczyk, and A. M. Capel. Seismic implications of mantle wedge plumes. *Physics of the Earth and Planetary Interiors*, 156(1–2):59–74, 2006.
- T. V. Gerya, R. J. Stern, M. Baes, S. V. Sobolev, and S. A. Whattam. Plate tectonics on the Earth triggered by plume-induced subduction initiation. *Nature*, 527(7577): 221–225, 2015.
- P. Hess. *Origins of Igneous Rocks*. Harvard University Press, 1989.
- K. Ito and G. C. Kennedy. An Experimental Study of the Basalt-Garnet Granulite-Eclogite Transition. In *The Structure and Physical Properties of the Earth’s Crust*, pages 303–314. American Geophysical Union, 1971.
- W. Johannes. The significance of experimental studies for the formation of migmatites. In *Migmatites*, chapter 2, pages 36–85. Springer US, 1985.
- I. Katayama and S.-i. Karato. Low-temperature, high-stress deformation of olivine under water-saturated conditions. *Physics of the Earth and Planetary Interiors*, 168 (3–4):125–133, 2008.
- R. F. Katz, M. Spiegelman, and C. H. Langmuir. A new parameterization of hydrous mantle melting. *Geochemistry Geophysics Geosystems*, 4(9):1073, 2003.
- W. B. Moore and A. A. G. Webb. Heat-pipe Earth. *Nature*, 501(7468):501–505, 2013.
- S. Poli and M. W. Schmidt. Petrology of subducted slabs. *Annual Review of Earth and Planetary Sciences*, 30(1):207–235, 2002.
- G. Ranalli. *Rheology of the Earth*. Springer, 1995.
- M. W. Schmidt and S. Poli. Experimentally based water budgets for dehydrating slabs and consequences for arc magma generation. *Earth and Planetary Science Letters*, 163(1–4):361–379, 1998.

- D. L. Schutt and C. E. Lesher. Effects of melt depletion on the density and seismic velocity of garnet and spinel lherzolite. *Journal of Geophysical Research: Solid Earth*, 111(B5):B05401, 2006.
- E. Sizova, T. Gerya, M. Brown, and L. L. Perchuk. Subduction styles in the Precambrian: Insight from numerical experiments. *Lithos*, 116(3–4):209–229, 2010.
- E. Sizova, T. Gerya, K. Stüwe, and M. Brown. Generation of felsic crust in the Archean: A geodynamic modeling perspective. *Precambrian Research*, 271:198–224, 2015.
- G. Zhu, T. V. Gerya, P. J. Tackley, and E. Kissling. Four-dimensional numerical modeling of crustal growth at active continental margins. *Journal of Geophysical Research: Solid Earth*, 118(9):4682–4698, 2013.

Chapter 3

Regimes of subduction and lithospheric dynamics in the Precambrian: 3D thermomechanical modelling¹

Abstract



Comparing the early Earth to the present day, geological-geochemical evidence points towards higher mantle potential temperature and a different type of tectonics. In order to investigate possible changes in Precambrian tectonic styles, we conduct 3D high-resolution petrological-thermomechanical numerical modelling experiments for oceanic plate subduction under an active continental margin at a wide range of mantle potential temperature T_p ($\Delta T_p = 0 - 250$ K, compared to present-day conditions). At present-day mantle temperatures ($\Delta T_p = 0$ K), results of numerical experiments correspond to modern-style subduction, whereas at higher-temperature conditions, important systematic changes in the styles of both lithospheric deformation and mantle convection occur. For $\Delta T_p = 50 - 100$ K a regime of dripping subduction emerges which is still very similar to present-day subduction but is characterised by frequent dripping from the slab tip and a loss of coherence of the slab, which suggests a close relationship between dripping subduction and episodic subduction. At further increasing $\Delta T_p = 150 - 200$ K, dripping subduction is observed together with unstable dripping lithosphere, which corresponds to a transitional regime. For $\Delta T_p = 250$ K, presumably

¹This material is submitted for publication to Gondwana Research, 2016

equivalent to early Archean, the dominating tectonic style is characterised by small-scale mantle convection, unstable dripping lithosphere, thick basaltic crust and small plates. Even though the initial setup is still defined by present-day subduction, this final regime shows many characteristics of plume-lid tectonics. Transition between the two end-members, plume-lid tectonics and plate tectonics, happens gradually and at intermediate temperatures, elements of both tectonic regimes are present. We conclude, therefore, that probably no abrupt geodynamic regime transition point can be specified in the Earth's history and that its global geodynamic regime gradually evolved over time from plume-lid tectonics into modern-style plate tectonics.

3.1 Introduction

The accretion of Earth from matter previously dispersed in the solar nebula and subsequent impact events, among them the moon-forming event (e.g. Canup, 2004), added a tremendous amount of energy to the early Earth (Jaupart et al., 2007). Other important heat sources were the core-mantle differentiation and a high amount of radiogenic elements such as U, Th and K (Wasserburg et al., 1964). Characteristic mantle temperatures at that time were between 50 – 300 K higher than present-day conditions (Abbott et al., 1994, and references therein).

This led to a period of a fully molten mantle, the magma ocean, which started to crystallise while the Earth was cooling. During this continuous process of cooling, the crust was formed and the mantle solidified and started to convect by solid state creep. At some point during further cooling, subduction processes and global plate tectonics must have initiated. However, this early subduction probably looked very different to what is called subduction today, mainly due to the high mantle temperature (e.g. van Hunen and van den Berg, 2008; Sizova et al., 2010, and references therein). With the continued cooling of the Earth's mantle, also amplified by the onset of plate tectonics, the style of subduction changed throughout the Precambrian and until the present day to the modern style of subduction which is the most well-known and commonly referred to as subduction.

Present-day Earth allows us to not only study directly accessible data at its surface by various means but also to sample geophysical data in its interior. This gives us a good understanding of the modern-day geodynamic processes. However, in the study of

Precambrian geodynamics, natural data are much more restricted since no geophysical information for the deep Earth's interior at that time is available (Gerya, 2014). The only accessible data is the geological, geochemical, petrological and geochronological data of Precambrian rocks from the Earth's surface. But the Precambrian rock record is relatively scarce and becomes more restricted with increasing rock age (Fig. 1.4).

Major outcrops of Precambrian rocks are mainly found in cratons and continental shields. Examples of Archean outcrops are the Slave province in Canada (Bleeker et al., 1999), the Pilbara craton in Australia (Collins et al., 1998; Hickman, 2004; Van Kranendonk et al., 2004) or the Kaapvaal craton in South Africa.

Granite-greenstone terrains (GGT) are a general structural element in cratons. Greenstones form circular networks (Van Kranendonk et al., 2004) or winding belts of tholeiitic basalts and komatiites often accompanied by metasediments and banded iron formations (Bleeker et al., 1999).

For most cratons, a felsic basement comprised of TTG has been shown (e.g. Slave province: Bleeker et al. (1999), Pilbara craton: Van Kranendonk et al. (2004), Kaapvaal craton: Kisters and Anhaeusser (1995); Van Kranendonk (2011)). This basement usually shows a characteristic dome-and-keel structure with large TTG domes intruding into the overlying greenstone cover (Hamilton, 1998; Van Kranendonk et al., 2004; François et al., 2014). Often several generations of granitoid intrusion can be found, sometimes within one dome with the oldest suit on the outside (Van Kranendonk et al., 2004). Several different mechanism have been proposed to generated these patterns. Many authors discuss the similarities of greenstone belts to modern ophiolite zones both structurally (de Wit, 1998) and chemically (Furnes et al., 2014). This leads to the conclusion that plate tectonics and with it, subduction might have been already operable in the Eoarchean or even Hadean (Furnes et al., 2014). Another possibility is the formation of the TTG domes by diapirism or sagduction (e.g. Hill et al., 1991; Vlaar et al., 1994; François et al., 2014). The layering of mafic greenstones on top of felsic TTGs creates a density instability which results in partial convective overturn (Collins et al., 1998; Van Kranendonk, 2011). The typical pattern of TTG domes with greenstone belts in-between emerges; this is best conserved in the East Pilbara (François et al., 2014). The process of sagduction does not necessarily require active plate tectonics and can therefore be seen as an alternative to an early onset of the subduction process (Hamilton, 1998).

In this context, the two questions which are most strongly debated are (1) the timing and mechanism of onset of subduction and (2) the change of style in subduction throughout the Earth history. To answer these important questions, numerical geodynamic models should be used in addition to restricted natural data (e.g. Vlaar et al., 1994; van Hunen and van den Berg, 2008; Sizova et al., 2010; Gerya, 2014; Gerya et al., 2015, and references therein).

Previous studies focused on 2D numerical models of Precambrian subduction. Van Hunen and van den Berg (2008) found in particular that an increase of 200–300 K in the mantle potential temperature T_p leads to episodic subduction interrupted by frequent slab break-off. Sizova et al. (2010) were able to identify several geodynamic regimes mainly depending on mantle potential temperature. They found a transition from ‘no-subduction’ to ‘pre-subduction’ for a mantle 200–250 K hotter, where ‘pre-subduction’ is characterised by shallow underthrusting and two-sided lithospheric downwellings. A second transition from ‘pre-subduction’ to present-day subduction was found at 160 – 175 K increased mantle potential temperature.

Despite the fact that Precambrian crustal deformation processes are typically characterised by three-dimensional mass redistribution (Chardon et al., 2009; Perchuk and Gerya, 2011; François et al., 2014), no 3D numerical modelling studies of Precambrian tectonics have been carried out so far. This study will therefore be the first to present 3D numerical modelling results. In the following, mantle temperature is identified as the dominant parameter (among others van Hunen and van den Berg, 2008; Sizova et al., 2010, 2014) which influences the subduction style. Subduction stability is then analysed back in geological time by means of exploring higher mantle potential temperature (van Hunen and van den Berg, 2008; Sizova et al., 2010, 2014), although no direct time-temperature correlation is explored in our study.

3.2 Methods

3.2.1 Model design

To simulate the process of subduction of an oceanic plate beneath an overriding continent, a model setup (see Fig. 3.2a) with a size of $1000 \times 328 \times 680$ km has been chosen. The model resolution is $2 \times 2 \times 2$ km per cell with a subgrid resolution of 1 km for the

material properties defined on Lagrangian markers. The model setup follows closely the 2D models described by Sizova et al. (2010) as well as 3D laterally variable modern subduction/collision models explored by Duretz et al. (2014) for comparison with previous results. The continental crust of the overriding plate at the left model boundary has a length of 400 km while the oceanic crust of the subducting plate has a length of 600 km on one half of the model domain and a length of 500 km on the other half to allow space for a continental corner of 100 km by 500 km at the right model boundary (Fig. 3.2a).

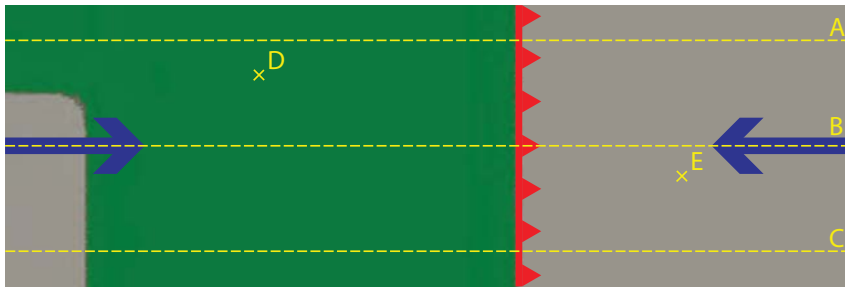


Figure 3.1: Top view of the model setup used. Blue arrows indicate the direction of compression, while the red line indicates the position of the prescribed weak zone. Letters denote positions of different 2D (A)-(C) and 1D (D),(E) profiles.

The models have been carried out with the 3D numerical I3ELVIS code (Gerya and Yuen, 2007) which is based on a conservative finite difference method with a multigrid solver and a non-diffusive marker-in-cell technique to simulate multiphase flow (Gerya and Yuen, 2003, 2007). Additionally, the 3D code also features melting of crustal and mantle rocks and volcanic addition of primordial crust from silicate melt, eclogitic phase changes as well as hydration and dehydration (Zhu et al., 2013).

The oceanic crust is modelled by a 3 km thick layer of basalt above a 5 km thick layer of gabbro. The continental crust consists of felsic rock of 35 km thickness in total while the upper continental crust is 12 km thick and the lower continental crust is 23 km thick. A lithospheric mantle of dry peridotite extends down to a depth of 90 km.

An inclined weak fracture zone of wet olivine rheology (Ranalli, 1995) is introduced which will allow focused subduction initiation at a prescribed narrow zone along the continental margin. The weak zone extends to the bottom of the lithosphere, forming a straight line between continental and oceanic plate continuing through the entire model domain (Duretz et al., 2014).

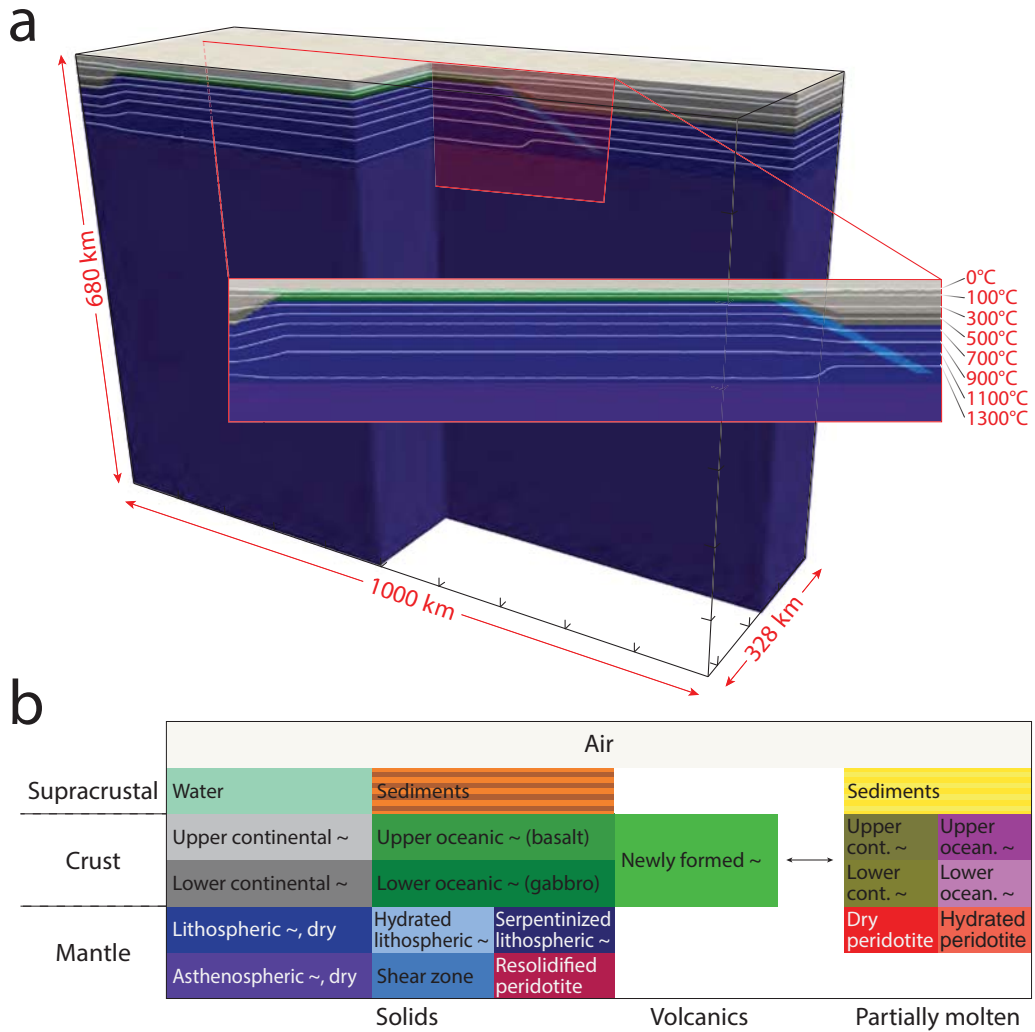


Figure 3.2: (a) Initial model setup. An enlarged view of the future subduction area is shown in the inset. (b) All available material types and their colour code in both solid and partially molten state, as will be used throughout this paper.

All mechanical boundary conditions are free slip except for the bottom boundary which is open. The uppermost 12 – 15 km of the model domain are filled with ‘sticky air’ which acts as an internal free surface boundary condition (Cramer et al., 2012). In the uppermost 130 km, constant convergence velocity conditions are applied at the left and right model boundary (except for model $A0$, where velocity boundary conditions are applied over the entire left and right model boundaries, see Fig. 3.3a) giving an overall convergence rate of 3.0 cm/yr partitioned as 1.0 cm/yr and 2.0 cm/yr between the left and right plate, respectively (Figs. 3.1 and 3.3b). This forced convergence rate

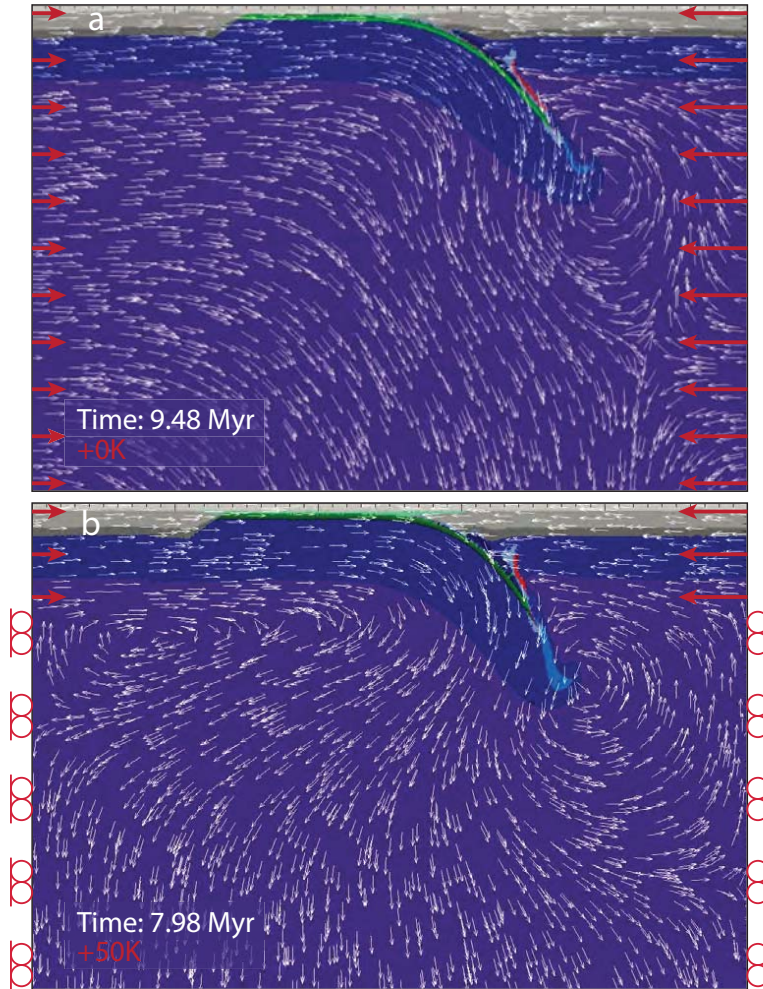


Figure 3.3: Imposed side boundary conditions for models (a) *A0* and (b) *A1* to *A6*, where arrows indicate compression and wheels indicate free slip conditions. Position of the slice corresponds to profile B in Fig. 3.1, scales are given in Fig. 3.2a.

decreases linearly to zero between 20 and 25 Myr and is set to zero after 25 Myr. These boundary conditions allow the development of a self-consistent subduction zone which will go into a retreating mode after the forced convergence is stopped and leads to extension of the overriding plate.

The temperature structure of the oceanic plate is given by the oceanic geotherm which is calculated for a given cooling age and mantle potential temperature (Turcotte and Schubert, 2002). The temperature structure in the continental plate is given by a linear geotherm. The surface temperature is fixed at 273 K whereas the temperature at the lithosphere-asthenosphere boundary (LAB) is given by the adopted asthenospheric

geotherm. The thickness of the lithosphere and the depth of the LAB is defined thermally by the change in slope of the temperature profile. The asthenosphere has a fixed linear adiabatic temperature gradient of 0.5 K/km . However the mantle potential temperature T_p is varied in different experiments to simulate early-Earth-like conditions ($\Delta T_p = 0 - 250 \text{ K}$ compared to present-day reference mantle potential temperature $T_p = T_{initial} = 1556 \text{ K}$ (Herzberg et al., 2007)).

The eruption efficiency in these models is chosen $\chi_{volc} = 100\%$. This is a model simplification because eruption efficiency on Earth is estimated to be around $5 - 20\%$ and thus most magmatic rocks are added to the crust as intrusions (plutons) rather than volcanic sequences (Crisp, 1984). The amount of volcanic rocks in our models will therefore be overestimated while melt emplacement into the crust in the form of intrusions will be neglected. The consequences are higher surface heat flux and larger heat loss to the atmosphere (Keller and Tackley, 2009). Thresholds for melt extraction are set to $M_{min} = 2 \text{ wt\%}$ while M_{max} can vary depending on the model setup (see Table 3.2). For brittle or plastic deformation, a yield stress σ_{yield} is defined which depends on the cohesion $C_{eff} = C_0$, the effective internal friction angle $\phi_{eff} = \phi_0$ and the pressure. An upper viscosity limit $\eta_{plastic}$ of the yielding material can be calculated. See Chapter 2 for details. No melt-induced weakening and fracture healing is incorporated in these models. This means $\lambda_{melt} = 1$ because $P_{melt} = 0$ and $\varepsilon_{healing} = 0$. Erosion and sedimentation level are set to $y_{eroslev} = 8 \text{ km}$ respectively $y_{sedilev} = 20 \text{ km}$, while the sea level is fixed at $y_{waterlev} = 12 \text{ km}$. 10^{19} Pa s and 10^{24} Pa s are used as respectively lower and upper cut-off viscosity limits for all types of materials.

16 different rock types (not including ‘sticky air’ and ‘sticky water’) are available in both solid and partially molten state (see Fig. 3.2b). To each of these rock types one of four different visco-plastic flow laws is applied. A wet quartzite flow (Ranalli, 1995) law is applied to sediments and upper crustal material. The lower crust follows a plagioclase An_{75} flow law and dry or wet mantle follow a respective (i.e. dry or wet) olivine flow law (Ranalli, 1995) (see Table 3.1 for a full compilation of material properties).

For a more detailed discussion of the applied methods, see Chapter 2 and Fischer and Gerya (submitted for publication).

Table 3.1: Material properties ^a as well as applied rheology and melting model are listed for each of the used lithologies as given in Fig. 3.2b.

Material	Rheology [MPa ⁻ⁿ s ⁻¹], [-], [kJ], [J/bar]	ρ_0 [kg/m ³]	k [K]	Melting [$\frac{W}{m \cdot K}$]	H_r^b [$\frac{\mu W}{m^3}$]	H_L [$\frac{kJ}{kg}$]	ϕ_{eff} [-]	σ_{crit} [MPa]	C_p [kJ/kg]
Sediments,	solid	2600	$0.64 + \frac{807}{T+77}$	Eq. (2.7)	2.0	300	0.0	0.03	1.0
	molten	2400						0.0	1.5
Dry felsic crust,	solid	2750			1.0		0.15	0.03	1.0
	molten	2400			2.0		0.0	0.0	1.5
Hydrated felsic crust,	solid	2700			1.0		0.03	0.03	1.0
	molten	2400					0.0	0.0	1.5
Basalt,	solid	3000	$1.18 + \frac{474}{T+77}$	Eq. (2.8)	0.25	380		0.03	1.0
	molten	2900						0.0	1.5
Lower continental crust, Gabbro,	solid	2950	$1.18 + \frac{474}{T+77}$	Eq. (2.9)	0.5	380	0.15	0.03	1.0
	molten	2400	$0.64 + \frac{807}{T+77}$		2.0		0.0	0.0	1.5
	solid	3000	$1.18 + \frac{474}{T+77}$		0.25		0.6	0.03	1.0
Hydrated basalt,	molten	2900					0.0	0.0	1.5
	solid	2900		Eq. (2.8)	0.5			30	1.0
Dry mantle peridotite,	molten	2400	$0.64 + \frac{807}{T+77}$		1.0			0.0	1.5
	solid	3300	$0.73 + \frac{1293}{T+77}$	Eq. (2.10)	0.022	400	0.6	0.03	1.0
Hydrated mantle peridotite,	molten	2900					0.0	0.0	1.5
	solid	3300	$0.73 + \frac{1293}{T+77}$	Eq. (2.10)	0.022	400	0.0	30	1.0
	molten	2900			0.05			30	1.0
Weak zone,	solid	3300			0.022			0.0	1.5
	molten	2900						30	1.0
Serpentinite,	solid	3300		-		-		30	1.0
References ^c	4,1	1,2	3		1	1,2			

^a for all rock types: Cohesion $C_0 = 1$ MPa, thermal expansion coefficient $\alpha = 3.0 \cdot 10^{-5} K^{-1}$ and compressibility $\beta = 1.0 \cdot 10^{-5} GPa^{-1}$.

^b fixed at present-day values as the influence of radiogenic heating is negligible compared to increased mantle temperature (Sizova et al., 2010)

^c (1) Turcotte and Schubert (2002), (2) Bittner and Schmeling (1995), (3) Clauser and Huenges (1995), (4) Ranalli (1995), (5) Schmidt and Poli (1998)

3.2.2 Variations in the mantle temperature

3.2.2.1 Development of the mantle geotherm during Earth history

The important difference between the Precambrian and the Phanerozoic is the increased upper mantle and crustal temperature in earlier Earth history due to higher radiogenic and primordial heating rates. Reconstructions of the varying mantle potential temperature during Earth history have already been undertaken by several authors. Geochemical studies show an increase of mantle potential temperature $\Delta T_p = 200 - 300$ K at 3 Ga (Abbott et al., 1994; Herzberg et al., 2007, 2010, and references therein) with a spread in T_p between up- and downwelling regions of up to 200 K (McKenzie and Bickle, 1988; Abbott et al., 1994; Herzberg et al., 2007, 2010). However, no evidence is found for a sudden change in global ambient mantle potential temperature (Abbott et al., 1994; Herzberg et al., 2007, 2010, and references therein). Similar results are obtained by Labrosse and Jaupart (2007) under the assumption of a plate tectonics regime: Their 1D numerical models also show a maximum at 3 Ga but a smaller ΔT_p of 150 K.

3.2.2.2 Reference model series

Table 3.2: List of all reference models (see Section 2.3 for a full description). t_{max} is the maximum model time reached from the beginning of the experiment and BC are the implemented boundary conditions shown in Fig. 3.3.

Model	ΔT_p	M_{min}, M_{max} [wt%]	t_{max} [Myr]	Comment Regime/Fig.	BC
A0	0	2, 4	54.17	I, Fig. 3.5	Fig. 3.3a
A1	50	2, 2	34.66	II	Fig. 3.3b
A2	100	2, 2	26.03	II, Fig. 3.6	Fig. 3.3b
A3	150	2, 2	22.65	II	Fig. 3.3b
A5	175	2, 2	23.36	III, Fig. 3.7	Fig. 3.3b
A4	200	2, 2	9.17	IV	Fig. 3.3b
A6	250	2, 2	6.47	IV, Fig. 3.8	Fig. 3.3b

Due to the demanding computational requirements for high-resolution 3D modelling, this study will focus on the variation of mantle potential temperature ΔT_p which, according to Sizova et al. (2010), is the major reason for observed changes in geodynamic regimes throughout Earth history. Mantle potential temperature is roughly

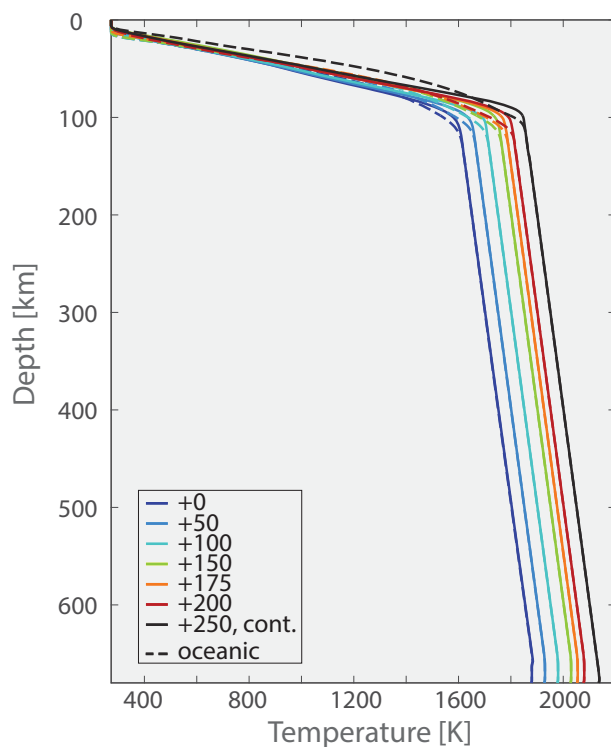


Figure 3.4: Temperature profiles for the reference models (see Table 3.2). Solid lines indicate profiles in continental crust (Fig. 3.1, position E) while dashed lines indicate profiles in the oceanic crust (Fig. 3.1, position D).

correlated with time and influences other important parameters such as the viscosity profile. To model subduction at different stages of Earth history, the reference mantle potential temperature $T_{initial} = 1556$ K (Herzberg et al., 2007) in the initial models is increased by some constant value $\Delta T_p = T(t) - T_{initial}$ (0–250 K) (Fig. 3.4). This way the asthenospheric adiabatic thermal gradient (0.5 K/km) is kept constant, while the lithospheric geotherm flattens and leads to a weakening of the crust and the subcrustal lithospheric mantle (Fig. 3.4).

The reference model A0 corresponds to a typical present-day subduction setup (after Duret et al., 2014) and has a mantle potential temperature of $T_{initial} = 1556$ K. The Precambrian models A1 to A6 differ from the initial model in temperature $\Delta T_p = [50, 100, 150, 175, 200, 250]$ K.

3.2.3 Numerical constraints and setup dependencies

This model setup is constructed to satisfy present-day subduction conditions. For example, the radiogenic heating is not varied between models because the previous work of Sizova et al. (2010) demonstrated its rather minor influence for relatively short timescales (few Myr to few tens Myr) investigated by our numerical modelling study. To account for increased radiogenic and primordial heating in the Precambrian mantle, the mantle potential temperature T_p is increased, which also results in hotter oceanic and continental lithospheric geotherms. The model setup will therefore become less accurate with increasing ΔT_p roughly corresponding to earlier times in Earth history.

Due to the chosen type of model setup, the models will go into a retreating mode of subduction in the oceanic domain (Duretz et al., 2014). After collision and further retreating the model is stopped when the trench reaches the model boundary. Models at higher ΔT_p are more challenging insofar as more melt is produced as well as higher velocities and sharper viscosity contrast are observed. A relatively large minimum viscosity of 10^{19} Pa.s and very short timesteps (< 100 yr) are necessary to stabilise these models. For the present-day model *A0* 50 Myr of model development takes ~ 3 months of compute time which increases to ~ 6 months compute time for only 6.5 Myr of model development for model *A6* at the highest mantle temperature $\Delta T_p = 250$ K.

3.3 Results

In the following, a systematic numerical investigation of the subduction process is undertaken and its spatial and temporal variations in crustal growth, arc formation, plate thickness and dynamic regime are discussed in relation to imposed mantle potential temperature changes. An overview of the discussed models is given in Table 3.2 and Figs. 3.5 to 3.8 as well as Figs. 3.S1 to 3.S4 for melt composition.

3.3.1 Reference model for present-day subduction ($\Delta T_p = 0$ K)

Starting from the setup as shown in Fig. 3.1, the model is compressed with a total convergence speed of 3 cm/yr. Subduction initiates at the prescribed weak zone and

a 6 – 8 km deep trench forms (Fig. 3.9) which starts to fill with sediments. The subducting oceanic plate is driven below the overriding continental plate and bends downward (Fig. 3.5a). The overriding plate is compressed and thickened and forms a mountain range with an elevation of approximately 3 – 4 km (see Fig. 3.S7 for the topographic evolution, where Figs. 3.S7d and 3.S7e correlate with the collisional stage). Scraping of the subducting upper crust (sediments and basalts) forms an accretionary wedge between the two plates (Fig. 3.12a). Water is transported down together with the subducting hydrated oceanic crust and hydrates both the overriding plate and the asthenospheric mantle wedge above the slab. Due to porous water release from the oceanic crust, felsic continental crust of the overriding plate becomes hydrated which leads to a drop in viscosity, and triggers formation of a subduction channel (Fig. 3.12b). Bound water, which is dragged down and released at greater depths, allows hydration of mantle peridotite on top of the slab. In the first 10 Myr the slab subducts at a shallow angle (Fig. 3.5a). From 8 Myr onwards, the hydrated peridotite starts to partially melt and the relatively warm, advancing slab tip is slightly deflected upwards by asthenospheric flow around the subducting and steepening slab within the next 9 Myr. After ~ 17 Myr the slab subducts into the mantle at a steep angle of almost 90° . The whole upper surface of the slab is covered by a continuous layer of hydrated peridotite, which becomes partially molten at higher temperature conditions. Hydrated peridotite is positively buoyant compared to the ambient dry mantle and starts to rise back up along the subduction channel and penetrates the lithosphere and crust of the overriding continent after ~ 18 Myr further hydrating lower continental crust in proximity of the slab by dehydration-released fluids (Figs. 3.5b and 3.12b).

At the same time the incoming continent, which is carried by the subducting plate, collides with the overriding plate and the initial oceanic basin becomes closed. Within this transitional stage (20 – 25 Myr), compression boundary conditions are gradually deactivated. The incoming continent is subducted to a great depth of over 100 km before the slab breaks off under the continent-continent collision zone, opening a window in the subducting plate. A Subduction-Transform Edge Propagator (STEP) (Govers and Wortel, 2005) associated with plate tear forms along the boundary between continental and oceanic domains of the subducting plate (Fig. 3.5c). Subduction in the oceanic domain continues in a retreating manner after the window opening, driven solely by the slab-pull, and the retreating trench forces the overriding plate to extend (Duretz et al., 2014).

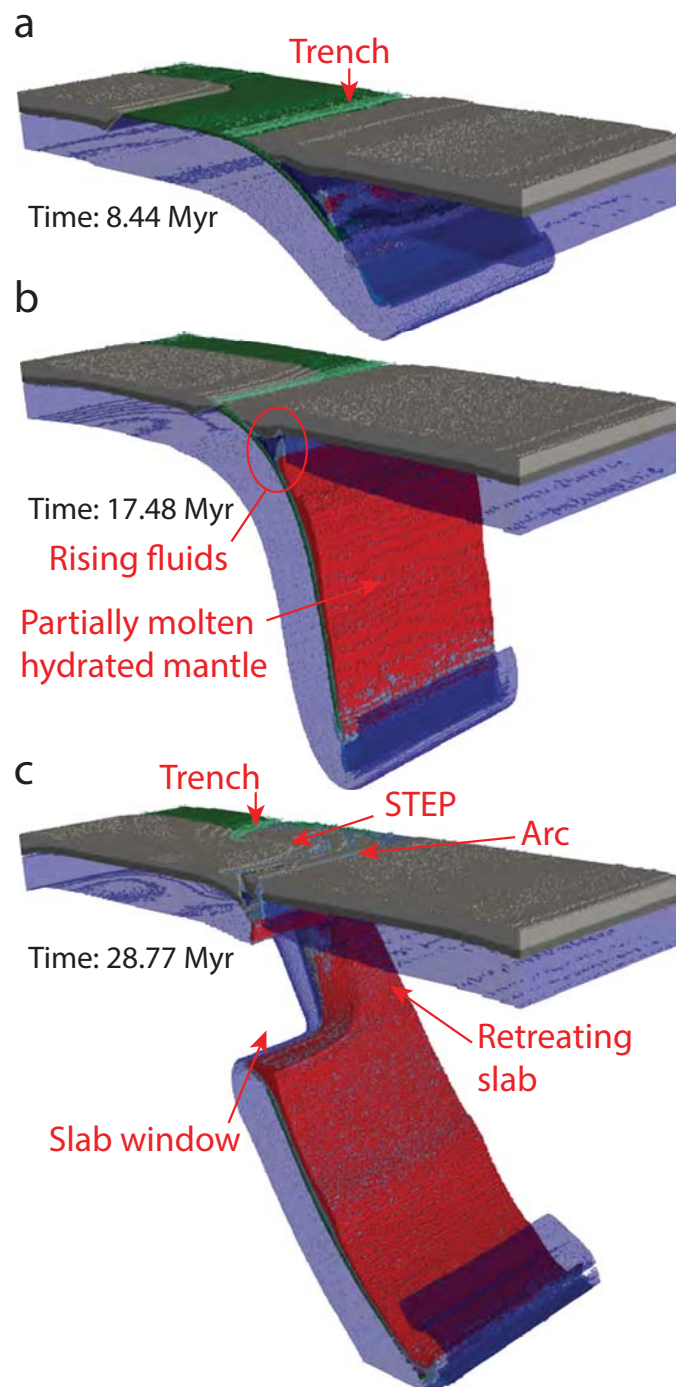


Figure 3.5: Evolution of the present-day reference model $A0$ at $\Delta T_p = 0$ K. The model shows an oceanic-continental subduction with the formation of (a) a trench, (b) a magmatic arc and then continent-continent collision and (c) the opening of a slab window and the formation of a STEP boundary (see text for details and Fig. 3.S1 for detailed melt distribution). Scales are given in Fig. 3.2a.

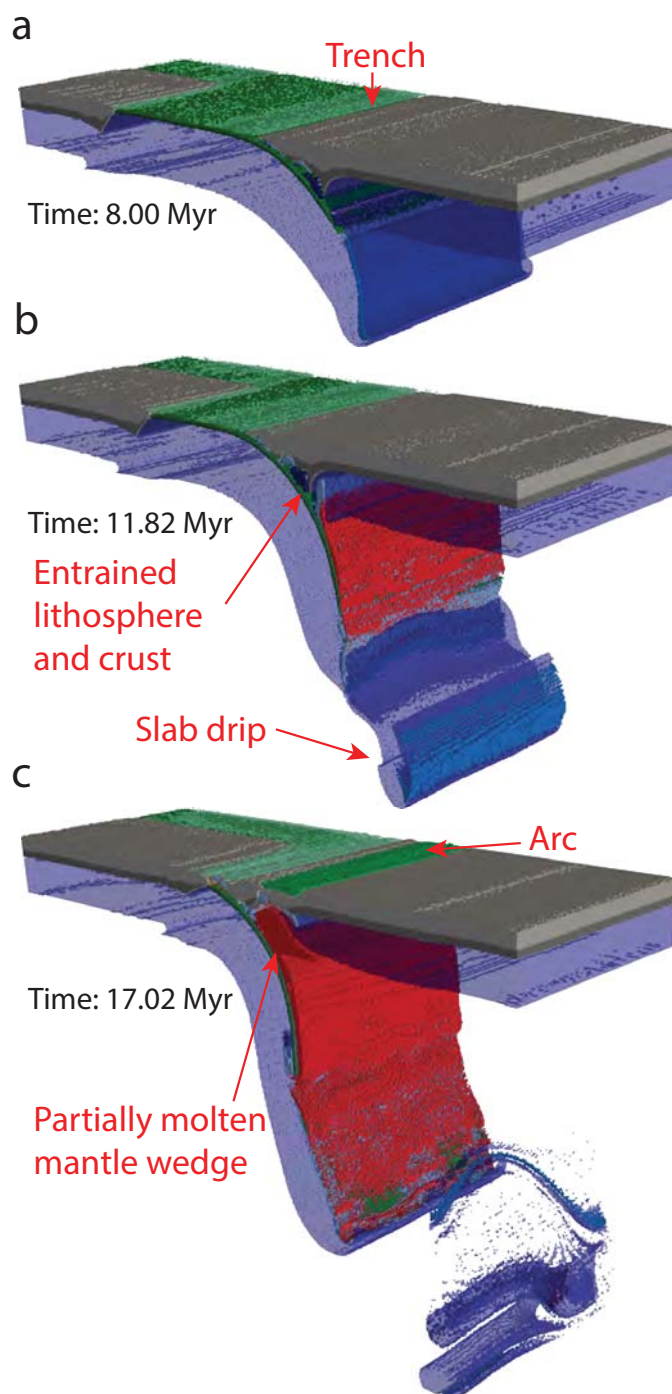


Figure 3.6: Evolution of the model *A2* at $\Delta T_p = 100$ K. The model shows (a) an irregular LAB, (b) ablative subduction and necking of the slab, (c) partial melting of the mantle wedge and a widening of the magmatic arc (see text for details and Fig. 3.S2 for detailed melt distribution). Scales are given in Fig. 3.2a.

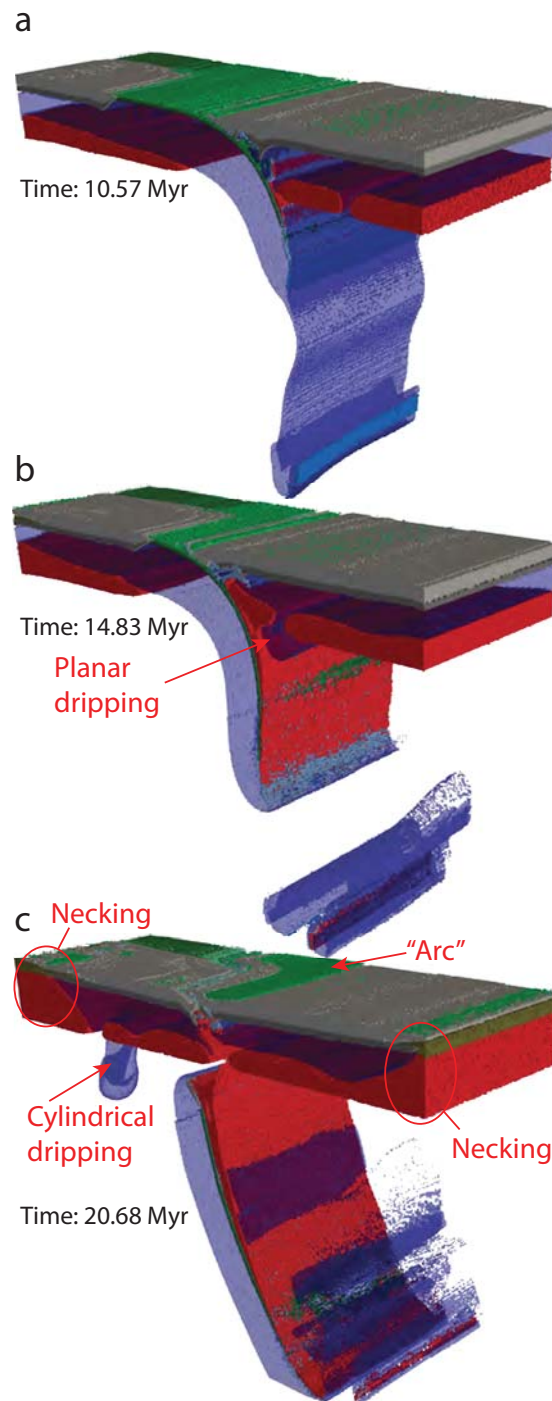


Figure 3.7: Evolution of the model *A5* at $\Delta T_p = 175$ K. The model shows (a) early slab necking, (b)-(c) both planar and cylindrical off-slab lithospheric dripping (see text for details and Fig. 3.S3 for detailed melt distribution). Scales are given in Fig. 3.2a.

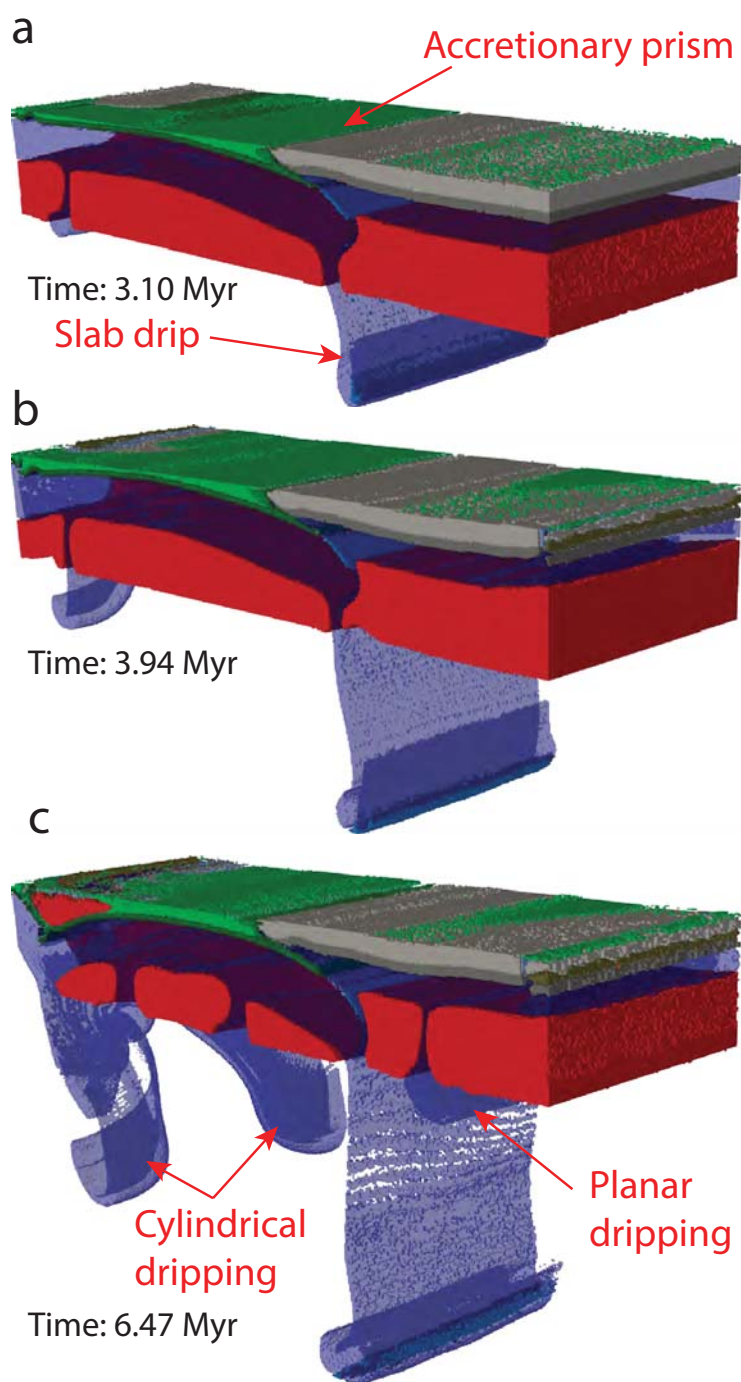


Figure 3.8: Evolution of the model *A6* at $\Delta T_p = 250$ K. The model shows intense non-arc-related basaltic volcanism (light green), (a) rapid necking of the slab tip, (b)-(c) formation of very large accretionary prism (see text for details and Fig. 3.S4 for detailed melt distribution). Scales are given in Fig. 3.2a.

3.3.2 Influence of mantle potential temperature increase ΔT_p

3.3.2.1 Variations in the retreating speed of the subducting slab and trench

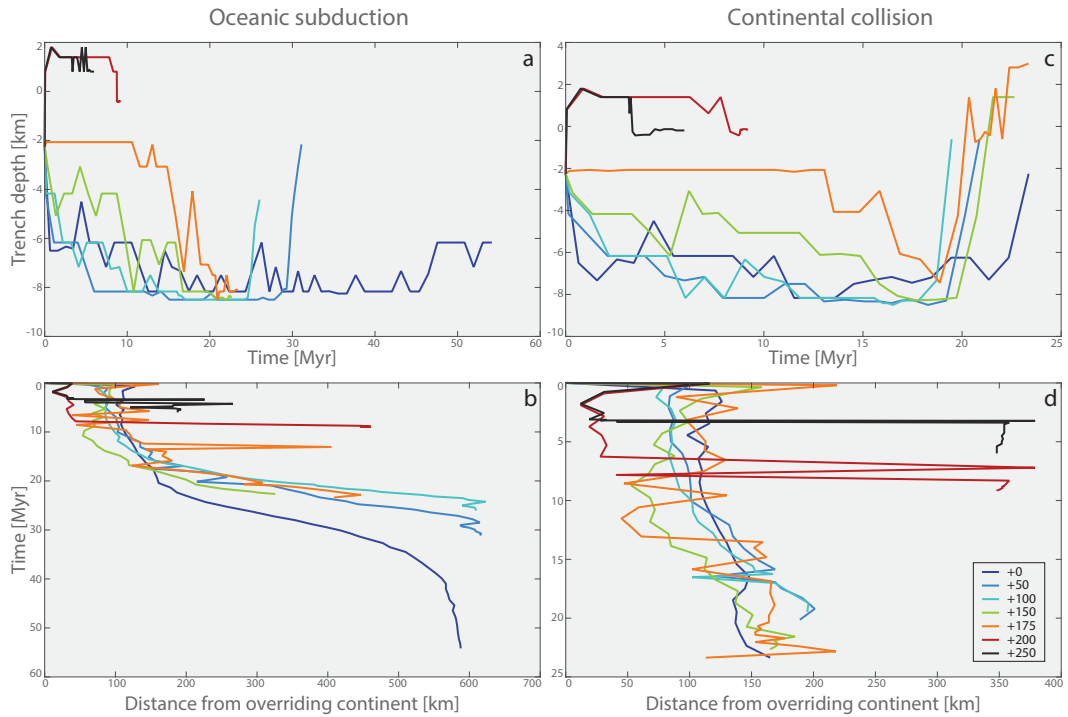


Figure 3.9: Observations of trench retreat at different ΔT_p . The subduction trench is defined as the minimum of the surface profile, where oceanic subduction profiles are taken along profile A (Fig. 3.1) for (a) and (b) and along profile C (Fig. 3.1) for (c) and (d). (a) and (c) show evolution of the trench depth with time in the oceanic and continental domain respectively. (b) and (d) show the distance of retreat from the original trench position (given by the red line in Fig. 3.1) in the oceanic and continental domain respectively. See text for details about oscillatory behaviour.

In the presented models, the applied setup and boundary conditions (see Sections 2.3 and 3.2.3) lead to the formation of a self-consistent subduction with its major driving forces being compression and slab-pull. After the collision event in the continental domain (and the subsequent shut-off of the velocity boundary conditions at 20 – 25 Myr), the only remaining driving force is slab-pull which leads to a retreat of the subducting slab and trench and to an extension of the overriding plate (Fig. 3.9 and Duretz et al. (2014)).

Figure 3.9 shows the minimum elevation automatically picked along a surface profile

in either the oceanic or continental domain of the model. In the present-day model ($\Delta T_p = 0$ K, see also Fig. 3.S7), a 6 – 8 km deep trench is formed within < 5 Myr (Figs. 3.9a and 3.9b). In the continental domain this trench is closed again during the collisional stage (Figs. 3.5c and 3.9c). Looking at the lateral evolution, the trench only migrates by a short distance of 50 km before the collisional stage is reached (Fig. 3.9d). In the oceanic domain, the distance of retreat matches the one found in the continental domain up to the collisional stage. After collision the velocity of retreat is increasing and it slows down again close to the model boundary at a distance of 600 km from the original trench position (Fig. 3.9b).

Models for $\Delta T_p = 50 - 100$ K follow the same pattern (Figs. 3.S8 and 3.9) and the collisional stage looks very similar. However the trench in the continental domain tends to close earlier with increasing ΔT_p (Fig. 3.9c). The same observation can be made for the oceanic domain, where the trench retreats faster for higher ΔT_p (Fig. 3.9b).

Models at $\Delta T_p = 150 - 175$ K (Fig. 3.S9) have a delayed formation of the trench in addition to the earlier closing (Figs. 3.9a and 3.9c). Model *A5* at $\Delta T_p = 175$ K cannot, therefore, reach a maximum trench depth of 8 km in the continental domain (Fig. 3.9c). The profiles also become increasingly more erratic, which signifies that it gets increasingly more complicated to pick a definite trench.

For $\Delta T_p = 200 - 250$ K the ‘trench’ is above sea level for the most time (Figs. 3.9a and 3.9c and topographic figures in Fig. 3.S10). The strongly erratic jumps between 0 – 50 km and 350 – 400 km, mainly visible in the continental domain of the model (Fig. 3.9d), hint at the formation of two ‘proto’-trenches at both sides of the oceanic plate, the active and the passive margin. Similar observations are made in the alternative model *B4h* (see Table 3.S1 and Figs. 3.S5 and 3.S6).

Higher ΔT_p leads to a faster retreat of the trench. The faster retreat is assisted by both a weaker mantle which allows faster slab retreat and a weaker continental crust which allows faster extension of the overriding plate. However there is also a counteracting trend with increasing ΔT_p of decreasing trench depth, caused by stronger volcanic activity.

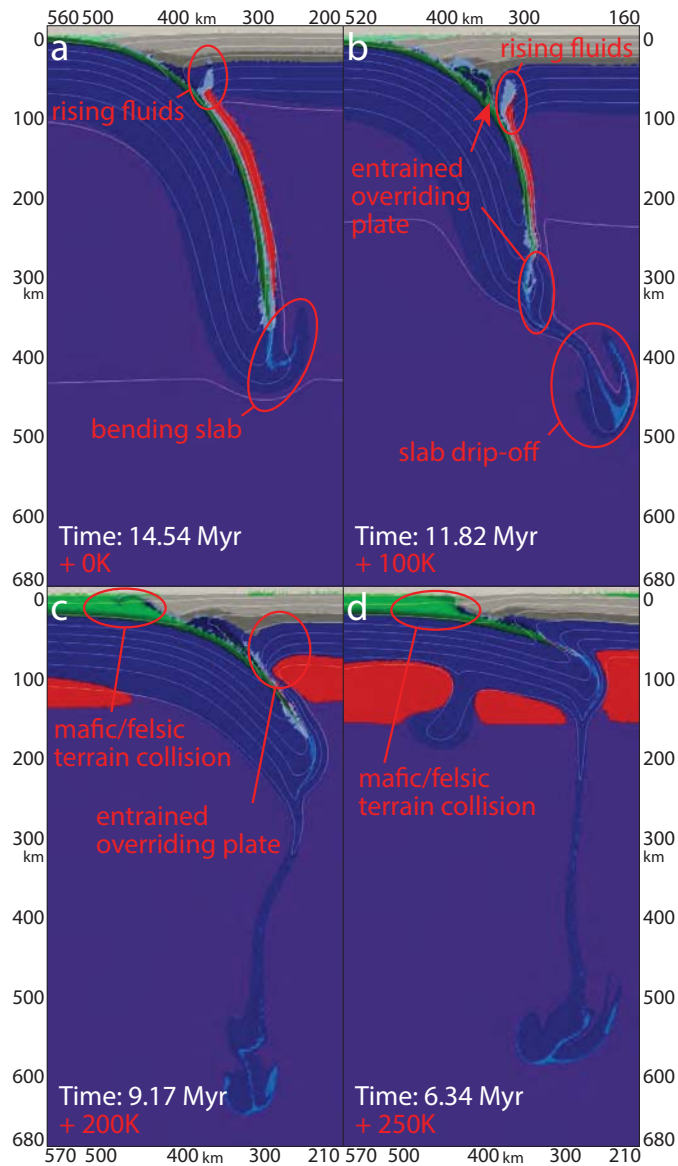


Figure 3.10: Variation of the slab geometry with increasing ΔT_p shown in 2D slices of the reference models. Position of the slice corresponds to profile B in Fig. 3.1.

3.3.2.2 Variations in slab geometry and behaviour

In the Phanerozoic model *A0* it takes 17 Myr of subduction to reach the collisional stage (Figs. 3.5b and 3.5c). The slab penetrates the mantle at a steep angle of $60^\circ - 70^\circ$. The slab tip bends slightly upward however the slab stays coherent during the entire subduction process (Figs. 3.5b and 3.10a).

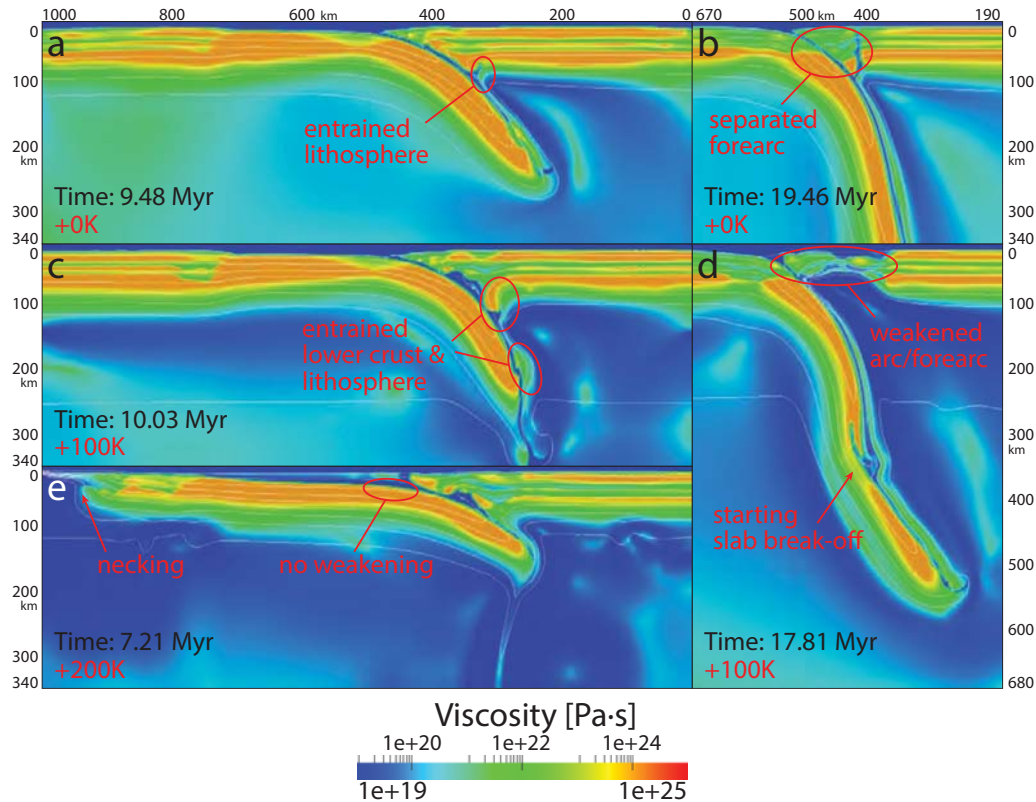


Figure 3.11: Variation of the viscosity with increasing ΔT_p shown in 2D slices of the reference models at an earlier ((a),(c),(e)) and later ((b),(d)) stage. Position of the slice corresponds to profile B in Fig. 3.1.

At a moderate increase in mantle temperature of $\Delta T_p = 100$ K, no large-scale differences are observed in the subduction process (Fig. 3.6). There are some minor changes however. During subduction initiation and in the early stages of subduction, parts of the overriding lithosphere are entrained and subducted as well (see Figs. 3.10b, 3.11c and 3.12c). The subducting plate steepens to its final near-vertical angle of $80^\circ - 90^\circ$ of descent within a shorter timescale of ~ 11 Myr (Fig. 3.10b). After 11 and 13 Myr sheet-like drips develop from the relatively warm advancing slab tip (Figs. 3.6b and 3.6c) and after 20 Myr necking of the slab can be observed at 400 km depth (Fig. 3.11d).

For high upper mantle temperature $\Delta T_p = 200$ K, the slab tip drips off almost immediately after subduction initiation at 2 Myr (Fig. 3.12e). In the model *A4* however, the slab only reaches a depth of 300 km after 9 Myr (Fig. 3.10c) and no weakening due to slab bending can be observed (Fig. 3.11e). The subduction process remains unfinished

and the collisional stage is never reached. In the alternative model *B4h* (see Table 3.S1 and Figs. 3.S5 and 3.S6), the slab reaches the bottom of the model domain. Shortly after subduction initiation, however, the slab starts to lose coherence and breaks up into several pieces by necking (Figs. 3.S5d to 3.S5f).

For $\Delta T_p = 250$ K the slab tip drips off immediately, after beginning of the simulation (Fig. 3.8a). Due to strongly decreased crustal and mantle viscosity, the respective model *A6* evolves very rapidly and only reaches an age of 6.5 Myr. By the end of the simulation, the slab has underthrust the overriding plate by ~ 160 km but only reaches a depth of 150 km; no slab bending has occurred (Figs. 3.8c and 3.10d).

Increasing ΔT_p therefore leads to an increase in subduction speed, and earlier and more frequent necking of the slab, which finally results in destabilisation (breaking down) of the subduction process.

3.3.2.3 Variations in geometry and composition of the accretionary prism

Both geometry and composition of the accretionary prism are changing with changing ΔT_p . In the Phanerozoic model *A0* ($\Delta T_p = 0$ K), the accretionary prism consists of a growing wedge of thickened basaltic upper crust topped by a thickening sediment layer (Fig. 3.12a). At greater depths, the subduction channel is composed of hydrated crustal rocks and serpentinised overriding lithospheric mantle forms between the plates, thus lubricating the subduction process (Fig. 3.12a). With ongoing subduction, the size of the accretionary prism is reduced and the subduction channel is thinned (Fig. 3.12b).

At a small increase in $\Delta T_p = 50 - 100$ K, directly after subduction initiation, the overriding plate is slightly buckled close to the wedge. This leads to the formation of a serpentinite pocket (i.e. pocket-like subduction channel) between the subducting oceanic crust and the hydrated continental crust, which is filled by serpentinised lithospheric mantle peridotite intermixed with subducted oceanic crust and hydrated continental crust (Fig. 3.12c). With increasing mantle potential temperature, the lower crust of the overriding plate tends to delaminate after subduction initiation, which enables the formation of larger serpentinite pockets between subducting oceanic crust and overriding continental crust. Compared to model *A0*, a thick sedimentary wedge is formed during later stages of subduction which persists until the collisional stage (Fig. 3.12d).

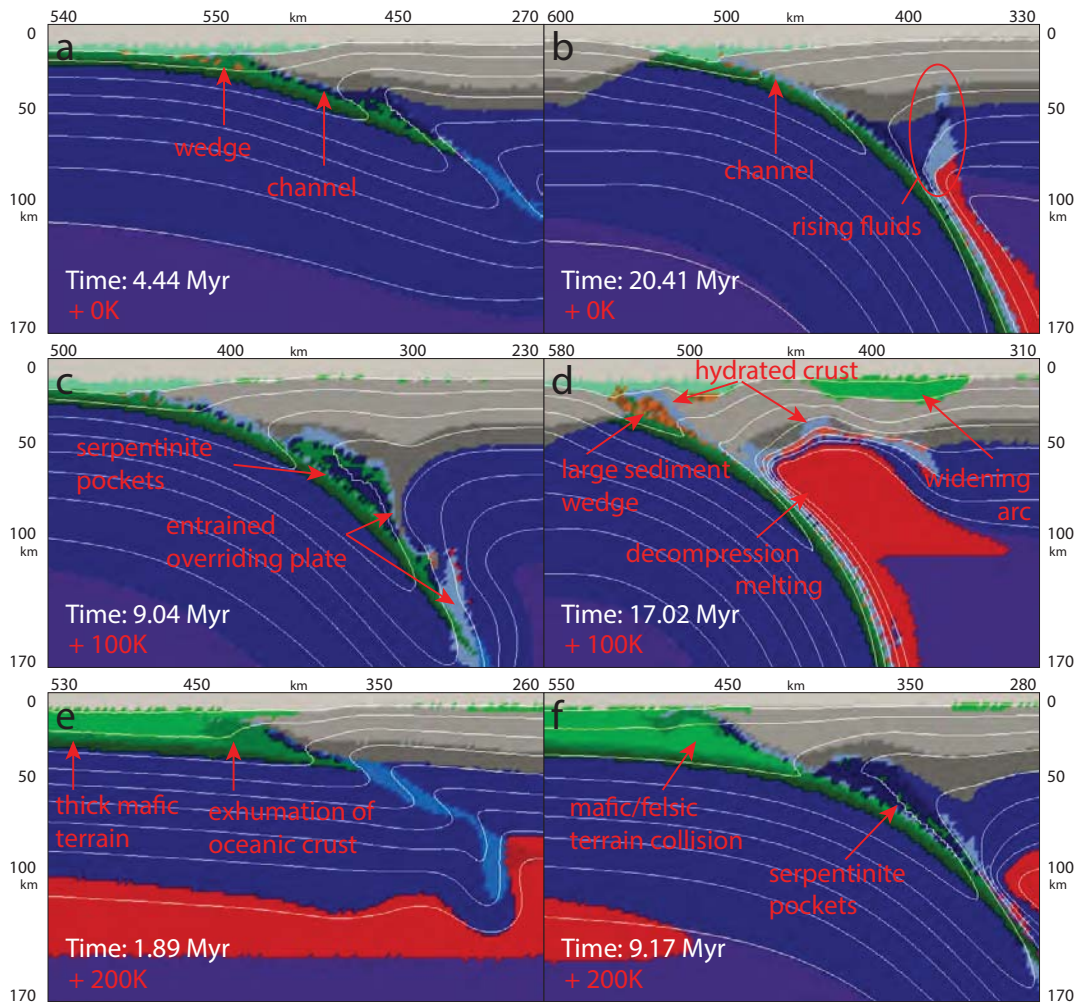


Figure 3.12: Variation of the accretionary prism and mantle wedge with increasing ΔT_p is shown in 2D slices of the reference models at an early ((a),(c),(e)) and later ((b),(d),(f)) stage of model development. Position of the slice corresponds to profile B in Fig. 3.1.

For $\Delta T_p = 150 - 175\text{K}$ new crust formed by volcanic processes plays a major role in both formation and composition of the accretionary prism. In model *A5* ($\Delta T_p = 175\text{K}$) large parts of the ocean floor are covered by mantle-derived basalts very early in the subduction process and this is reflected by the accretionary prism which mainly consist of newly formed volcanic rocks and oceanic upper crust. Compared to lower temperature models, the crustal accretionary wedge can grow much thicker, however no significant sedimentary component is present in this wedge. Only a thin subduction channel is formed between the plates which mainly consists of serpentinised mantle peridotite.

At the two highest temperatures we modelled ($\Delta T_p = 200 - 250$ K), the layer of newly formed basaltic crust on top of the original oceanic crust grows extremely thick. Therefore, after a very short timespan of only 2 Myr, the oceanic crust reaches the same thickness as the overriding continental crust (i.e. 40 – 50 km). The accretionary wedge has a large size and superposition of newly formed mafic volcanic crust over the continental margin can be observed (see Fig. 3.12e). After 9 Myr the ‘wedge’ bears resemblance to an internally deformed collisional orogenic structure, as can be seen from Fig. 3.12f.

3.3.2.4 Variations in geometry and composition of the forearc region

In the present day model *A0*, a clearly defined subduction channel forms early in the model development (Fig. 3.12a). Almost no material from the overriding plate is entrained into the subduction. The overriding plate remains strong and nearly undeformed, even close to the trench. A volcanic arc starts to develop at around ~ 13 Myr and the forearc section is separated from the overriding plate, however it still remains structurally intact (see Figs. 3.11b and 3.12b).

At an increased mantle temperature $\Delta T_p = 100$ K, delamination of both lithosphere and lower crust of the overriding plate can be observed already at an early stage of subduction (see Figs. 3.10b, 3.11c and 3.12d for details). During this process partially molten and hydrated mantle wedge material ascends from the slab (Fig. 3.10b). This weakens the structural integrity of the forearc (Fig. 3.11d). As the slab starts to retreat and partially molten asthenosphere moves into the opening gap between the subducting and overriding plates (Figs. 3.S2c and 3.12d), the forearc is further weakened and thinned until the collisional stage is reached (Fig. 3.11d).

For $\Delta T_p = 175$ K the forearc region is weakened by strong flood basalt style volcanism in combination with a growing region of partially molten mantle wedge below the arc (Figs. 3.7b and 3.7c). Due to the fast slab retreat (see also Section 3.3.2.1), no clear arc is formed and the forearc region is further thinned, weakened and stretched. This pattern continues at higher mantle potential temperatures where the whole forearc region is completely ‘reworked’ over the course of the model (Figs. 3.S5 and 3.7).

3.3.2.5 Variations in arc and backarc region

In all models, the upper surface of the plunging slab is hydrated and partially molten (Figs. 3.S1 to 3.S3 and 3.S6). As the slab penetrates deeper into the mantle, it continuously drags down hydrated oceanic crust which releases water at depths hydrating overriding mantle wedge peridotite and thus lowering its melting temperature. This well known fluid-fluxed melting mechanism (Bouilhol et al., 2015, and references therein) permits partial melting of the peridotite atop the slab. Hydrated, partially molten mantle peridotite is positively buoyant compared to the surrounding mantle and with ongoing subduction therefore rises up against the slab motion (Fig. 3.10a). This upwelling material starts to penetrate and break up the lithosphere of the overriding plate. At this time the first occurrence of new volcanic crust formation can be observed above the upwelling partially molten mantle region which can be interpreted as subduction-related arc volcanism.

In the Phanerozoic model, hydrated peridotite with subordinate volume of partially molten hydrated mantle rises from the slab roughly 100 km from the trench in a linear pattern, penetrating the crust in the form of a thin wedge. Only a small amount of newly formed crust is produced, forming a narrow but well defined linear arc (Fig. 3.5c).

With increasing ΔT_p , the amount of partial melt formed from hydrated mantle peridotite increases. Below the young arc, a broad partially molten mantle region forms with size and volume largely depending on mantle temperature and which is fed by partially molten hydrated mantle rising from the subducting slab top (see Figs. 3.6b and 3.6c). Slab retreat (see Section 3.3.2.1) leads to a less clearly defined arc which spreads over a wider region. The backarc region is extended and a backarc-basin forms which is filled by basalts derived from decompression melting of rising asthenosphere. At $\Delta T_p = 100$ K a 80 km wide, relatively shallow arc crust is formed in this manner (Fig. 3.12d).

For high ΔT_p a large area of partially molten mantle forms below the arc region (Fig. 3.S3a), which produces a rheologically weak gap between the overriding plate and the slab, and allows for the formation of large amounts of volcanic rock. With ever increasing temperature, the arc grows in width. In model *A5* ($\Delta T_p = 175$ K) no penetration of the crust by rising hydrated and partially molten mantle is observed and

new crust is formed over a much wider area, but with smaller thickness (Fig. 3.7c). In model *B4h* ($\Delta T_p = 200$ K, see Table 3.S1 and Figs. 3.S5 and 3.S6) due to the fast slab retreat, no pronounced linear arc is formed but the trench is followed directly by a broad region of overriding plate extension and intense distributed basaltic volcanism (Figs. 3.S5c to 3.S5e).

With increasing ΔT_p larger volumes of arc basalts are produced which are spread over a wider area; they have a thickness of 8–12 km with maximum thickness at $\Delta T_p = 100$ K (Figs. 3.12b, 3.12d and 3.12f).

3.3.2.6 Relationship between fluid-fluxed and decompression mantle melting

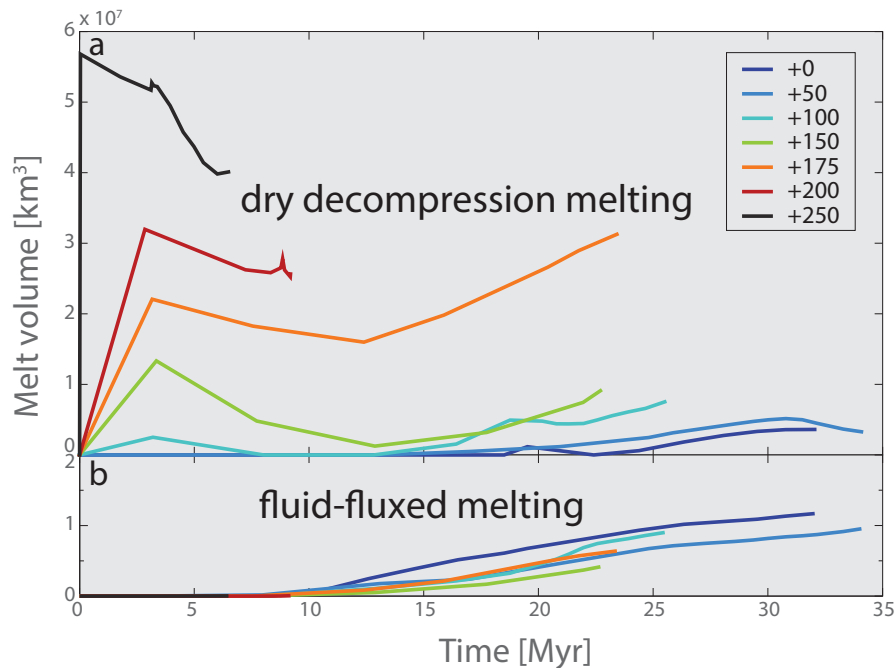


Figure 3.13: For all models *A0* - *A6* with $\Delta T_p = 0 - 250$ K in the top panel, (a) the total volume of partially molten mantle produced by dry decompression melting is shown (comprised of Figs. 3.S12c, 3.S12j and 3.S12k). (b) In the bottom panel the volume of partially molten mantle produced by fluid-fluxed melting is shown (comprised of Fig. 3.S12l). Partial melt from newly formed crust is not considered. A detailed analysis of volume change by composition for all fluids is given in Fig. 3.S12

There are two different melting mechanisms considered by our models. Fluid-fluxed melting can only occur in hydrated crustal and mantle rocks, and predominantly occurs on top of the downgoing slab which acts as a continuous source of water. As seen in

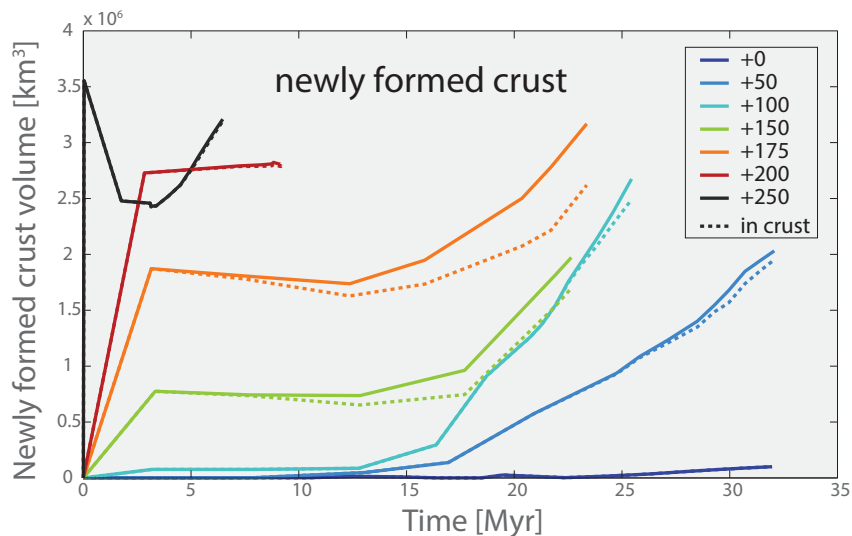


Figure 3.14: The total volume of volcanic rock present in the course of the model is shown in solid lines for models $A0 - A6$ with $\Delta T_p = 0 - 250$ K. The volume of volcanic rock without rocks subducted to depths > 50 km is shown in dashed lines. Eroded material was not considered. A detailed analysis of volume change by composition for all solids is given in Fig. 3.S11

Fig. 3.13b, hydrated partial melt first appears at ~ 10 Myr. Its volume continuously increases but no significant systematic changes with increasing ΔT_p can be observed. Models with $\Delta T_p = 200$ and 250 K never reach a model age of 10 Myr and no subduction is initiated. Therefore almost no hydrated partial melt is formed in these models. A second melting mechanism is dry decompression melting. Decompression melting mainly occurs in sublithospheric zones of upwelling hot mantle and the source material is predominantly dry asthenosphere. From Fig. 3.13a two maxima of dry melting can be identified (though the second maximum is not reached). The early maximum is related to initial mantle temperature conditions. With increasing ΔT_p the volume of dry partial melt present in the asthenosphere increases because the region where the geotherm crosses the peridotite solidus increases in size. The amount of partially molten dry mantle decreases after formation of the new thick basaltic crust at the surface (Figs. 3.13a and 3.14), which increases lithostatic pressure in the asthenosphere and thus decreases the extent of dry decompression melting. From ~ 12 Myr the dry partial melt volume increases again because in the mantle wedge above the slab, a growing area of partially molten mantle is developing due to the overriding lithosphere thinning (see e.g. Fig. 3.12d). Decompression melting of the mantle wedge cannot be observed for $\Delta T_p = 0$ K and is only a very minor effect at $\Delta T_p = 50$ K. However with increasing ΔT_p , the area of dry decompression melting in the mantle wedge is

noticeably growing and for $\Delta T_p \geq 150 \text{ K}$, decompression melting of sublithospheric mantle also occurs away from the mantle wedge in increasing volumes (Fig. 3.8c).

In the Phanerozoic model, fluid-fluxed melting is dominant and partial melting mainly occurs on top of the downgoing slab. In models with an increased ΔT_p , decompression melting mechanisms become increasingly more important. At lower $\Delta T_p = 50 - 150 \text{ K}$ it is still confined to the mantle wedge and leads to the formation of a wider arc as discussed above in Section 3.3.2.5. For $\Delta T_p = 150 - 250 \text{ K}$ decompression melting occurs along the entire LAB surface and extensive broadly distributed basaltic crustal growth shows characteristic of flood basalt style volcanism.

3.3.2.7 Variations in volume and composition of newly formed crust

With increasing ΔT_p the curves in Fig. 3.14 show an increasingly higher volume of the newly formed basaltic crust produced from larger volumes of partially molten asthenosphere initially present in the respective models (see Figs. 3.13a and 3.14). This broadly distributed basaltic crust growth occurs for all models with $\Delta T_p > 50 \text{ K}$ and is not confined to the subduction-related arc. For high temperature models starting out at a high volume of newly formed volcanic rock in the following quiet period, the total amount of new crust is slightly decreasing. This is both due to subduction of newly formed crust (see Fig. 3.14, dashed lines) and due to the simplified erosion model, which instantaneously removes volcanic rocks deposited above the prescribed erosion level. In Fig. 3.14 the change in slope at around 12–15 Myr marks the onset of arc volcanism where large volumes of crust are produced, confined to the relatively small area of the volcanic arc. The difference between a solid and a dashed line in Fig. 3.14 indicates the amount of subducted new crust and is growing with increasing ΔT_p . As arc volcanism is confined to the overriding continental plate, we can conclude that at high ΔT_p , not only are large amounts basaltic new crust formed on the oceanic plate and in the trench but also increasing volumes are subducted. The very high temperature models *A4* and *A6* with $\Delta T_p = 200$ and 250 K are again an exception where self-sustained modern-style subduction is never initiated. Arc volcanism or subduction of newly formed crust can therefore not be observed in these models. For model *A6* bending of the oceanic plate from two sides leads first to erosion of the newly formed crust (Figs. 3.8a and 3.8b) and later to increased formation of volcanic crust (Figs. 3.8c and 3.14). Figs. 3.13 and 3.14 have been produced in post-processing and are, therefore, of coarser time resolution.

3.3.2.8 Variation in structural behaviour of the crust and mantle lithosphere

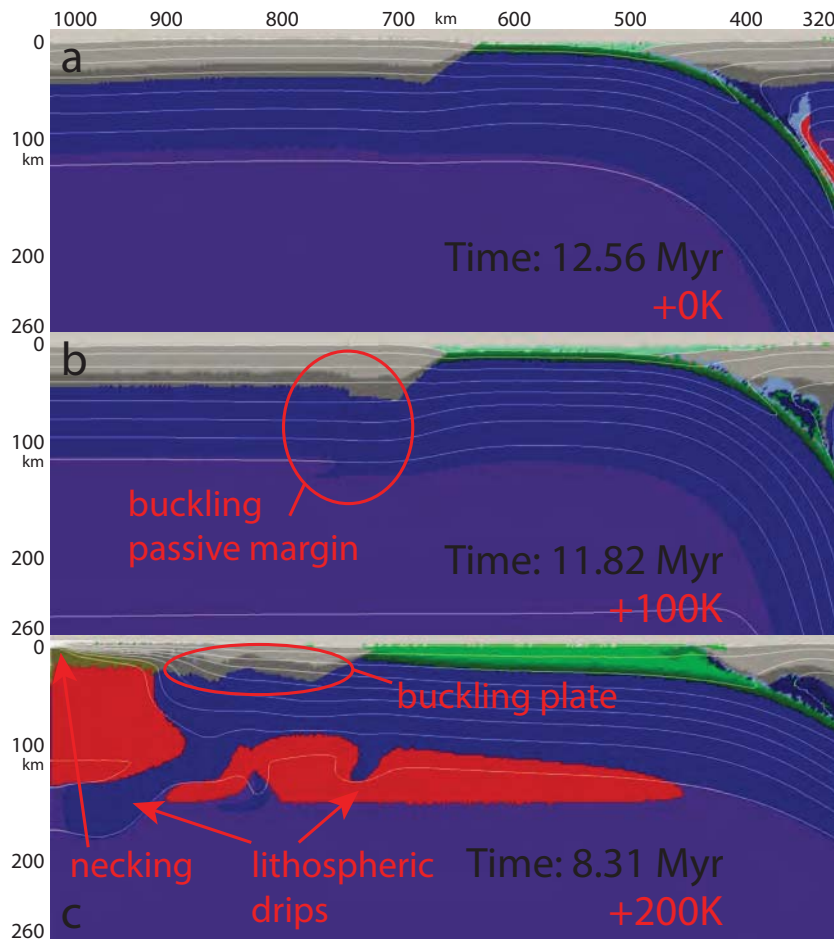


Figure 3.15: Evolution of the passive margin with increasing ΔT_p is shown in 2D slices of the reference models. Position of the slice corresponds to profile B in Fig. 3.1.

In the present-day model, the plates move as a rigid entity, leaving the crust nearly undeformed. However at increased ΔT_p the compressional setup leads to buckling in the continental crust of the subducting plate and delamination of the overriding crust close to the subduction zone. At $\Delta T_p = 100$ K a slight buckling of the subducting continental crust can be observed which shows its already weakened state (Fig. 3.15b). At $\Delta T_p = 150$ K the overriding crust is strongly buckled also away from the subduction zone and the lower crust starts to delaminate. Similar behaviour is observed at $\Delta T_p > 150$ K. This behaviour, which leads to a deformed and inhomogeneous base of the crust, is rheologically mirrored by buckling of the lithosphere, producing planar sheet-like or cylindrical drips (Figs. 3.7b, 3.7c and 3.8c).

Further indication for the increasingly weakened rheological state of the plates is given by the passive margin. The connection between oceanic and continental plate in the subducting plate shows almost no indication of the applied stress in the present-day model (Fig. 3.15a). With increasing ΔT_p the continental crust in the passive margin zone is thickened due to compression (Fig. 3.15b). For $\Delta T_p = 150$ K and higher, the passive continental margin is typically pushed down into the mantle, starting a symmetrical subduction of the oceanic lithosphere from both ends (see Fig. 3.S5).

In several models with an increased $\Delta T_p > 100$ K (in one case *B2* – see Table 3.S1 – even for $\Delta T_p = 100$ K) it can be observed that above a zone of strong mantle upwelling, the lithosphere becomes strongly thinned and partially molten until hot partially molten asthenospheric mantle directly reaches the crust (Figs. 3.7c and 3.15c). At this point the lower crust starts to melt (Fig. 3.S3c) and the once structurally coherent plate is effectively broken into two fragments. This necking process can be observed in both continental and oceanic plates as well as in the subducting and overriding plate. It preferentially appears on the left or right model boundary but can also be observed inside the model (Figs. 3.S5 and 3.11d).

All of the above described processes lead to a increasingly inhomogeneous base of the lithosphere for higher ΔT_p . For $\Delta T_p \geq 150$ K these inhomogeneities are then able to spawn thermal or thermochemical edge-instabilities which coincide with cold lithospheric mantle downwellings. These downwellings can show characteristics of either cylindrical or planar sheet-like drips (Figs. 3.7c, 3.8c and 3.15c).

3.3.2.9 Variations in the mantle flow pattern

The general mantle flow pattern, as observed in the present-day model, is very simple. Material flows in through both side boundaries and leaves through the model bottom (Fig. 3.3a). Through the course of the model this pattern mainly stays the same. The mantle downwelling in the middle of the model box becomes more pronounced and focused below the subducting slab. Additionally, during subduction, a poloidal flow around the slab tip can be observed.

Due to the different velocity boundary conditions (see Fig. 3.3 and Section 2.3), models *A1* ($\Delta T_p = 50$ K) and *A2* ($\Delta T_p = 100$ K) show slightly different convection patterns to model *A0*. However major features are consistent. The formation of two stable

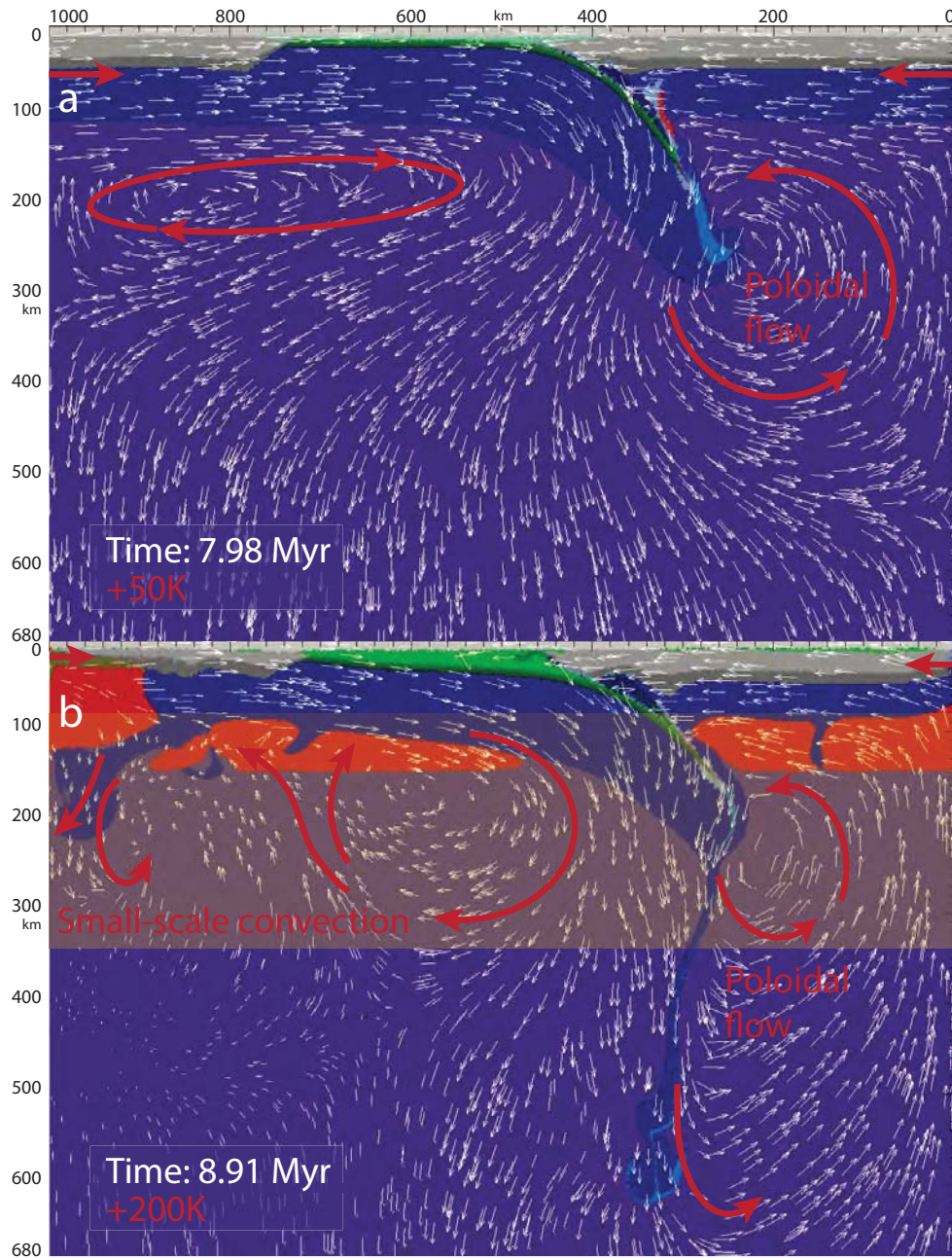


Figure 3.16: Mantle flow pattern for (a) model $A1$ ($\Delta T_p = 50$ K) and (b) model $A4$ ($\Delta T_p = 200$ K). For increased ΔT_p an area of small-scale mantle convection forms between 100 – 300 km. Position of the slice corresponds to profile B in Fig. 3.1; scales are given in Fig. 3.2a.

convection cells soon after subduction initiation can be observed. These convection cells remain stable until the collisional stage and break-off of the slab (Fig. 3.16a). Also the poloidal flow around the slab tip can be observed (Fig. 3.16a).

For $\Delta T_p > 100$ K however no stable configuration of convection can be established during subduction. The number of convection cells varies over the horizontal model extent, generally increasing with increasing ΔT_p . This small scale convection is very shallow though and limited to the uppermost ~ 300 km of the mantle (Fig. 3.16b).

3.4 Discussion

3.4.1 Geodynamic regimes of subduction and lithospheric dynamics in numerical experiments

In the following, the above-described models are grouped into four regimes for the purpose of easier description. However it should be kept in mind that no strict boundaries are observed between these regimes and gradual development from Precambrian plume-lid tectonics (Gerya et al., 2015) to present-day subduction and plate tectonics seems more likely.

3.4.1.1 Regime I: Present-day subduction $\Delta T_p = 0$ K

The first regime is used as a reference case for present-day subduction (see Section 3.3.1 and Fig. 3.5) and can nowadays be observed globally in different stages e.g. the Andes or the Himalayas.

3.4.1.2 Regime II: Dripping subduction $\Delta T_p = 50 - 100$ K

The second regime is still very similar to present-day subduction and at increased mantle temperatures of $50 - 100$ K the large-scale subduction process still operates in the same manner as at the present-day mantle temperature (see Fig. 3.6 for an overview). However there are clear indications of plates weakened by increased temperature, such as buckling of the subducting plate (Fig. 3.15b), incipient delamination of the lower crust in the overriding plate (Fig. 3.10b), increasingly earlier drip-off from the slab tip (Fig. 3.18), incipient necking of the slab (Fig. 3.11d) and larger volumes of partially molten asthenosphere (Fig. 3.13). Drip-off from the subducting slab (see Fig. 3.6b) can

occur repeatedly during the subduction process. With increasing mantle temperature the first drip-off from the slab tip occurs earlier after subduction initiation (Fig. 3.18). Due to the short model runtime no slab break-off can be observed (apart from the slab break-off and subsequent opening of a slab window directly below the orogen e.g. in Fig. 3.5c). However weakening of the slab at higher temperatures Fig. 3.11d suggests that slab break-off could occur for a longer model runtime. This has already been observed by van Hunen and van den Berg (2008) and Moyen and van Hunen (2012).

We call this regime ‘dripping subduction’ as it is characterised by a stable subduction zone which is still very similar to present-day subduction but with multiple drips from the slab tip and possible slab break-off. Van Hunen and van den Berg (2008) and Moyen and van Hunen (2012) found what can be called ‘episodic subduction’ when they observed multiple slab break-off under similar conditions. We therefore suggest that our observed dripping subduction regime could correspond to episodic subduction at its early stage.

3.4.1.3 Regime III: Transitional mode $\Delta T_p = 150 - 200$ K

In a third regime, active primarily at a mantle potential temperature increase of $\Delta T_p = 150 - 200$ K, the tectonic process shows (see Fig. 3.7) both features of subduction (Sections 3.4.1.1 and 3.4.1.2) as well as plume-lid tectonics (Section 3.4.1.4). In this transitional mode, the slab tip starts to weaken and neck off very rapidly after the subduction initiation, although not fast enough to terminate the formation of a slab. At $\Delta T_p = 200$ K (e.g. model *B4h* as shown in Table 3.S1 and Figs. 3.S5 and 3.S6) the subducting slab warms up rapidly and eventually becomes entrained in mantle convection and loses coherency. Additionally with increasing temperature the subduction becomes ablative (two-sided) (e.g. Davies, 1992) and increasingly large portions of overriding mantle lithosphere and lower continental crust become entrained into the subduction process. This leads to an increasingly two-sided geometry of the subduction zone, though still noticeably asymmetrical (Figs. 3.S5, 3.11c and 3.11e).

The two stable large-scale convection cells, present at the left and right side of the slab at lower mantle temperature (Fig. 3.16a), break up into a series of multiple smaller convection cells forming directly below the LAB (Fig. 3.16b). These convection cells are very non-stationary and are also associated with increasingly laterally inhomogeneous

temperature distribution at the base of the lithosphere. Above mantle downwellings thermochemical instabilities form, which produce drips of cold lithosphere into the asthenospheric mantle (Figs. 3.S5 and 3.7c).

3.4.1.4 Regime IV: Plume-lid tectonics $\Delta T_p > 200$ K

For increases in the upper mantle temperature of $\Delta T_p = 200$ K or higher, subduction is no longer observed even in our kinematic modern-style subduction setup (see Fig. 3.8). Instead a new tectonic style emerges which is strongly dominated by an up- and downwelling intensely convecting mantle which interacts with the internally deforming (non-subducting) lithospheric lid. Intense volcanism is no longer constrained to volcanic arcs but forms extensive planes of newly formed mantle-derived mafic (basaltic) crust (see Fig. 3.8c but also Fig. 3.S10). Oceanic and continental crust grow to roughly the same thickness which strongly hinders subduction. Strong mantle return flow leads to melting at the edges of the model and breaks up the lithosphere, thus precluding its plate-like behaviour.

This geodynamic regime, usually named ‘plume tectonics’, ‘plume-lid tectonics’ or ‘heat-pipe regime’, has been previously discussed (Hamilton, 1998; Smithies et al., 2003; Herzberg, 2014) and modelled (Vlaar et al., 1994; Johnson et al., 2014; François et al., 2014; Gerya et al., 2015) by several authors. Van Kranendonk (2011) also proposed a very similar conceptual model to describe the asthenospheric mantle formation of the Barberton Greenstone belt in South Africa as well as the East Pilbara Terrane in Western Australia. Van Kranendonk (2010) and Hill et al. (1991) discuss a similar model for the Yilgarn Block of Western Australia. Recent studies also show the onset of subduction-like dynamics from plume-lid tectonics (Sizova et al., 2015; Gerya et al., 2015). In this chapter our aim was to start at the present-day end-member, plate tectonics, and find possible tectonic regimes and transitions from plate tectonics to plume-lid tectonics. The present-day plate-tectonics-like setup (Figs. 3.1 and 3.2) is obviously unsuitable for proper investigation of plume-lid tectonics (Sizova et al., 2015; Gerya et al., 2015; Fischer and Gerya, in press).

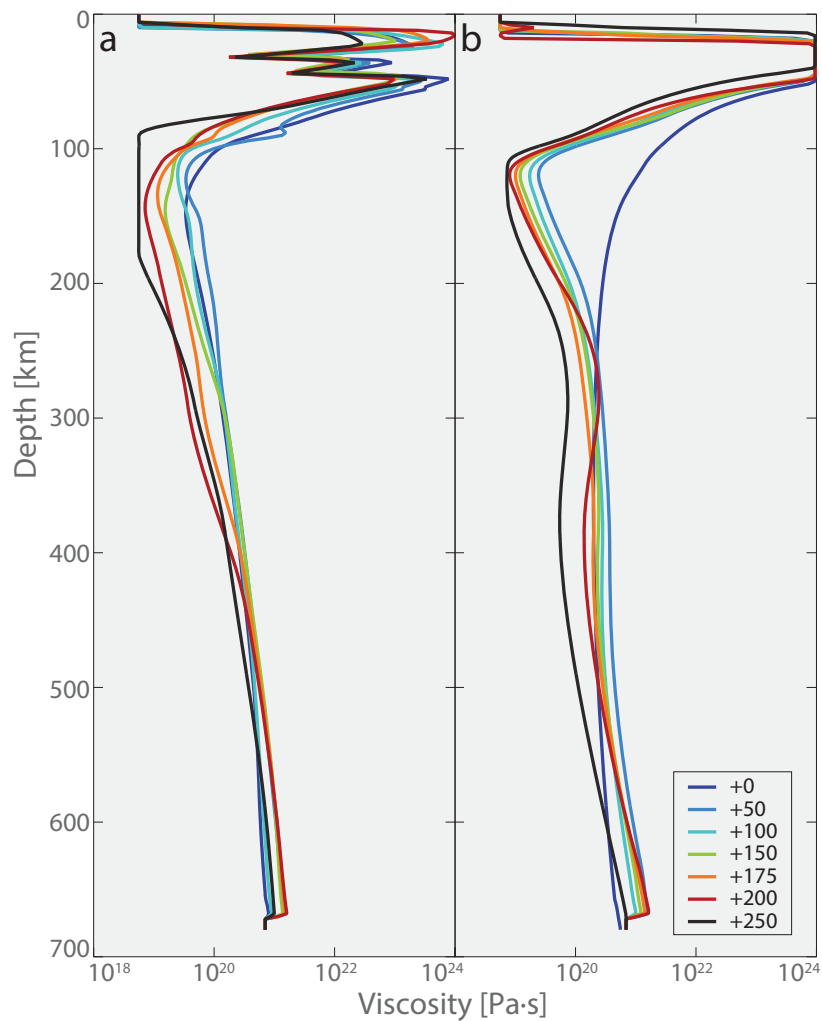


Figure 3.17: Effective (visco-plastic) viscosity profiles for both (a) continental and (b) oceanic lithosphere at $\Delta T_p = 0 - 250$ K corresponding to reference models *A0* to *A6* (at 4.4 Myr, 3.1 Myr, 3.2 Myr, 3.3 Myr, 3.2 Myr, 2.8 Myr, 1.8 Myr for $\Delta T_p = 0, 50, 100, 150, 175, 200, 250$ K respectively). Position of the profiles corresponds to localities D (oceanic) and E (continental) in Fig. 3.1.

3.4.2 Linking temperature and plate strength

The main parameter which is changed between the various models here is the mantle potential temperature. Increasing the mantle temperature but keeping the surface temperature and lithospheric thickness constant produces notable steepening of the crustal and lithospheric geotherms. This affects various other parameters as well but mainly the lithospheric viscosity profile. As shown in Fig. 3.17b, below oceanic crust the viscosity drops by around one to two orders of magnitude while the strong part

of the plate thins. The same is true below continental crust (Fig. 3.17a). Due to the mantle viscosity decrease at increased mantle temperature, the base of the lithosphere starts to build drips and folds more easily. Additionally the continental strength is lowered and the connection between crust and subcrustal mantle-lithosphere as well as between upper and lower crust is weakened. This allows for easier delamination of continental crust at increased upper-mantle temperature. This effect can mainly be observed at the subduction trench where at higher temperatures, upper continental crust is also entrained in the ablative subduction process (see e.g. Fig. 3.12c).

3.4.3 Consequences of wide-spread mantle-derived magmatism

New basaltic crust formed on top of oceanic crust does not destabilise the layering. The dynamics can however be influenced due to the fact that the oceanic crust effectively becomes thicker and thus more positively buoyant. This thicker oceanic crust influences dynamics in two ways. The added thickness allows for a larger accretionary wedge to be built which hinders subduction and chokes the subduction zone. The resulting dynamics resemble a collisional process (see e.g. Fig. 3.12f) which can be found in modern continent-continent collision or island arc accretion zones.

Volcanic crust of basaltic composition however is denser than upper continental crust and thus newly formed crust formed on top of continental crust is gravitationally unstable. Large amounts of volcanic rocks erupting in a flood basalt style on top of a weakened continental crust lead to an overturn in the crust (Johnson et al., 2014; François et al., 2014). Denser mafic crust starts to sink down into the underlying felsic crust which in turn starts to dome up (e.g. Figs. 3.8c and 3.12d). This tendency seems similar to the beginning of the development of a typical dome-and-keel structure (Van Kranendonk, 2011), although longer-term 3D models with hot mantle temperature will be needed for properly investigating crustal doming processes triggered by mantle-derived magmatism.

The strong volcanism and large volume of crust formation leave behind a growing layer of depleted asthenospheric mantle effectively cooling it down and turning it into a depleted lithosphere. However, this rudimentary lithosphere is not stable under high T_p conditions and frequently drips off into the mantle. This generates a return flow and more decompression melting which in turn generates more new crust and depleted

mantle (Johnson et al., 2014).

3.4.4 Formation of small plates

Thinning and necking of the lithosphere and crust can mainly be observed at model boundaries. Thinning of the plate (as e.g. seen in Figs. 3.S3c and 3.15c) is caused by hot mantle upwelling. The process therefore occurs more often and faster at higher mantle potential temperature. At higher ΔT_p smaller scale convection cells directly below the lithosphere can also lead to thinning of the former, e.g. above the mantle wedge (Figs. 3.S2c and 3.S6e). With the given boundary conditions (Fig. 3.3b) and model box size and ratio, mantle convection is forced to form upwellings at the left and right model boundaries. Considering these limitations, the findings seem to indicate formation of smaller plates with higher ΔT_p (Sizova et al., 2010).

3.4.5 Slab break-off and initiation of cold downwellings

Figure 3.18 shows the timing of the first slab break-off or necking with different ΔT_p . At present-day mantle temperature the slab only breaks off after continental collision. For an increased ΔT_p an earlier drip off at a shallower depth indicates the start of dripping subduction. At $\Delta T_p \geq 200$ the subducting plate drips off within < 4 Myr or as soon as it enters the mantle and modern-style subduction is thus no longer possible.

For an increase in $\Delta T_p = 100$ K the slab viscosity is lowered by roughly one order of magnitude (van Hunen and Moyen, 2012). Van Hunen and Allen (2011) showed that a weakened slab leads to a shorter time delay between continental collision following slab break-off. The process of slab necking and tearing is also expedited within a weakened slab (van Hunen and Allen, 2011). Furthermore van Hunen and van den Berg (2008) showed that for increasing ΔT_p subduction becomes faster and more episodic.

At $\Delta T_p = 150$ K cold drips or Rayleigh-Taylor instabilities appear for the first time, not at the slab tip but at the base of the lithosphere (Fig. 3.18). With further increasing ΔT_p the number of ‘off-slab’ RT-instabilities appearing during the course of the model increases while the onset time decreases.

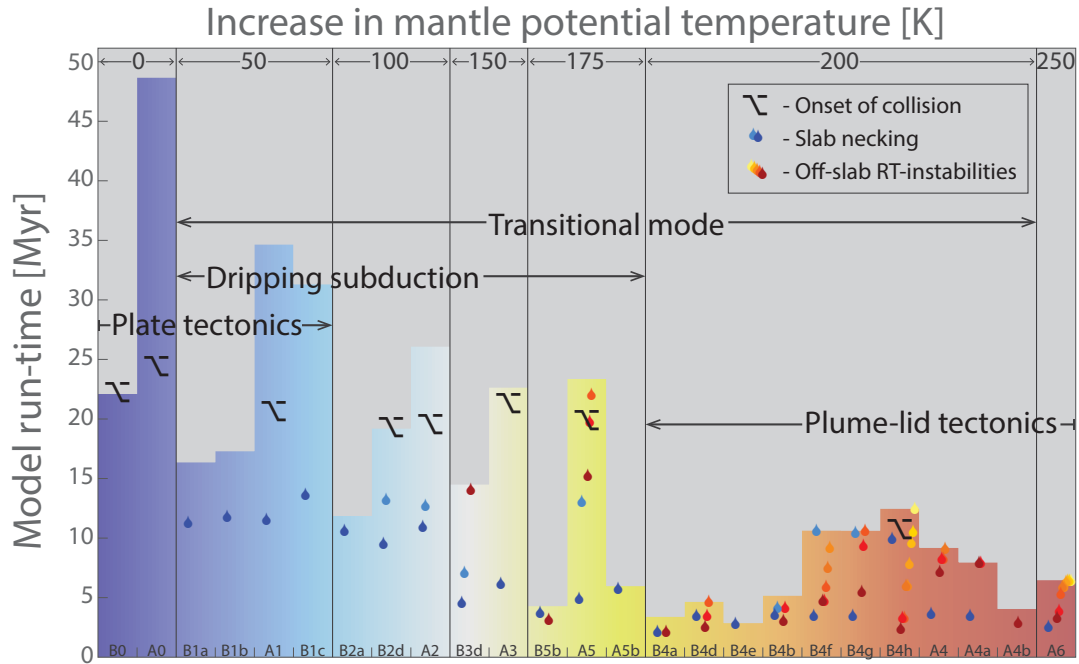


Figure 3.18: Important events during the model evolution are briefly summarised for all models in Table 3.S1. The length of the bar indicates the maximum length of the model run t_{max} . The black symbol at ~ 20 Myr indicates continental collision. Blue drips signify necking or dripping restricted to the slab tip, whereas yellow/red drips signify dripping away from the slab.

3.4.6 Factors inhibiting the subduction process

Several factors can either hinder or totally inhibit subduction. With increasing ΔT_p more lithospheric material of the overriding plate is entrained which eventually leads to a more two-sided (ablative) subduction style (Davies, 1992). Rheological weakening of the continental crust also leads to delamination of the lower crust which can slow down subduction substantially because of the low density of the continental crust. In addition, oceanic crust on the subducting plate is growing thicker and its positive buoyancy is increased which could further hinder subduction at the beginning before eclogitisation depth is reached (van Hunen and van den Berg, 2008).

Very strong crustal growth of the oceanic crust by mantle-derived magmatism can also lead to an increasing size of the accretionary prism. The subduction zone becomes locked as increasingly larger volumes of the newly-formed volcanic rocks are accreted into what starts to resemble a collisional orogen between a felsic and a mafic terrain (Fig. 3.12f and Davies (1992)).

The higher mantle temperature and subsequent weakening of a subducting slab leads to an earlier slab break-off. The major driving force of subduction (van Hunen and Moyen, 2012) is therefore effectively removed. Especially at $\Delta T_p \geq 200$ K subduction is practically impossible to start as any lithospheric discontinuity simply drips off immediately (Fig. 3.8c and Davies (1992); Smithies et al. (2003)).

3.4.7 The onset of subduction

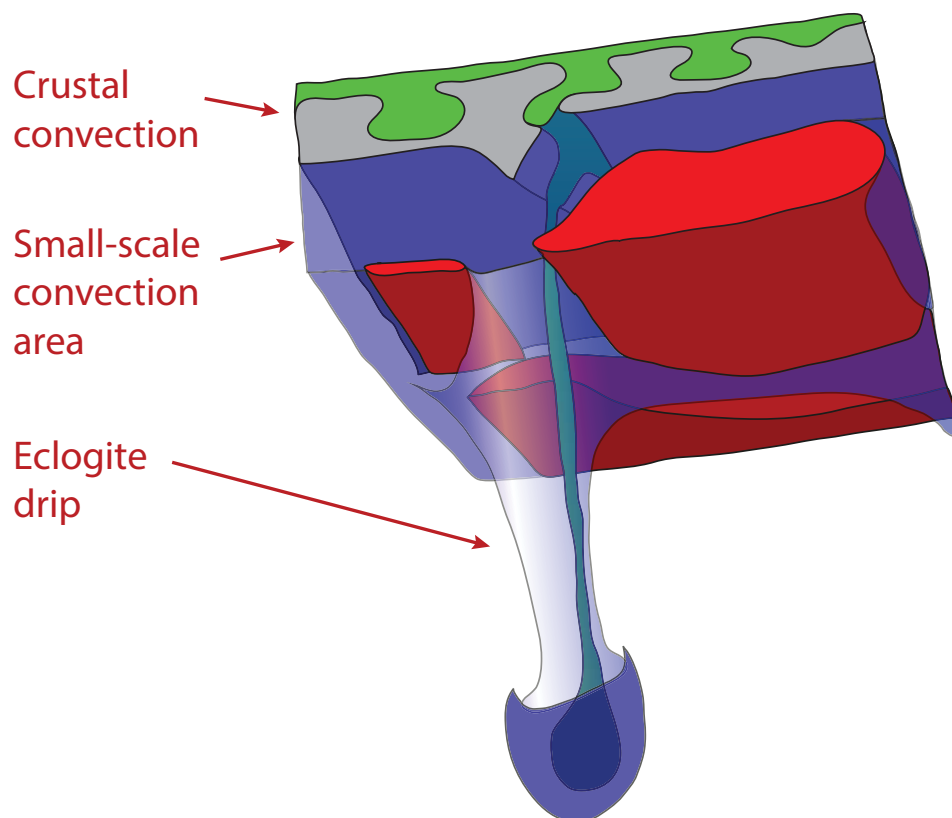


Figure 3.19: Sketch of Precambrian tectonics. The crust is dominated by diapiric overturns. Cold overthickened unstable lithosphere drips down into the mantle, initiating delamination or two-sided subduction.

One of the most strongly debated questions about early Earth tectonics is how and when did the first subduction zone initiate. To answer this questions we need to consider secular changes in global geodynamic regimes forward in time. As suggested for example by Van Kranendonk (2011) for the South African Kaapvaal craton and by François et al. (2014) for the Australian East Pilbara craton, the dominating tec-

tonic regime in the earlier Archean was plume-lid tectonics, which consists of a stable two-layer convection-system with separate crustal doming and mantle convection with a strong emphasis on vertical movement (Vlaar et al., 1994; Smithies et al., 2003; Van Kranendonk, 2011; François et al., 2014).

With decreasing ΔT_p the lithosphere and crust strengthens and more material becomes entrained by lithospheric dripping. This dripping process might indeed help to initiate horizontal motions in the crust as well. Further decrease in ΔT_p will lead to a dripping which is eventually able to entrain lower crustal material as well. At this stage, dripping therefore starts to resemble a two-sided subduction (Fig. 3.S5c and Davies (1992)). However this very early proto-subduction will remain episodic and be associated with frequent slab necking and dripping. With further cooling of the mantle colder, stronger, more coherent and longer slabs become feasible. Further decrease in ΔT_p allows the slab to be strengthened and leads to less frequent slab break-off and finally a stable subduction process (van Hunen and van den Berg, 2008; Gerya et al., 2015).

The evolutionary progression described corresponds to a gradual transition between the two end-members plume-lid tectonics in the early Archean and Subduction in the Phanerozoic. Therefore any time between the Archean and the Present may show some kind of subduction-like dynamics. However, how close to present day the transition to modern-style subduction and plate tectonics occurred, remains debatable. Our models thus suggest gradual rather than abrupt plume-lid tectonics to plate tectonics transition in the Earth's history.

3.4.8 Setup dependencies and model limitations

Knowledge of the global geodynamic style and lithospheric and crustal conditions during the Precambrian is very limited and the modern-style plate-tectonic setup explored may, therefore, be not fully appropriate for analysing the Precambrian mantle and crustal dynamics. Due to a model setup and kinematic boundary conditions which are very similar to the present day, subduction can be observed up to very high temperatures. Nevertheless subduction stability clearly breaks at roughly $\Delta T_p = 200$ K compared to present-day mantle potential temperature. Presumably, without kinematically prescribed plate motions, subduction might destabilise at even lower temperatures but this requires careful investigation based on self-consistent models with

spontaneously moving plates (e.g. Sizova et al., 2014).

At increased ΔT_p the influence of the erosion level becomes more visible. Erosion level is chosen either 8 or 4 km above the water level and continent surface which seems to inhibit formation of larger volumes of volcanic crust by instantaneous erosion in some cases. Since sedimentation in our models is in fact independent of erosion (see Section 2.3), almost no sedimentation occurs in response to the instantaneous erosional mass removal. Consequently, implementation of more sophisticated erosion/sedimentation treatment approaches would be desirable in the future. Last but not least, crustal growth in our models is assumed to be fully controlled by surface volcanism, whereas on Earth intrusive crustal accretion in the form of plutons is dominant, which calls for the use of more realistic melt emplacement algorithms (e.g. Vogt et al., 2012).

3.5 Conclusion

We varied the mantle potential temperature T_p in a 3D present-day subduction model up to $\Delta T_p = 250$ K. In models with $\Delta T_p = 200 - 250$ K we found that subduction is no longer possible and model evolution is driven by intense tectono-magmatic plume-lithosphere interactions instead. We therefore propose that the early Archean Earth was radically different and was driven by plume-lid tectonics. Its major elements are a thick crust of 35 – 50 km which is internally convecting and an unstable lithosphere which displays vigorous small-scale instabilities and thinning by dripping. Due to strong small-scale convection, larger plates are also often broken up into smaller fragments. At a lower $\Delta T_p = 150 - 200$ K models are subjected to frequent necking and dripping processes and show characteristics of both types of tectonics: Present-day subduction and plume-lid tectonics. For $\Delta T_p < 150$ K signs of plume-lid tectonics disappear. At slightly elevated temperatures of $\Delta T_p = 50 - 100$ K subduction has dripping and (possibly) episodic character and shows signs of weakened plates.

We conclude that tectonics, starting out from plume-lid tectonics, evolved gradually into what we can observe today as plate tectonics and subduction. Therefore no abrupt geodynamic regime transition point can probably be specified because subduction gradually evolved over time.

Table 3.S1: All models (Fig. 3.18) are briefly described by their main parameters. d_{c12} and d_{c1} is the thickness of the subducting continental/oceanic lithosphere and d_{c11} is the thickness of the overriding continent. d_{cc} and d_{oc} is the thickness of the continental/oceanic crust. d_{air_c} and d_{air_o} is the thickness of the sticky air layer above continental/oceanic crust. t_{max} is the model time.

Model	ΔT_p [K]	d_{c12} [km]	d_{c1} [km]	d_{c11} [km]	d_{oc} [km]	d_{cc} [km]	M_{min}, M_{max} [wt%]	P_{max} [Pa]	d_{air_o} [km]	d_{air_c} [km]	t_{max} [Myr]	Comment Regime/Fig.
A0	0	88	85	78	8	35	2, 4	-	15	12	54.17	Reference model I, Fig. 3.5
B0*	0	88	85	78	8	35	2, 4	-	15	12	22.10	Present-day model, setup B
A1	50	88	85	78	8	35	2, 2	1e10	15	12	34.66	Warm subduction, Reg. I/II,
B1a*	50	88	85	78	8	35	1, -	-	15	12	23.32	Figs. 3.5 and 3.6
B1b*	50	138	135	78	8	35	2, 2	1e10	15	12	17.30	-//-
B1c*	50	138	135	78	8	35	2, 4	1e10	15	12	44.57	-//-
A2	100	88	85	78	8	35	2, 2	1e10	15	12	26.03	Warm subduction, Reg. II, Fig. 3.6
B2a*	100	88	85	78	8	35	1, -	-	15	12	11.86	-//-
B2d*	100	108	135	78	8	35	2, 4	1e10	15	12	19.21	-//-
A3	150	88	85	78	8	35	2, 2	1e10	15	12	22.65	Early slab necking and weak plates,
B3d*	150	108	135	78	8	35	2, 4	1e10	15	12	15.73	Reg. II, Fig. 3.6
A5	175	88	85	78	8	35	2, 2	1e10	15	12	23.36	Early slab necking and dripping of
A5b	175	88	135	78	8	35	2, 4	1e10	25	22	5.96	lithosphere, Reg. III, Fig. 3.7
B5b*	175	138	135	78	8	35	2, 2	1e10	15	12	4.29	-//-
A4	200	88	85	78	8	35	2, 2	1e10	15	12	9.17	Immediate slab necking, lithospheric
A4a	200	88	85	78	20	35	2, 2	1e10	15	12	7.94	dripping, buckling of crust, Reg. IV,
A4b	200	88	135	78	8	35	2, 4	1e10	25	22	4.05	Fig. 3.8
B4a*	200	88	85	78	8	35	1, -	-	15	12	3.71	-//-
B4d*	200	108	135	78	8	35	2, 4	1e10	15	12	4.67	-//-
B4e*	200	108	135	78	8	35	2, 2	1e10	15	12	2.86	-//-
B4b*	200	138	135	78	8	35	2, 2	1e10	15	12	5.17	-//-
B4f*	200	108	135	78	8	35	2, 2	1e10	15	12	10.67	-//-
B4g*	200	108	135	78	8	35	2, 2	1e10	15	12	10.63	-//-
B4h*	200	108	135	78	8	35	2, 4	1e10	25	22	12.47	see Fig. 3.S5 and Section 3.5
A6	250	88	85	78	8	35	2, 2	1e10	15	12	6.47	Plume tectonics, Reg. IV, Fig. 3.8

* Initial model setup: Different placement of the predefined weak zone leads to the formation of a transform fault (Duretz et al., 2014, Fig.1b)

Partial melt composition for selected reference models

In the following figures, solid rocks are shown in grey scale, whereas partial melt is shown in the colour code of its solid counterpart except for partially molten hydrated mantle peridotite which is shown in red.

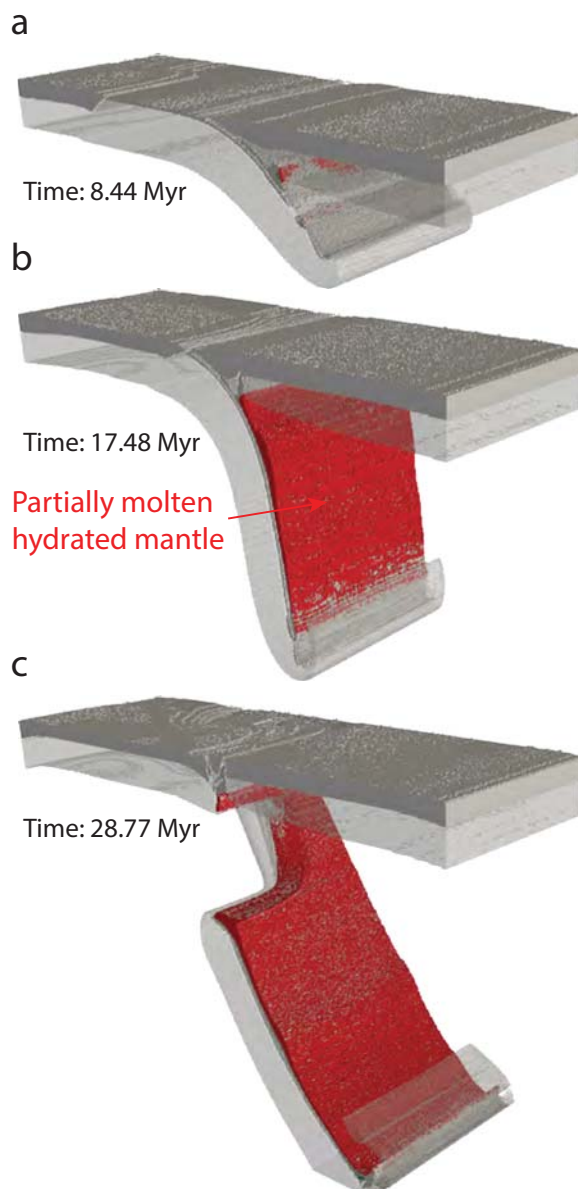


Figure 3.S1: Evolution of crustal and mantle melting for reference model $A0$ at $\Delta T_p = 0$ K. Partial melt only occurs on top of the slab in the form of partially molten hydrated mantle peridotite. See Fig. 3.5 for the full compositional evolution. Scales are given in Fig. 3.2a.

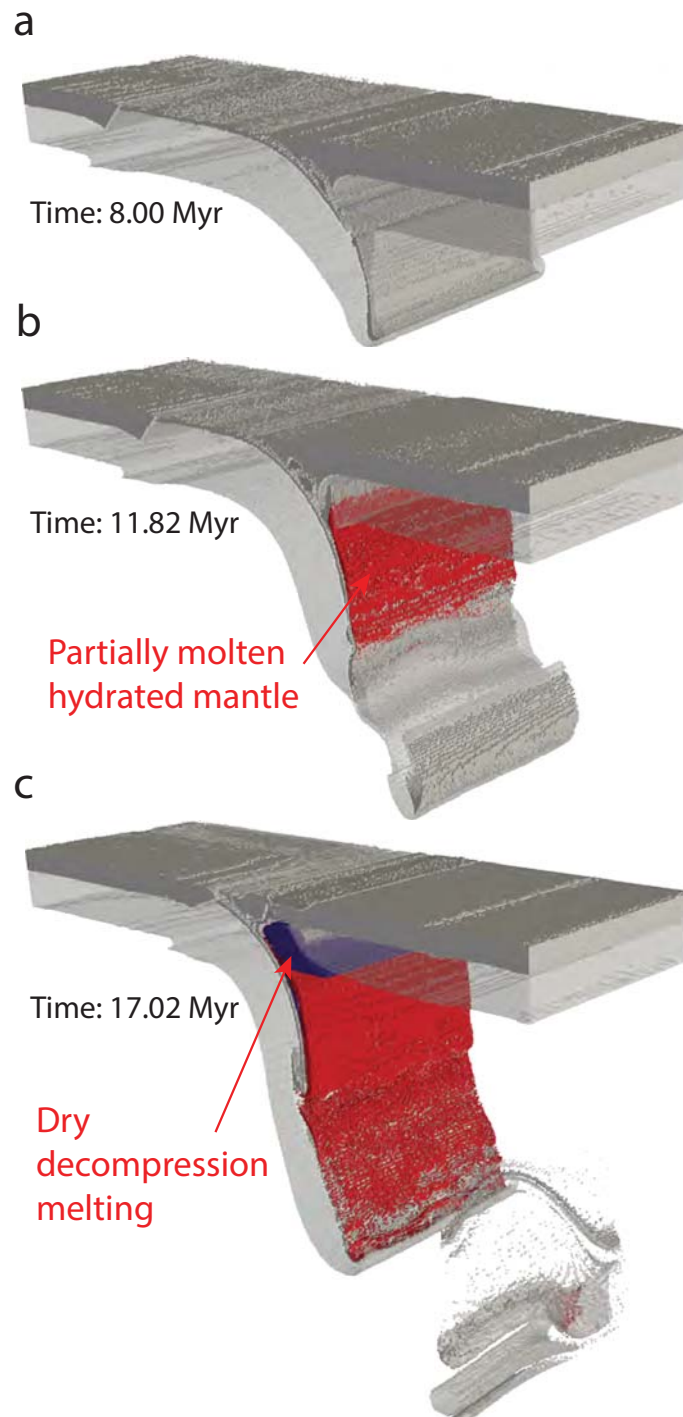


Figure 3.S2: Evolution of crustal and mantle melting for reference model *A2* at $\Delta T_p = 100$ K. (a)-(b) Partial melt mainly occurs on top of the slab in the form of partially molten hydrated mantle peridotite. (c) However the retreating slab leads to a pocket of dry partial melt by decompression melting in the mantle wedge. See Fig. 3.6 for the full compositional evolution. Scales are given in Fig. 3.2a.

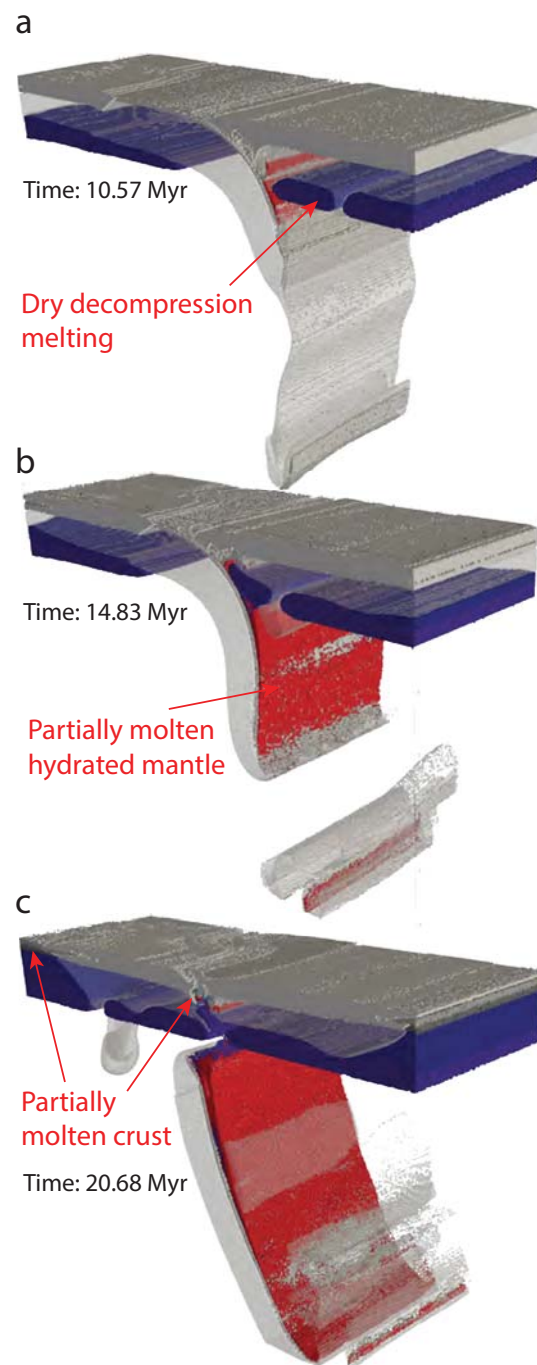


Figure 3.S3: Evolution of crustal and mantle melting for reference model *A5* at $\Delta T_p = 175$ K. (a)-(b) Fluid-fluxed melting occurs on top of the slab, producing a slab-parallel red layer of partially molten hydrated mantle peridotite. Due to the high mantle temperature, a layer of sublithospheric partially molten dry mantle peridotite is formed. (c) The partially molten hydrated mantle peridotite on top of the slab is thickening and in the collision zone partial melts of newly formed and hydrated crust appear. See Fig. 3.7 for the full compositional evolution. Scales are given in Fig. 3.2a.

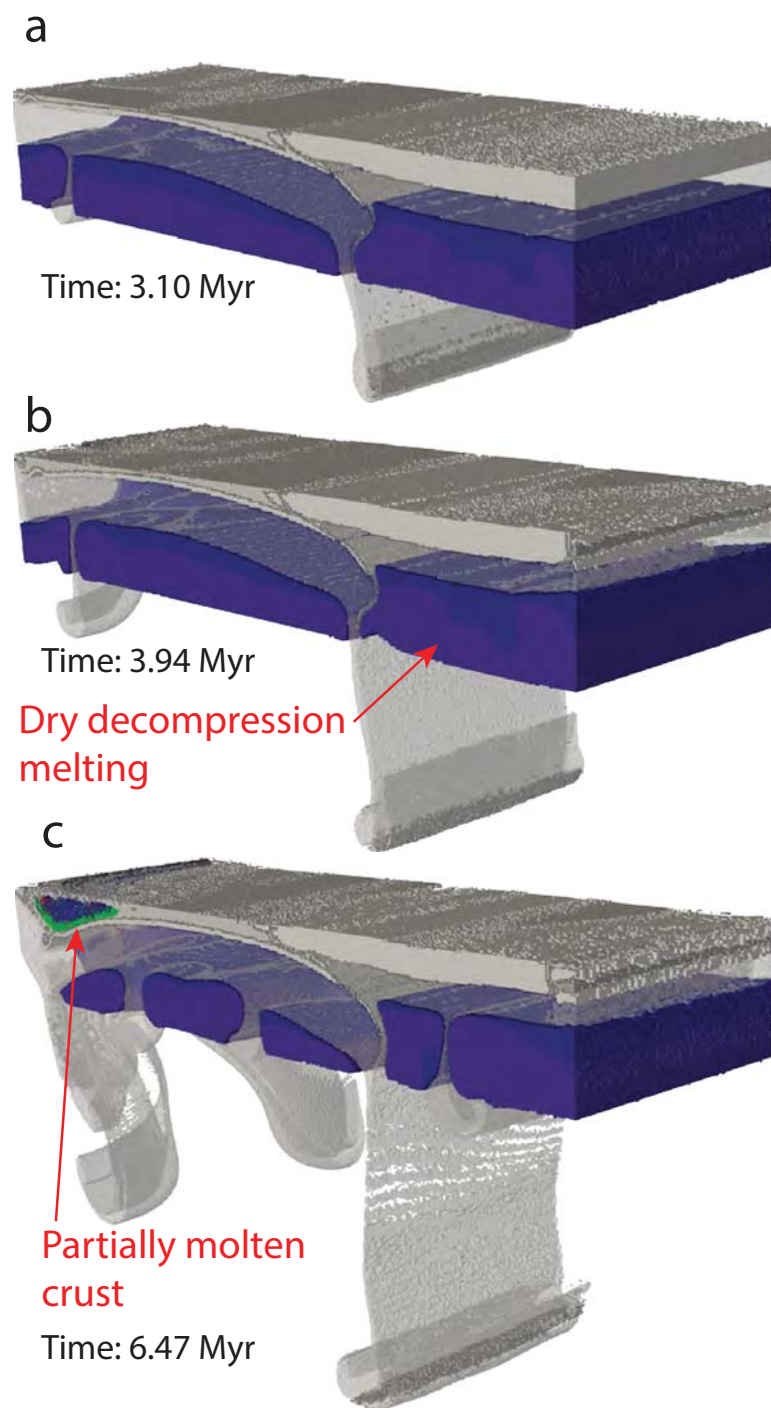


Figure 3.S4: Evolution of crustal and mantle melting for reference model *A6* at $\Delta T_p = 250$ K. As no subduction occurs, no partially molten hydrated mantle peridotite is formed. Instead a thick layer of partially molten dry mantle is generated by decompression melting. See Fig. 3.8 for the full compositional evolution. Scales are given in Fig. 3.2a.

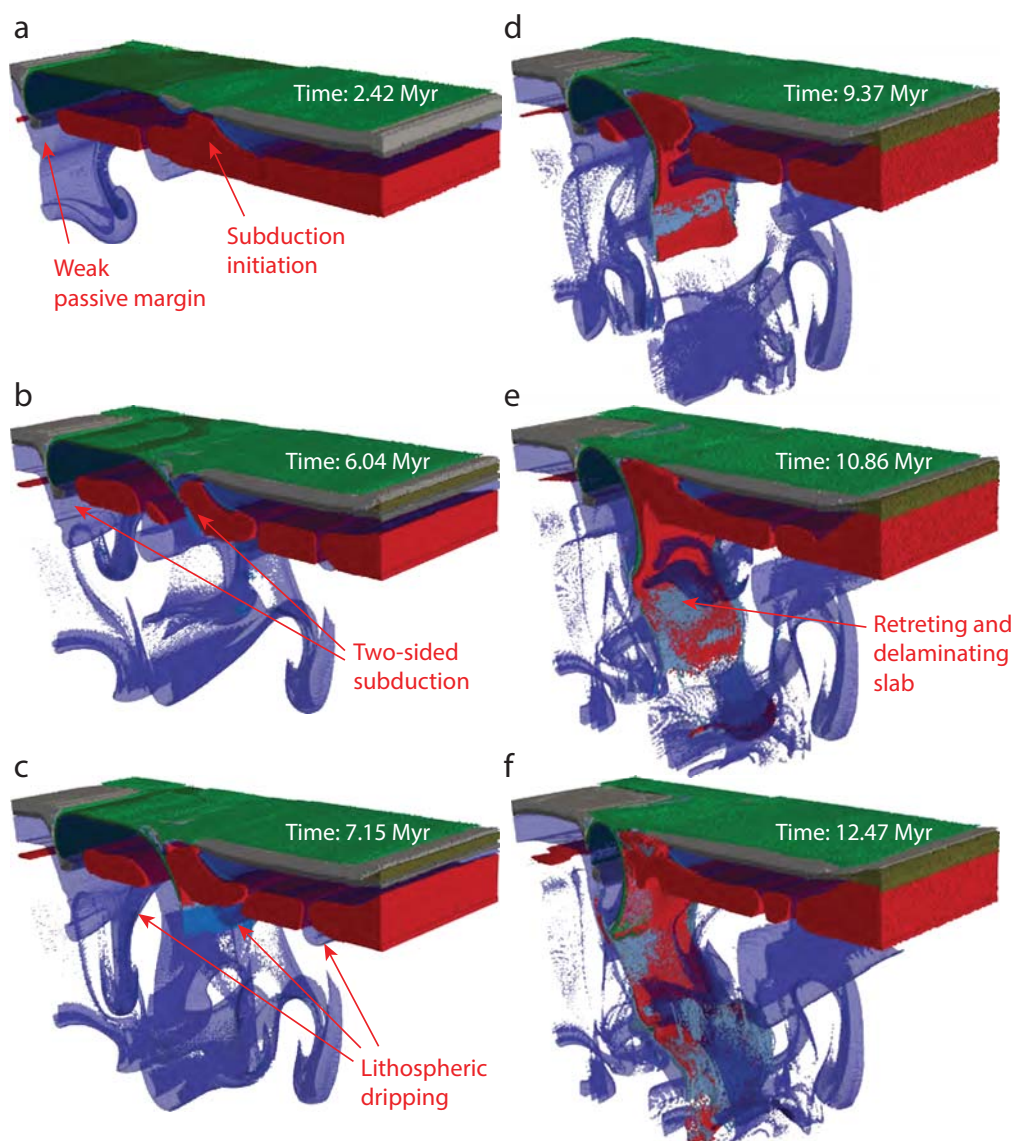
Alternative model *B4h* at $\Delta T_p = 200$ K

Figure 3.S5: Evolution of the model *B4h* at $\Delta T_p = 200$ K. The model shows (a) a weak passive margin which develops a lithospheric drip and intense non-arc-related volcanism. (b) Subduction is not initiated at the weak zone but close to it by a lithospheric drip and below the passive margin by a drip as well. Both subduction zones are two-sided. (c)-(d) Strong partial melting in the mantle wedge leads to delamination of the former oceanic plate from the new formed basaltic crust. (e)-(f) The lithospheric part of the subducting slab becomes entrained in mantle convection while the mafic crust remains nearly intact. Scales are given in Fig. 3.2a.

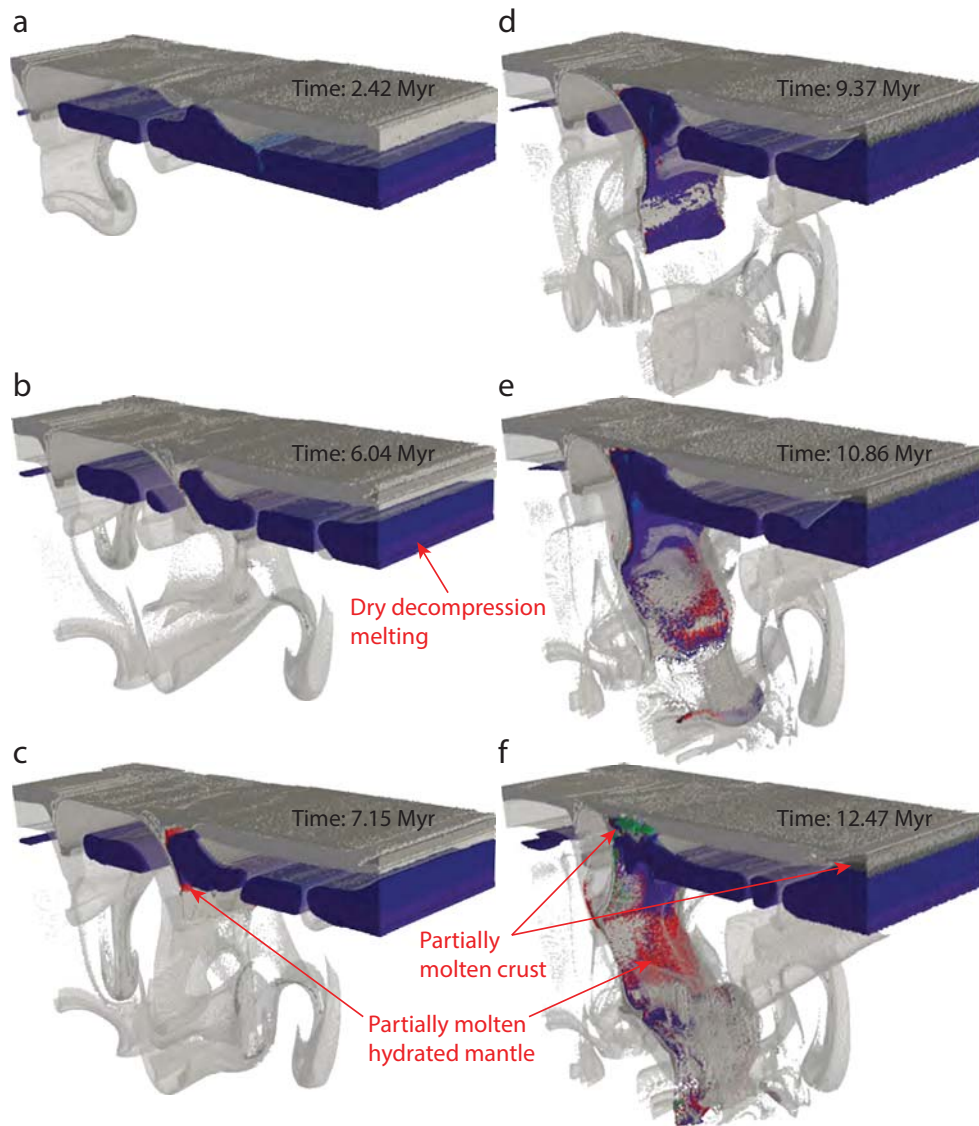


Figure 3.S6: Evolution of crustal and mantle melting for model *B4h* at $\Delta T_p = 200$ K. (a)-(b) Due to high mantle temperature, a thick layer of partially molten dry mantle peridotite is established (see Fig. 3.S4). (c) However after onset of delamination/subduction the slab releases enough water to cover it in partially molten hydrated mantle. Due to the retreating slab, decompression melting forms dry partial melt in the mantle wedge. (d)-(e) Additionally, dry partially molten mantle forms on top of the slab. (f) In the collision zone, dry partial melt of the basaltic crust forms. See Fig. 3.S5 for the full compositional evolution. Scales are given in Fig. 3.2a.

Evolution of topography for selected reference models

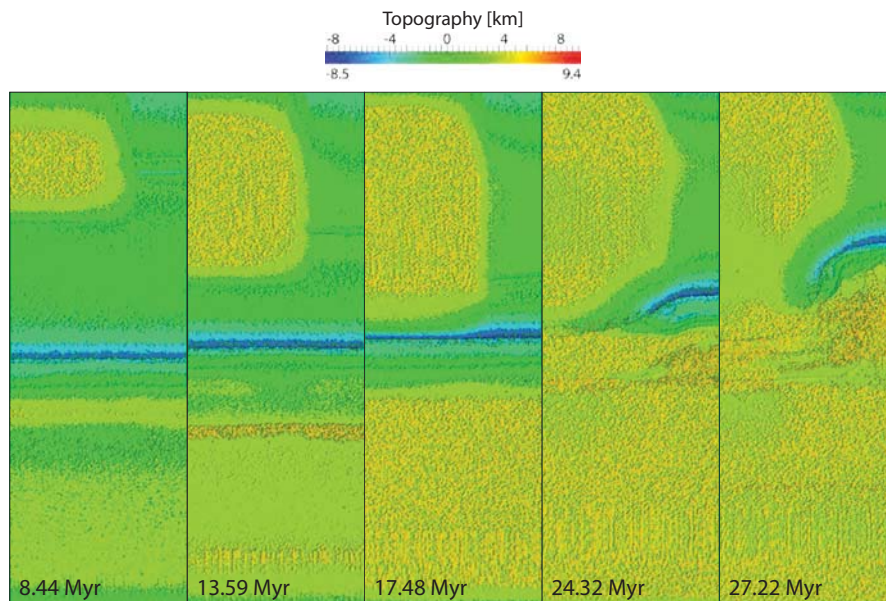


Figure 3.S7: Evolution of topography for reference model *A0* at $\Delta T_p = 0$ K. (a) A trench is formed. (b)-(c) While the trench is slightly retreating, the magmatic arc rises. (d)-(e) After collision, a STEP-boundary is formed and the trench retreats further. Scales are given in Fig. 3.2a.

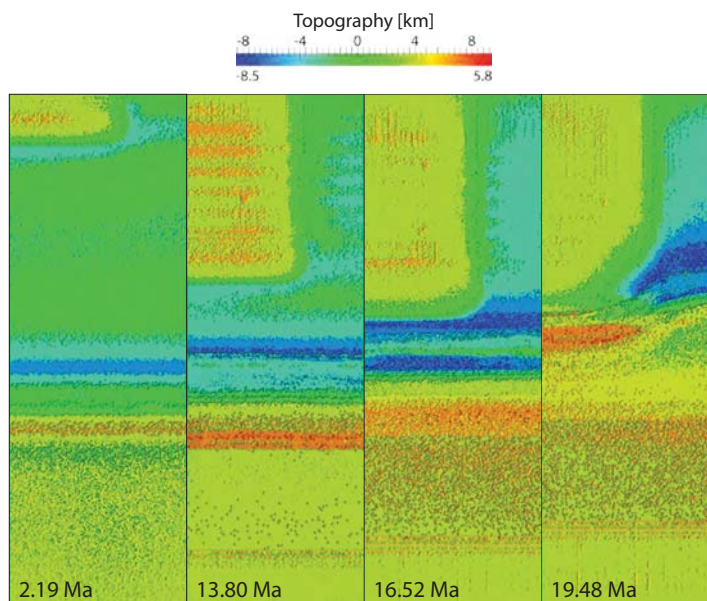


Figure 3.S8: Evolution of topography for reference model *A2* at $\Delta T_p = 100$ K. The topographic evolution of this model is very similar to the case $\Delta T_p = 0$ K shown in Fig. 3.S7. However in panel (c) two depressions are formed; this is due to the larger sediment wedge (see Fig. 3.12d). Scales are given in Fig. 3.2a.

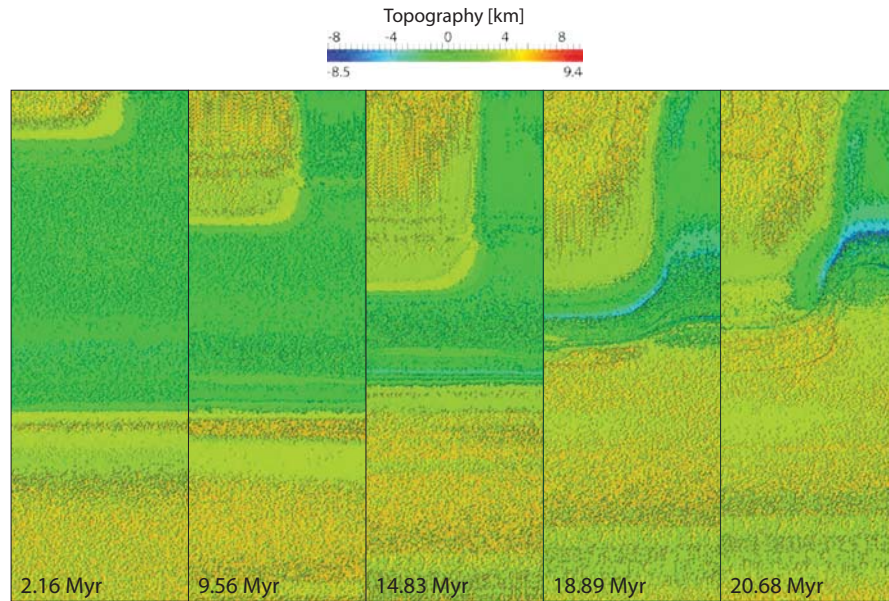


Figure 3.S9: Evolution of topography for reference model *A5* at $\Delta T_p = 175$ K. (a)-(b) No trench is formed in the early evolution of the model. Instead a relatively (compared to Figs. 3.S7b and 3.S8b) low but wide arc is forming. (c)-(e) a very shallow trench is forming and propagates as described above (Fig. 3.S7). During the course of the model, the whole surface is uplifted due to the large amounts newly formed volcanic rocks. However no large topographic differences are developed. Scales are given in Fig. 3.2a.

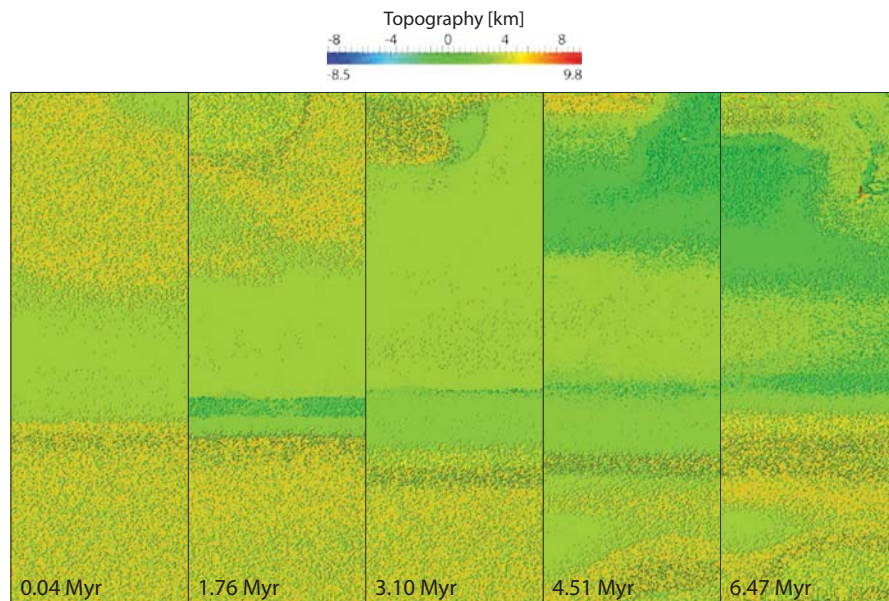


Figure 3.S10: Evolution of topography for reference model *A6* at $\Delta T_p = 250$ K. The whole surface is strongly uplifted due to the large amounts newly formed volcanic rocks. No clear trench and arc are formed and topographic differences between continental and oceanic plate are minimised. Scales are given in Fig. 3.2a.

Detailed analysis of marker volume change by composition

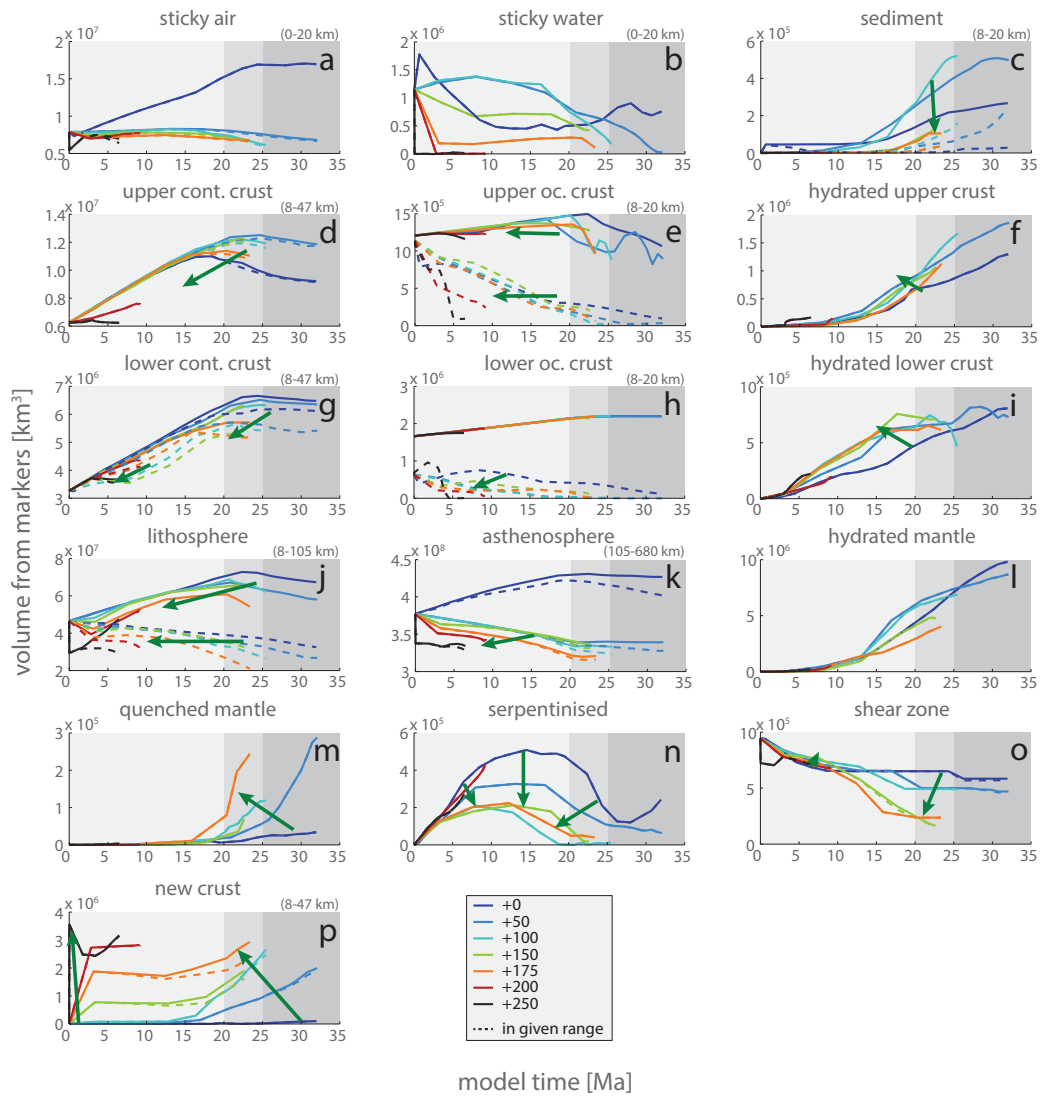


Figure 3.S11: Change in volume over the course of the model is shown separately for each solid rock type available (see Fig. 3.2b) for the whole reference model series $A0$ to $A6$ with $\Delta T_p = 0 - 250$ K. In some plots, dashed lines indicate volumes measured only within the given depth range. Additionally the volume of ‘sticky air’ and ‘sticky water’ (Section 2.3) is shown as well. Green arrows indicate the general trend with increasing ΔT_p .

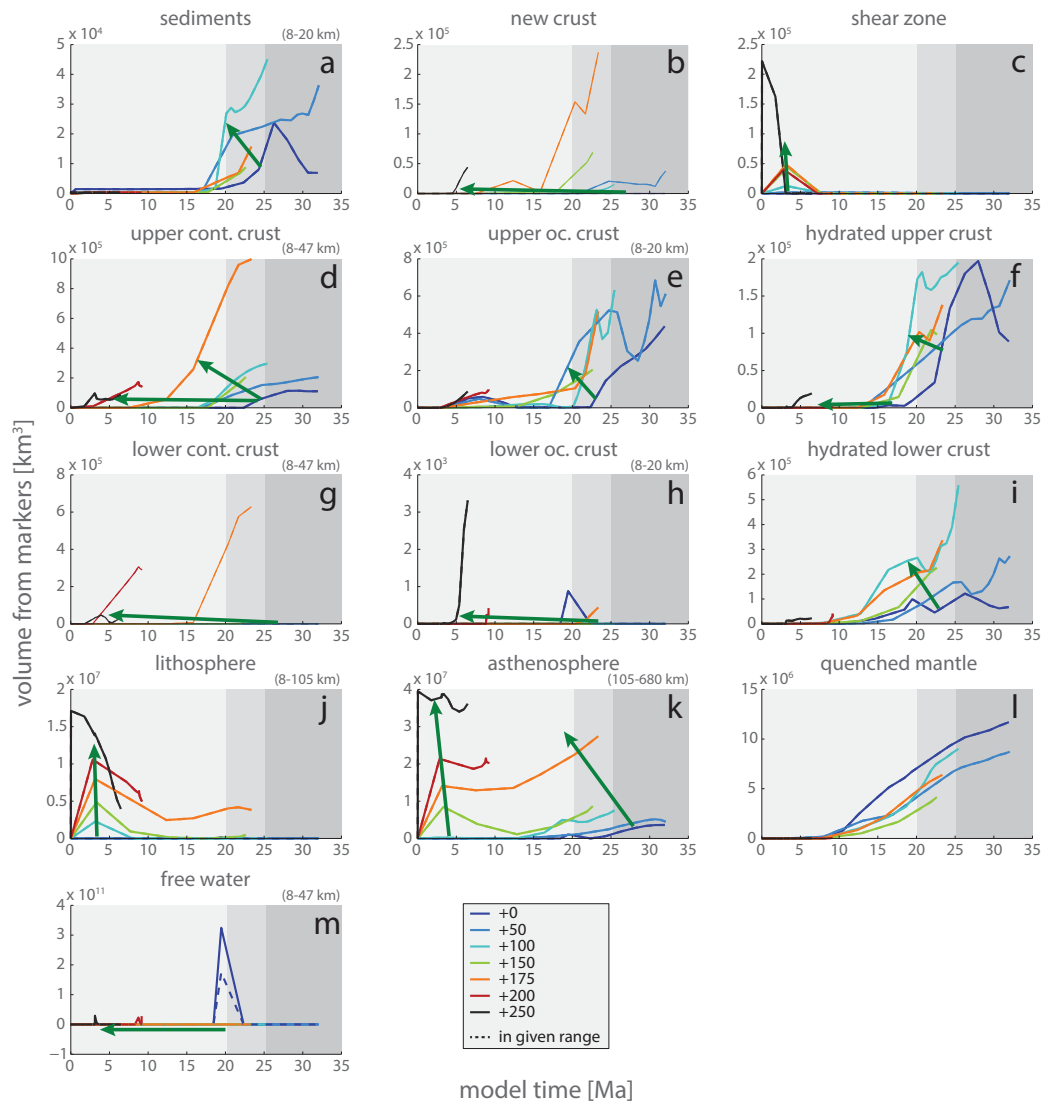


Figure 3.S12: Change in volume over the course of the model is shown separately for each partially molten rock type available (see Fig. 3.2b) for the whole reference model series $A0$ to $A6$ with $\Delta T_p = 0 - 250$ K. In some plots, dashed lines indicate volumes measured only within the given depth range. Additionally the volume of free water markers (Section 2.5) is shown as well. Green arrows indicate the general trend with increasing ΔT_p .

References

- D. Abbott, L. Burgess, J. Longhi, and W. H. F. Smith. An empirical thermal history of the Earth's upper mantle. *Journal of Geophysical Research: Solid Earth*, 99(B7):13835–13850, 1994.
- D. Bittner and H. Schmeling. Numerical Modelling of Melting Processes and Induced Diapirism In the Lower Crust. *Geophysical Journal International*, 123(1):59–70, 1995.
- W. Bleeker, J. W. Ketchum, V. A. Jackson, and M. E. Villeneuve. The Central Slave Basement Complex, Part I: its structural topology and autochthonous cover. *Canadian Journal of Earth Sciences*, 36(7):1083–1109, 1999.
- P. Bouilhol, V. Magni, J. van Hunen, and L. Kaislaniemi. A numerical approach to melting in warm subduction zones. *Earth and Planetary Science Letters*, 411:37–44, 2015.
- R. M. Canup. Origin of Terrestrial Planets and the Earth–Moon System. *Physics Today*, 57(4):56–62, 2004.
- D. Chardon, D. Gapais, and F. Cagnard. Flow of ultra-hot orogens: A view from the Precambrian, clues for the Phanerozoic. *Tectonophysics*, 477(3-4):5–118, 2009.
- C. Clauser and E. Huenges. Thermal Conductivity of Rocks and Minerals. In T. Ahrens, editor, *Rock Physics and Phase Relations*, volume 3, pages 105–126. AGU Reference Shelf, 1995.
- W. Collins, V. Kranendonk, MJ, and C. Teyssier. Partial convective overturn of Archaean crust in the east Pilbara Craton, Western Australia: driving mechanisms and tectonic implications. *Journal of Structural Geology*, 20(9):1405–1424, 1998.
- F. Crameri, H. Schmeling, G. J. Golabek, T. Duretz, R. Orendt, S. J. H. Buiter, D. A. May, B. J. P. Kaus, T. V. Gerya, and P. J. Tackley. A comparison of numerical surface topography calculations in geodynamic modelling: an evaluation of the ‘sticky air’ method. *Geophysical Journal International*, 189(1):38–54, 2012.
- J. A. Crisp. Rates of magma emplacement and volcanic output. *Journal of Volcanology and Geothermal Research*, 20(3–4):177–211, 1984.
- G. F. Davies. On the emergence of plate tectonics. *Geology*, 20(11):963–966, 1992.

- M. J. de Wit. On Archean granites, greenstones, cratons and tectonics: does the evidence demand a verdict? *Precambrian research*, 91(1):181–226, 1998.
- T. Duretz, T. V. Gerya, and W. Spakman. Slab detachment in laterally varying subduction zones: 3-D numerical modeling. *Geophysical Research Letters*, 41(6):1951–1956, 2014.
- R. Fischer and T. Gerya. Early Earth plume tectonics: A high-resolution 3D numerical modelling approach. *Journal of Geodynamics*, in press.
- R. Fischer and T. Gerya. Regimes of subduction and lithospheric dynamics in the Precambrian: 3D thermomechanical modelling. *Gondwana Research*, submitted for publication.
- C. François, P. Philippot, P. Rey, and D. Rubatto. Burial and exhumation during Archean sagduction in the East Pilbara Granite-Greenstone Terrane. *Earth and Planetary Science Letters*, 396(0):235–251, 2014.
- H. Furnes, Y. Dilek, and M. de Wit. Precambrian greenstone sequences represent different ophiolite types. *Gondwana Research*, 2014.
- T. Gerya. Precambrian geodynamics: Concepts and models. *Gondwana Research*, 25(2):442–463, 2014.
- T. V. Gerya and D. A. Yuen. Characteristics-based marker-in-cell method with conservative finite-differences schemes for modeling geological flows with strongly variable transport properties. *Physics of the Earth and Planetary Interiors*, 140(4):293–318, 2003.
- T. V. Gerya and D. A. Yuen. Robust characteristics method for modelling multiphase visco-elasto-plastic thermo-mechanical problems. *Physics of the Earth and Planetary Interiors*, 163(1-4):83–105, 2007.
- T. V. Gerya, R. J. Stern, M. Baes, S. V. Sobolev, and S. A. Whattam. Plate tectonics on the Earth triggered by plume-induced subduction initiation. *Nature*, 527(7577):221–225, 2015.
- R. Govers and M. J. R. Wortel. Lithosphere tearing at STEP faults: response to edges of subduction zones. *Earth and Planetary Science Letters*, 236(1-2):505–523, 2005.
- W. B. Hamilton. Archean magmatism and deformation were not products of plate

- tectonics. *Precambrian Research*, 91(1):143–179, 1998.
- C. Herzberg. Early Earth: Archaean drips. *Nature Geoscience*, 7(1):7–8, 2014.
- C. Herzberg, P. D. Asimow, N. Arndt, Y. Niu, C. M. Lesher, J. G. Fitton, M. J. Cheddle, and A. D. Saunders. Temperatures in ambient mantle and plumes: Constraints from basalts, picrites, and komatiites. *Geochemistry Geophysics Geosystems*, 8(2):n/a–n/a, 2007.
- C. Herzberg, K. Condie, and J. Korenaga. Thermal history of the Earth and its petrological expression. *Earth and Planetary Science Letters*, 292(1–2):79–88, 2010.
- A. Hickman. Two contrasting granite-greenstone terranes in the Pilbara Craton, Australia: evidence for vertical and horizontal tectonic regimes prior to 2900Ma. *Precambrian Research*, 131(3):153–172, 2004.
- R. I. Hill, I. H. Campbell, and R. W. Griffiths. Plume Tectonics and the Development of Stable Continental Crust. *Exploration Geophysics*, 22(1):185–188, 1991.
- C. Jaupart, S. Labrosse, and J. C. Mareschal. 7.06 - Temperatures, Heat and Energy in the Mantle of the Earth. In G. Schubert, editor, *Treatise on Geophysics*, chapter 7, pages 253–303. Elsevier, Amsterdam, 2007.
- T. E. Johnson, M. Brown, B. J. P. Kaus, and J. A. VanTongeren. Delamination and recycling of Archaean crust caused by gravitational instabilities. *Nature Geoscience*, 7(1):47–52, 2014.
- T. Keller and P. J. Tackley. Towards self-consistent modeling of the martian dichotomy: The influence of one-ridge convection on crustal thickness distribution. *Icarus*, 202(2):429–443, 2009.
- A. F. M. Kisters and C. R. Anhaeusser. Emplacement features of Archaean TTG plutons along the southern margin of the Barberton greenstone belt, South Africa. *Precambrian Research*, 75(1–2):1–15, 1995.
- S. Labrosse and C. Jaupart. Thermal evolution of the Earth: Secular changes and fluctuations of plate characteristics. *Earth and Planetary Science Letters*, 260(3–4):465–481, 2007.
- D. McKenzie and M. J. Bickle. The Volume and Composition of Melt Generated by Extension of the Lithosphere. *Journal of Petrology*, 29(3):625–679, 1988.

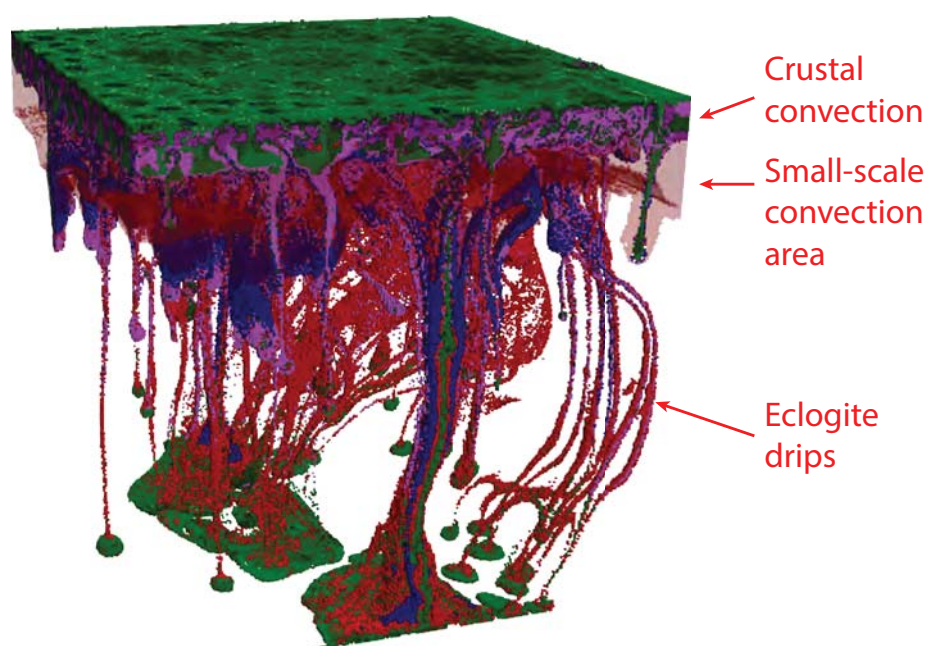
- J.-F. Moyen and J. van Hunen. Short-term episodicity of Archaean plate tectonics. *Geology*, 40(5):451–454, 2012.
- L. L. Perchuk and T. V. Gerya. Formation and evolution of Precambrian granulite terranes: a gravitational redistribution model. *Geological Society of America Memoirs*, 207:289–310, 2011.
- G. Ranalli. *Rheology of the Earth*. Springer, 1995.
- M. W. Schmidt and S. Poli. Experimentally based water budgets for dehydrating slabs and consequences for arc magma generation. *Earth and Planetary Science Letters*, 163(1–4):361–379, 1998.
- E. Sizova, T. Gerya, M. Brown, and L. L. Perchuk. Subduction styles in the Precambrian: Insight from numerical experiments. *Lithos*, 116(3–4):209–229, 2010.
- E. Sizova, T. Gerya, and M. Brown. Contrasting styles of Phanerozoic and Precambrian continental collision. *Gondwana Research*, 25(2):522–545, 2014.
- E. Sizova, T. Gerya, K. Stüwe, and M. Brown. Generation of felsic crust in the Archean: A geodynamic modeling perspective. *Precambrian Research*, 271:198–224, 2015.
- R. H. Smithies, D. C. Champion, and K. F. Cassidy. Formation of Earth’s early Archaean continental crust. *Precambrian Research*, 127(1–3):89–101, 2003.
- D. Turcotte and G. Schubert. *Geodynamics*. Cambridge University Press, 2. edition, 2002.
- J. van Hunen and M. B. Allen. Continental collision and slab break-off: A comparison of 3-D numerical models with observations. *Earth and Planetary Science Letters*, 302(1–2):27–37, 2011.
- J. van Hunen and J.-F. Moyen. Archean Subduction: Fact or Fiction? *Annual Review of Earth and Planetary Sciences*, 40(1):195–219, 2012.
- J. van Hunen and A. P. van den Berg. Plate tectonics on the early Earth: Limitations imposed by strength and buoyancy of subducted lithosphere. *Lithos*, 103(1–2):217–235, 2008.
- M. J. Van Kranendonk. Two types of Archean continental crust: Plume and plate tectonics on early Earth. *American Journal of Science*, 310(10):1187–1209, 2010.

- M. J. Van Kranendonk. Cool greenstone drips and the role of partial convective overturn in Barberton greenstone belt evolution. *Journal of African Earth Sciences*, 60(5):346–352, 2011.
- M. J. Van Kranendonk, W. Collins, A. Hickman, and M. J. Pawley. Critical tests of vertical vs. horizontal tectonic models for the Archaean East Pilbara granite–greenstone terrane, Pilbara craton, western Australia. *Precambrian Research*, 131(3):173–211, 2004.
- N. J. Vlaar, P. E. van Keken, and A. P. van den Berg. Cooling of the earth in the Archaean: Consequences of pressure-release melting in a hotter mantle. *Earth and Planetary Science Letters*, 121(1):1–18, 1994.
- K. Vogt, T. V. Gerya, and A. Castro. Crustal growth at active continental margins: Numerical modeling. *Physics of the Earth and Planetary Interiors*, 192–193(0):1–20, 2012.
- G. J. Wasserburg, J. F. M. Gordon, F. Hoyle, and W. A. Fowler. Relative Contributions of Uranium, Thorium, and Potassium to Heat Production in the Earth. *Science*, 143(3605):465–467, 1964.
- G. Zhu, T. V. Gerya, P. J. Tackley, and E. Kissling. Four-dimensional numerical modeling of crustal growth at active continental margins. *Journal of Geophysical Research: Solid Earth*, 118(9):4682–4698, 2013.

Chapter 4

Early Earth plume-lid tectonics: A high-resolution 3D numerical modelling approach¹

Abstract



Geological-geochemical evidence points towards higher mantle potential temperature and a different type of tectonics (global plume-lid tectonics) in the early Earth (> 3.2 Ga) compared to the present day (global plate tectonics). In order to investigate tectono-magmatic processes associated with plume-lid tectonics and crustal growth under hotter mantle temperature conditions, we conduct a series of 3D high-resolution magmatic-thermomechanical models. No external plate tectonic forces are applied to isolate 3D effects of various plume-lithosphere and crust-mantle interactions. Results

¹This material is accepted for publication in Journal of Geodynamics, 2016

of the numerical experiments show two distinct phases in coupled crust-mantle evolution: (1) a longer (80 – 100 Myr) and relatively quiet ‘growth phase’ which is marked by growth of crust and lithosphere, followed by (2) a short (~ 20 Myr) and catastrophic ‘removal phase’, where unstable parts of the crust and mantle lithosphere are removed by eclogitic dripping and later delamination. This modelling suggests that the early Earth plume-lid tectonic regime followed a pattern of episodic growth and removal, also known as episodic overturn, with a periodicity of ~ 100 Myr.

4.1 Introduction

In the late 18th century the famous Scottish geologist, James Hutton – father of modern geology – introduced the idea of uniformitarianism. He understood that the land we see today was shaped by processes that had acted in a similar fashion in the past and will continue to act in the same manner (Hutton, 1788). In the early 19th century Sir Charles Lyell rephrased this idea into what is still taught to geology students all around the globe, “The present is the key to the past”. The uniformitarian view holds up well when explaining modern geodynamics and the successful paradigm of plate tectonics through the Phanerozoic. But gradual changes appear in the style of tectonics through the Proterozoic and late Archean (Sizova et al., 2010, 2014; O’Neill and Wyman, 2013; Chapter 3), and controversy remains for the early Archean, > 3.2 Ga.

From our present-day understanding of geodynamics, however, we struggle to understand processes older than 3.2 Ga (Champion and Smithies, 2007; Van Kranendonk et al., 2007; Gerya, 2014a, and references therein), such as the formation of cratons or even the dominant tectonic style in the Hadean and early Archean. What is needed is a global working paradigm for Archean geodynamics comparable to plate tectonics (Benn et al., 2006). The directly accessible surface rock record of early Archean age is sparse, and unaltered geophysical data is limited which amplifies the role of quantitative geodynamic modelling approaches for the integration of observational constraints from a wide range of disciplines in order to further our understanding of Archean geodynamics (Champion and Smithies, 2007; Van Kranendonk et al., 2007; Gerya, 2014a, and references therein).

From the perspective of numerical geodynamic modelling, present-day geodynamics – plate tectonics – is predominantly driven by tectonism. Tectonism is a process

of deformation in the Earth's crust that produces its continents and ocean basins, plateaus and mountains, fold of strata, and faults. Thermomechanical models are therefore sufficient in order to understand modern geodynamics. In the early Earth, however, the increased mantle temperature leads to massive heat and mass advection by mantle-derived magmas and widespread melt-induced weakening of the lithosphere (Lenardic et al., 2005; Gerya et al., 2015, and references therein). Archean geodynamics follow an overall tectono-magmatic style and require more sophisticated magmatic-thermomechanical models (Sizova et al., 2015).

Several different models have already been proposed to describe Archean tectonics. For example, it has been suggested that the Archean Earth and its tectonic style was similar to present-day Venus (e.g. Van Kranendonk, 2010; Harris and Bédard, 2014, 2015). These authors argue that the two planets are relatively similar in many ways, however, Venus has preserved not only a higher surface temperature but also a higher internal temperature due to its closer distance to the sun (Breuer and Moore, 2007). Venusian surface tectonics is marked by an absence of a well-defined plate mosaic and by the presence of striking coronae and novae features (Hansen and Willis, 1996; Phillips and Hansen, 1998; Gerya, 2014b, and references therein). The common theory is that these features are formed by mantle plumes and that the planet experiences episodic overturn events rather than the style of plate tectonics that we observe on present-day Earth (Schaber et al., 1992; Strom et al., 1994; Armann and Tackley, 2012). It is speculated that the large displacements of plana observed are driven by mantle flow (Harris and Bédard, 2015).

The hypothesis of plume-induced tectonics, plume-lid tectonics (Gerya et al., 2015), is often invoked for the early Archean. In this case, tectonic deformation of crust and lithosphere is not produced by plate tectonics and its major driving forces, among others the slab pull force (van Hunen and Moyen, 2012), but by mantle plumes and various other active mantle and crustal upwellings and downwellings. The Archean plume-lid tectonics regime has been described by Van Kranendonk (2011b), who suggested an early Earth geodynamic style (before 3 Ga) with small mobile plates and rapid upper mantle convection. Continental crust is formed by volcanism over upwelling mantle or by imbrication over downwelling mantle (Van Kranendonk, 2011b). Johnson et al. (2014) and Sizova et al. (2015) modelled early Earth plume-lid tectonics in 2D, where they showed that continued melting and dripping of over-thickened crust under Archean conditions in combination with fractionation could lead to the source

magmas required for TTG melts. Van Thienen et al. (2005a) discussed 2D models of the whole mantle under Archean conditions, concluding that the Archean mantle shows strong heterogeneity and different reservoirs produced by convective instabilities and resurfacing events.

Crustal and mantle processes associated with plume-lithosphere interactions are intrinsically three-dimensional and require 3D numerical modelling approaches (Burov and Gerya, 2014). Therefore, a systematic 3D high-resolution magmatic-thermomechanical numerical modelling effort is required to understand how plume-lid tectonics operated in the early Earth. In the preceding Chapter 3 we investigated a gradual change between the two global tectonic regime end-members, present-day plate tectonics and Archean plume-lid tectonics with increasing mantle potential temperature using kinematically driven 3D models with typical present-day oceanic-continental plate boundary settings. In contrast, this new study will focus on the plume-lid tectonics regime itself, based on more appropriate 3D magmatic-thermomechanical models with laterally homogeneous unstressed lithosphere (Johnson et al., 2014; Sizova et al., 2015).

4.2 Methods

4.2.1 Model design

In order to investigate tectono-magmatic processes associated with plume-lid tectonics and crustal growth under hot Archean mantle temperature conditions, we examine a series of 3D high-resolution magmatic-thermomechanical models. In contrast to Chapter 3, no external plate tectonic forces were applied in these models in order to isolate 3D effects of plume-lithosphere and crust-mantle interactions (Johnson et al., 2014; Sizova et al., 2015; Fischer and Gerya, submitted for publication).

To model Archean upper mantle and crustal processes, a model setup of 520 km in length, width and depth has been chosen. The initial laterally homogeneous plate setup (Fig. 4.1a) is simplified to prevent inscription of any predefined structures and consists of a 35 km thick crust of varying composition (Table 4.2) on top of the asthenospheric mantle.

We use the 3D numerical magmatic-thermomechanical I3ELVIS code (Gerya and Yuen,

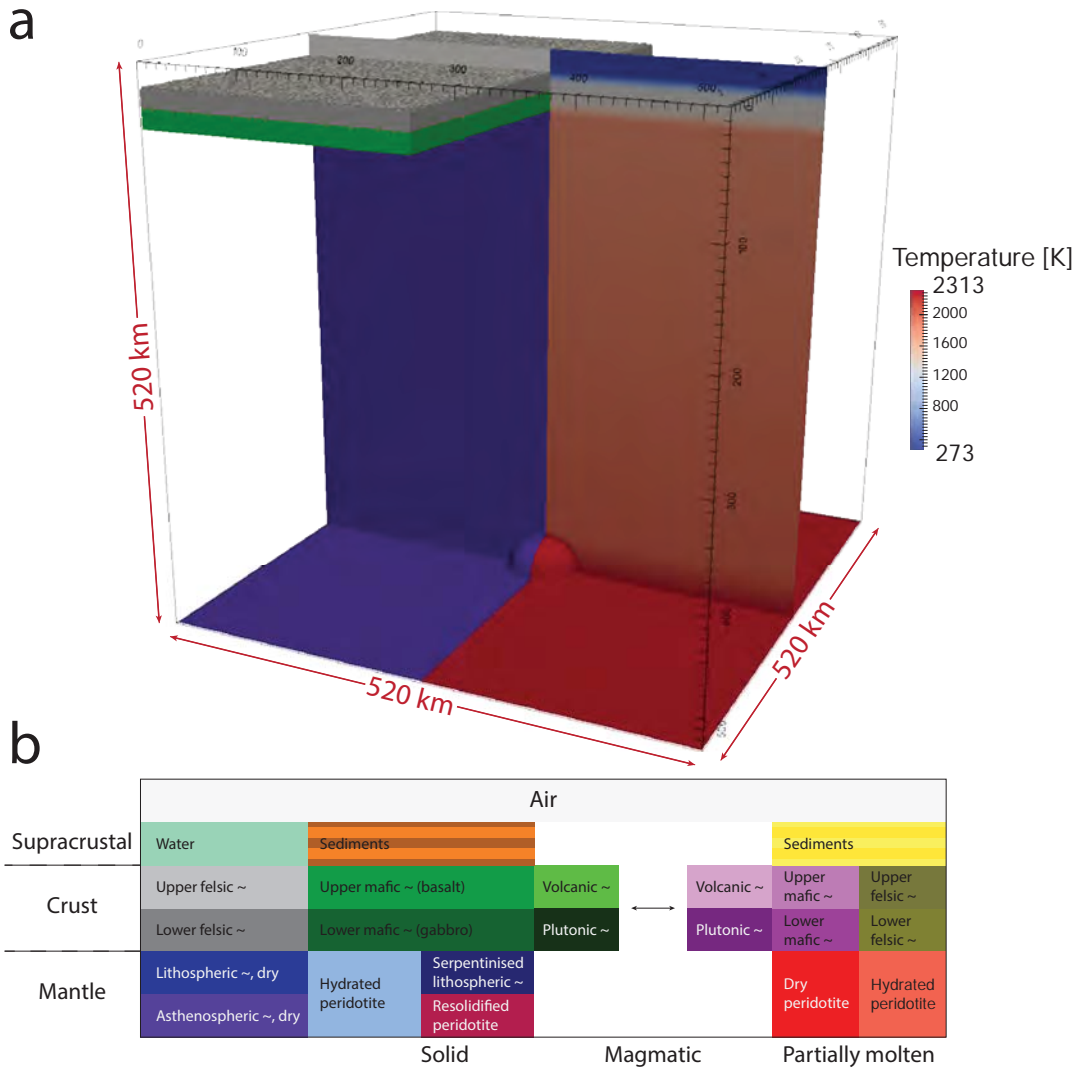


Figure 4.1: (a) The initial model setup shown in 3D as well as a 2D cross-section. The left side shows the initial compositional setup whereas the right side shows the initial temperature structure. (b) All available material types and their colour code in both solid and partially molten state as will be used throughout this paper.

2007) which is based on a conservative finite difference method with a multigrid solver and a non-diffusive marker-in-cell technique to simulate multiphase flow (Gerya and Yuen, 2003, 2007). Additionally, the 3D code features melting of crustal and mantle rocks, and volcanic and plutonic addition of juvenile crust from extracted mantle-derived melt, eclogitic phase changes as well as hydration and dehydration processes (Zhu et al., 2013; Gerya et al., 2015).

The crust chosen can be either one- or two-layered, following Van Kranendonk et al. (2014b) for a ‘Stage 1: developing protocrust’. In the two-layered case, both layers are initially chosen to be 17.5 km thick. Various crustal compositions are explored, one- and two-layered felsic crust and one- and two-layered mafic crust as well as felsic rocks underlain by mafic crust (Table 4.2; Rudnick and Gao, 2003).

All velocity boundary conditions are free slip. The uppermost 20 km of the model domain is filled with ‘sticky air’ which acts as an internal free surface boundary condition (Cramer et al., 2012). In order to ensure mantle plume growth from the bottom of the model (Johnson et al., 2014; Sizova et al., 2015), an elevated mantle temperature of 2313 K is prescribed at the lower boundary which is 240 K higher than the potential mantle temperature at this depth.

The initial temperature structure of the model is adjusted to the Archean Earth (Chapter 3; Sizova et al., 2010, 2015; Brown, 2007). According to Herzberg et al. (2010) an elevated mantle potential temperature of $T_p = 1823$ K can occur at any age > 1.5 Ga. However, comparison of modelling results with geological observations (e.g. Collins et al., 1998; Van Kranendonk, 2011a) shows that the appropriate time range is closer to early Archean. The crust has a hot initial geotherm with a fixed temperature of 273 K at the top. The uppermost 10 km have a temperature gradient of 100 K/km, the next 20 km have a lower temperature gradient of 5 K/km. The following layer of 10 km thickness and a temperature gradient of 47 K/km acts as a transition between crust and asthenospheric mantle. This setup assumes a separate crustal convection cell and a transition zone between the crustal and mantle reservoir.

In the initial model no lithosphere is defined either thermally or compositionally. However, lithosphere is able to develop spontaneously through the course of the model. The asthenospheric mantle has a linear adiabatic temperature gradient of 0.5 K/km and the mantle potential temperature T_p is increased by $\Delta T_p = 267$ K compared to present-day reference mantle potential temperature $T_p = T_{initial} = 1556$ K. A pre-existing self-consistent mantle depletion profile is defined that corresponds to dry melting along the prescribed mantle potential temperature profile with an adiabatic thermal gradient of 0.5 K/km. The lowermost 40 km at the model bottom have a steep temperature gradient to meet the increased thermal boundary condition of 2313 K. As an initial thermal perturbation in the mantle, a half-sphere of 40 km radius is inscribed with a temperature of 2313 K at the centre of the lower boundary (Fig. 4.1a).

Eruption efficiency of volcanic compared to plutonic eruption can be freely varied via the parameter χ_{volc} . Eruption efficiency on present-day Earth is estimated to be around 5 – 20% (Crisp, 1984). However, it is not clear whether this also holds true for Archean tectonic settings. In the heat-pipe mode suggested by Moore and Webb (2013) it is assumed to be 100%. We therefore vary χ_{volc} between 0% and 100% (see Table 4.2). Thresholds for melt extraction are set to $M_{min} = 2 \text{ wt\%}$ and $M_{max} = 4 \text{ wt\%}$. For selected models, melt-induced weakening and fracture healing is activated (see Table 4.2). Erosion and sedimentation level are set to $y_{eroslev} = 10 \text{ km}$ respectively $y_{sedilev} = 25 \text{ km}$, while the sea level is fixed at $y_{waterlev} = 20 \text{ km}$. We use 10^{18} Pa s and 10^{24} Pa s respective, as lower and upper cut-off viscosity limits for all types of materials.

14 different rock types (not including ‘sticky air’ and ‘sticky water’) are available in both solid and partially molten state (see Fig. 4.1b). Four different visco-plastic flow laws are applied to these rock types. A wet quartzite flow law (Ranalli, 1995) is applied to sediments and upper crustal material. The lower crust follows a plagioclase An₇₅ flow law and dry or wet mantle follow a respective (i.e., dry or wet) olivine flow law (Ranalli, 1995). See Table 4.1 for a full compilation of material properties (and Table 4.S1 for models *B100b*, *D0b*, *D100b* and *E100b*).

For a more detailed discussion of the applied methods see Chapter 2 and Fischer and Gerya (in press).

4.2.2 Reference model series

According to Sizova et al. (2010); Fischer and Gerya (submitted for publication) the increase in mantle potential temperature ΔT_p is the major parameter which influences transition from plume tectonics to plate tectonics. At high $\Delta T_p = 250 \text{ K}$ no elements of plate tectonics are visible. To explore the plume tectonic end-member we therefore assume an increase in mantle potential temperature of $\Delta T_p = 267 \text{ K}$ while assuming a present-day mantle potential temperature of $T_p = 1556 \text{ K}$.

To explore plume tectonics models we vary the eruption efficiency of volcanic vs. plutonic magmatism (χ_{volc}) as well as the initial composition of the upper and lower crust. The influence of rheological weakening and healing has also been studied. All models

Table 4.1: Material properties ^a as well as applied rheology and melting model are listed for each of the used lithologies as given in Fig. 4.1b.

Material	Rheology [MPa ⁻ⁿ s ⁻¹], [-], [kJ], [$\frac{1}{\text{bar}}$] [$\frac{1}{\text{kg}}$]	ρ_0 [$\frac{\text{kg}}{\text{m}^3}$]	k [K]	Melting [$\frac{\text{W}}{\text{m}^2\text{K}}$]	H_r^b [$\frac{\mu\text{W}}{\text{m}^3}$]	H_L [kJ]	ϕ_0, ϕ_1 [-]	γ_0, γ_1 [-]	σ_{crit} [MPa]	C_p [$\frac{\text{kJ}}{\text{kg}}$]
Sediments	Wet quartzite flow law $B_D = 1.97 \cdot 10^{17}$, $n = 2.3$, $E_a = 154$, $V_a = 0$	2600 solid 2400 molten	$0.64 + \frac{807}{T+77}$	Granite	2.0 2.0	- 300	0.0, 0.0 -	0.0, 0.5 -	0.03 -	1.0 1.5
Upper felsic crust	-	2750 solid	-	-	1.0	-	0.200, 0.0	0.0, 0.5	0.03	1.0
Hydrated felsic crust	-	2400 molten	-	-	2.0	300	-	-	-	1.5
Upper mafic crust	-	2400 molten	-	Basalt	1.0	300	0.200, 0.0	0.0, 0.5	0.03	1.0
Volcanic crust	-	3000 solid	$1.18 + \frac{474}{T+77}$	-	0.25	-	0.0, 0.0	0.0, 0.5	0.03	1.0
		2900 molten	$0.64 + \frac{807}{T+77}$	-	0.25	380	-	-	-	1.5
		3000 solid	$1.18 + \frac{474}{T+77}$	-	0.25	-	0.0, 0.0	0.0, 0.5	0.03	1.0
		2900 molten	-	-	0.25	380	-	-	-	1.5
Lower felsic crust	Plagioclase Arr ^s flow law $B_D = 4.80 \cdot 10^{22}$, $n = 3.2$, $E_a = 238$, $V_a = 0$	2950 solid 2400 molten	$1.18 + \frac{474}{T+77}$	Gabbro	0.5 2.0	- 380	0.200, 0.0	0.0, 0.5	0.03 -	1.0 1.5
Lower mafic crust	-	3000 solid	$1.18 + \frac{474}{T+77}$	-	0.25	-	0.200, 0.0	0.0, 0.5	0.03	1.0
Plutonic crust	-	2900 molten	-	Basalt	0.25	380	-	-	-	1.5
		3000 solid	-	-	0.25	-	0.200, 0.0	0.0, 0.5	0.03	1.0
		2900 molten	-	-	0.25	380	-	-	-	1.5
Hydrated crust	-	2900 solid	-	-	0.5	-	0.200, 0.0	0.0, 0.5	30	1.0
		2400 molten	$0.64 + \frac{807}{T+77}$	-	1.0	380	-	-	-	1.5
Asthenospheric mantle	Dry olivine flow law $B_D = 3.98 \cdot 10^{16}$, $n = 3.5$, $E_a = 532$, $V_a = 0.8$	3300 solid 2900 molten	$0.73 + \frac{1293}{T+77}$	Peridotite	0.022 0.023	- 400	0.200, 0.0	0.0, 0.5	0.03 -	1.0 1.5
Depleted mantle	-	3300 solid	-	-	0.020	-	0.200, 0.0	0.0, 0.5	0.03	1.0
Quenched mantle	-	2900 molten	-	-	0.021	400	-	-	-	1.5
		3300 solid	-	-	0.024	-	0.200, 0.0	0.0, 0.5	0.03	1.0
		2900 molten	-	-	0.025	400	-	-	-	1.5
Hydrated mantle	Wet olivine flow law $B_D = 5.01 \cdot 10^{20}$, $n = 4.0$, $E_a = 470$, $V_a = 0.8$	3300 solid 2900 molten	$0.73 + \frac{1293}{T+77}$	Peridotite	0.024 0.025	- 400	0.200, 0.0	0.0, 0.5	30 -	1.0 1.5
Serpentinite	-	3300 solid	-	-	0.024	-	0.200, 0.0	0.0, 0.5	30	1.0
References ^c		4,1	1,2	3	5-10	1	1,2			

^a for all rock types: Cohesion $C_0 = C_1 = 1 \text{ MPa}$. Thermal expansion coefficient $\alpha = 3.0 \cdot 10^{-5} \text{ K}^{-1}$ and compressibility $\beta = 1.0 \cdot 10^{-5} \text{ GPa}^{-1}$.

^b fixed at present-day values as the influence of radiogenic heating is negligible compared to increased mantle temperature (Sizova et al., 2010).

^c (1) Turcotte and Schubert (2002), (2) Bittner and Schmelting (1995), (3) Clauser and Hengges (1995), (4) Ranalli (1995), (5) Schmidt and Poli (1998), (6) Johannes (1985), (7) Poli and Schmidt (2002), (8) Schmidt and Poli (1998), (9) Hess (1989), (10) Katz et al. (2003)

(Table 4.2) have the same setup as discussed in Section 2.3: no lithosphere initially and a crustal thickness of 35 km.

Model	χ_{volc} [%]	$\dot{\epsilon}_{healing}$ [s^{-1}]	λ_{melt}	Upper crust	Lower crust
A20	20%	10^{-14}	0.01	felsic wet	felsic dry
B20	20%	10^{-14}	0.01	felsic wet	mafic dry
B100b	100%	0	1.0	felsic wet	mafic dry
C20	20%	10^{-14}	0.01	mafic wet	mafic dry
D0	0%	10^{-14}	0.01		mafic dry
D0b	0%	$2.5 \cdot 10^{-14}$	0.0		mafic dry
D20	20%	10^{-14}	0.01		mafic dry
D100	100%	10^{-14}	0.01		mafic dry
D100b	100%	0	1.0		mafic dry
E100b	100%	0	1.0		felsic wet

Table 4.2: List of all reference models. All models are designed using the setup described in Section 2.3 and Fig. 4.1a.

4.3 Results

4.3.1 Reference model *D100b*

The reference model *D100b* has a pure mafic crust. Eruption efficiency is 100% and no melt-induced weakening is considered ($\lambda_{melt} = 1$, $\dot{\epsilon}_{healing} = 0 s^{-1}$). From the very beginning of the model, new crust is formed continuously in a heat-pipe-mode fashion (Moore and Webb, 2013), originating from the thick layer of partially molten mantle (~ 200 km) directly underplating the partially molten lower crust. After ~ 3 Myr the plume arrives and penetrates the partially molten mantle layer and the crust on top of the plume starts to thicken due to the rapid melt addition from the plume, thus creating a circular volcanic (‘greenstone’) area at the surface (Fig. 4.2a). The ‘plug’ of newly formed volcanic crust increases in diameter and thickness and a ring of sediments forms around it. With continuing volcanism, the sediments are buried between the plug and underlying crust and the original mafic crust subsides into the mantle (Fig. 4.2b). At 8 Myr, eclogitisation depth of the mafic crust is reached. The unstable material drips down into the mantle as a cold high-density eclogitic drip (Fig. 4.2b). The downward motion of the cold crustal material into the mantle stops the upward motion of the plume, deflecting it outwards and producing new secondary plumes further away from the centre of the model. The eclogitised volcanic sequence rocks pool at the base of

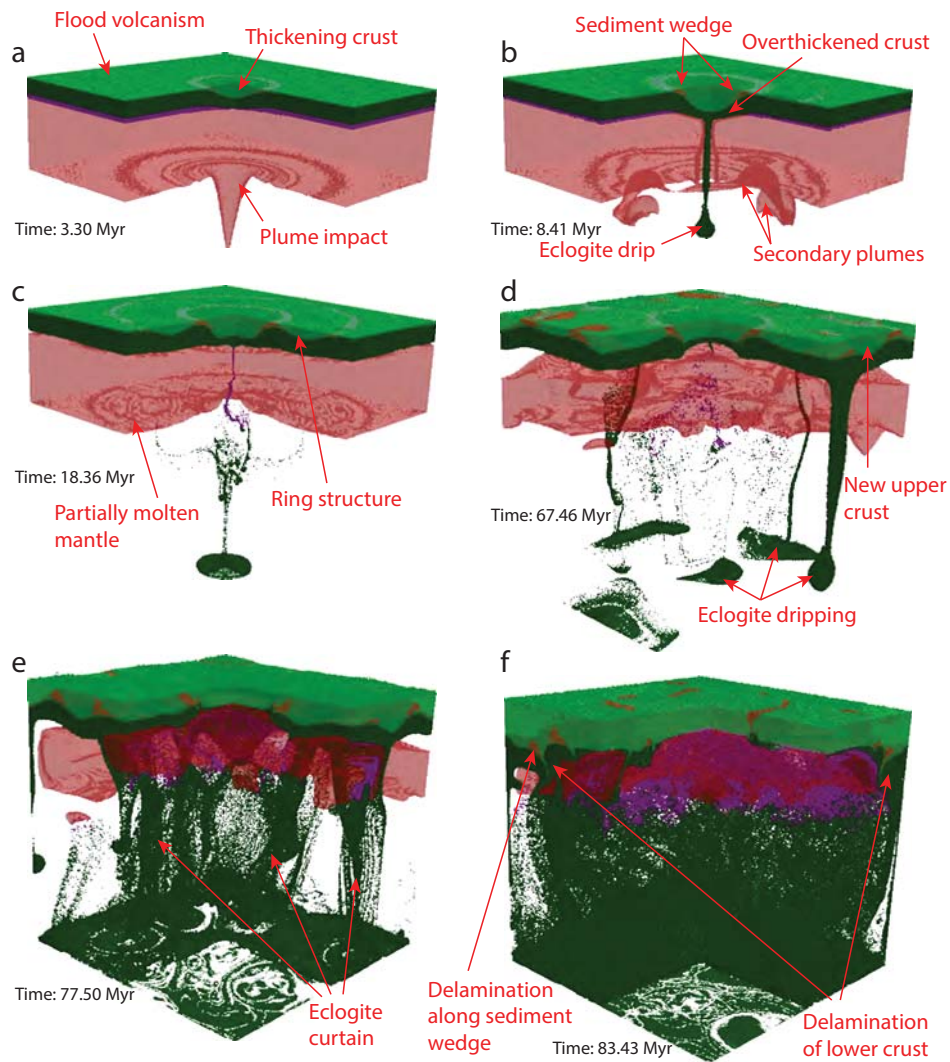


Figure 4.2: Evolution of the reference model *D100b* with a pure mafic crust, eruption efficiency 100% and no melt-induced weakening ($\lambda_{melt} = 1$, $\dot{\epsilon}_{healing} = 0 \text{ s}^{-1}$). The model shows one full cycle of crustal growth and destruction, within ~ 100 Myr. (a) New crust starts to form immediately, forming a thicker plug on top of the central plume. (b-c) The crust reaches eclogitisation depth and becomes thermochemically unstable. A cold eclogitic drip forms which reaches the model bottom. Secondary plumes form a ring structure in the crust. (d) Further crustal thickening leads to formation of a new upper crust and eclogite drips. (e-f) Strong dripping starts delamination of large parts of crust in a retreating sheet-like manner, thereby forming an eclogite curtain. Scales are given in Fig. 4.1a.

the model and leave narrow cylindrical partially molten traces in the partially molten upper mantle region, which become entrained in mantle convection (Fig. 4.2c).

After ~ 65 Myr of constant depletion and cooling of the uppermost mantle, the layer of partial melt has diminished to a thickness of 50–100 km and formed a depleted mantle lithosphere of a thickness of 20–40 km, with an uneven topography of the Moho and LAB. The crust is two-layered with a total thickness of 40–60 km Champion and Smithies (2007); Van Kranendonk et al. (2007, 2014b). A lower layer is formed by the original mafic crust and the upper layer is comprised of the newly formed volcanic (‘greenstone’) sequences with bands of sediments (Fig. 4.2d). Eclogitised crustal drips form in several places where the crust reaches eclogitisation depth. Further model development leads to a thickening of the upper crust by continued flood volcanism and thinning of the lower crust by dripping. At this stage, crustal thinning by eclogitic drip removal occurs in phases with quiet periods in-between. During major dripping phases, drips can also initiate sheet-like delamination of the lower crust from the upper crust (often along zones weakened by sediments).

At 77 Myr a continuous layer of the lower crust starts to delaminate in a wide curved area, filling the whole model domain (Fig. 4.2e). This large-scale delamination continues over the next 6 Myr until large parts of the lower crust are removed by delamination (Fig. 4.2f) leaving only the upper crust, consisting of newly formed volcanic rocks. The remaining crust now has a similar thickness as the original mafic crust (cf Figs. 4.2a and 4.2f).

4.3.2 Influence of eruption efficiency χ_{volc}

We test two different cases, one with only volcanic (model *D100b*) magmatism and one with only plutonic (model *D0b*) magmatism, to understand the influence of these two types of magmatism. A third case with present-day Earth eruption efficiency $\chi_{volc} = 20\%$ (model *D20*) is chosen for comparison. For all three cases, the same initial crustal composition is chosen with a single-layered dry mafic crust.

As already described for the reference model *D100b*, pure volcanic rocks ($\chi_{volc} = 100\%$) lead to a strong growth of crust thickness (5–15 km) as well as a two-layered crust. Both developments lead first to thinning of the lower crust by dripping and later by delamination of the lower crust in a catastrophic event which is aided by the bands of buried sediments located in the bottom of the upper volcanic crust.

Model *D0b* has an eruption efficiency $\chi_{volc} = 0$ and no melt-induced weakening

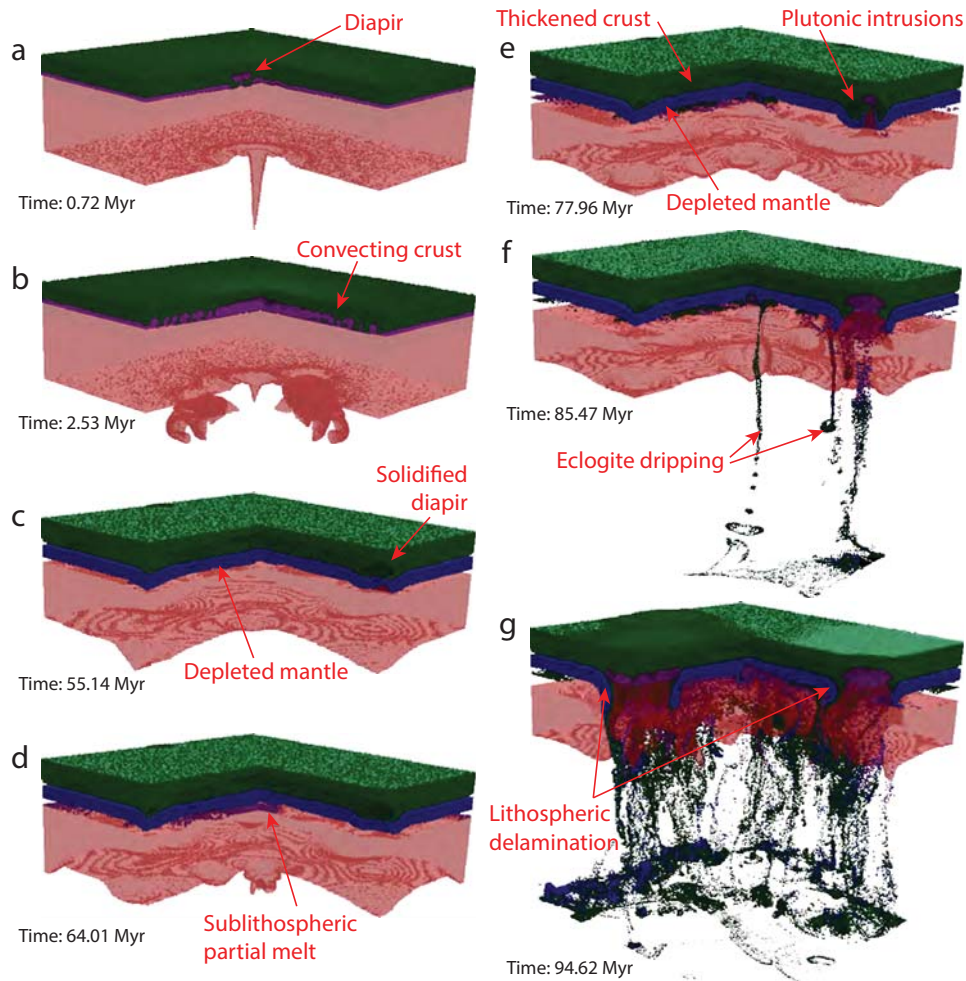


Figure 4.3: Evolution of the model *D0b* with a pure mafic crust, eruption efficiency 0% (with initial emplacement of plutonic rocks at the LAB and their spontaneous propagation to the Moho) and no melt-induced weakening ($\lambda_{melt} = 1.0, \dot{\epsilon}_{healing} = 2.5 \cdot 10^{-14} s^{-1}$). One full cycle of crustal growth and destruction is shown within ~ 100 Myr. (a-b) Accumulated partial melt at the bottom of the crust starts to rise as diapirs. (c) The rising diapirs solidify at mid-crustal level resulting in a thickened crust and mantle lithosphere. (d) Partial melt accumulates at the bottom of the lithosphere. (e) Newly accumulated partial melt starts to solidify and form eclogite or rises through the lithosphere. (f) Where crust has reached eclogitisation depth, it starts to drip into the mantle. (g) Crustal diapirism and eclogite dripping causes delamination of the lithosphere and lower crust. Scales are given in Fig. 4.1a.

($\lambda_{melt} = 1.0, \dot{\epsilon}_{healing} = 10^{-14} s^{-1}$). This allows us to study the case of purely plutonic magmatism. After the plume ascends through the partially molten mantle layer, a thin layer of partially molten newly formed crust builds at the bottom of the crust. This plutonic magma is positively buoyant and starts to rise through the gabbroic crust forming a diapir, which rises to a mid-crustal level of ~ 15 km depth (~ 0.5 Myr,

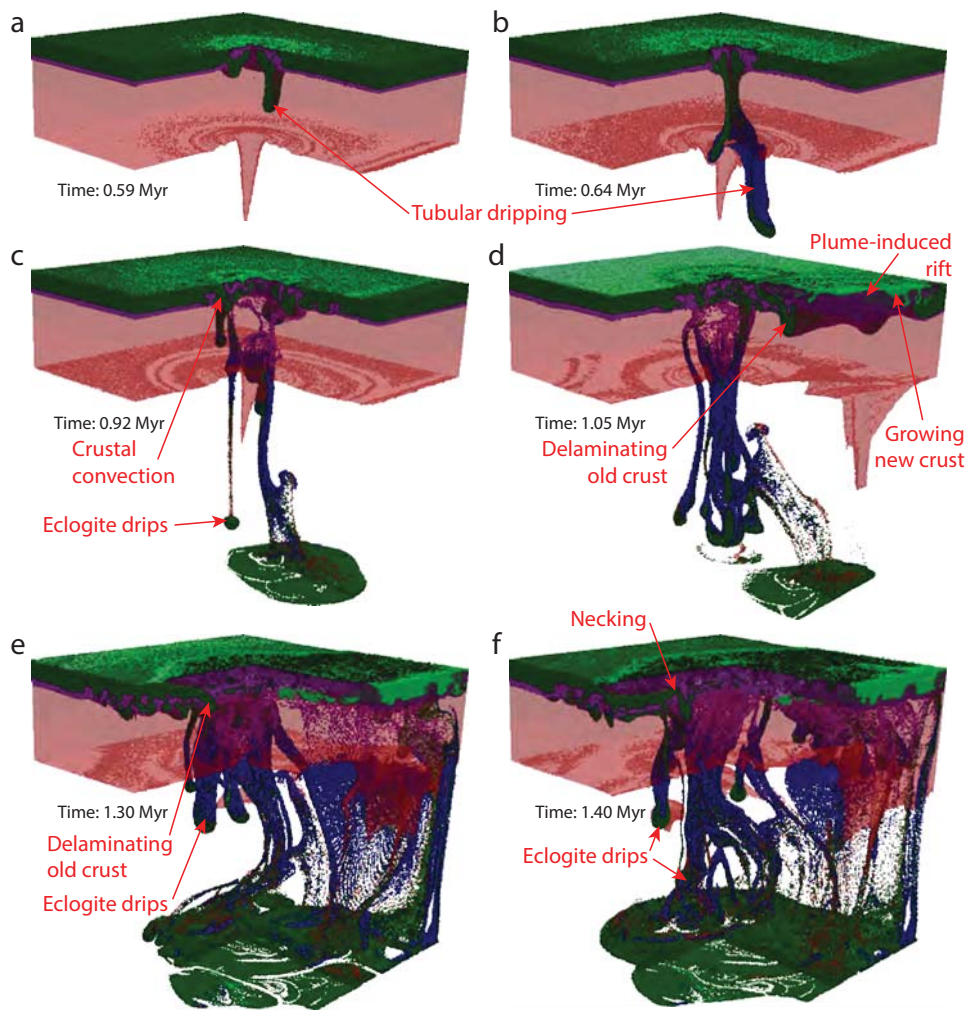


Figure 4.4: Evolution of the model *D20* with a pure mafic crust, eruption efficiency 20% and melt-induced weakening ($\lambda_{melt} = 0.01, \dot{\epsilon}_{healing} = 10^{-14} s^{-1}$). Destabilisation of the crust and the onset of an overturn event is shown. (a-b) The hot mafic melt extracted from the central plume fully penetrates the crust and starts a tubular eclogite drip. (c) Below a thin brittle lid, the crust is convecting vigorously. (d) A mantle plume initiates subduction/delamination of the old crust below the newly formed lid. (e) A circular retreating subduction/delamination of the old crust forms, assisted by eclogite drips. The slab breaks/drips off while the lower part of the crust is still convecting. Scales are given in Fig. 4.1a.

see Fig. 4.3a). Within the next 5 Myr the whole lower crust is penetrated by diapirs starting from the centre of the model radially outwards (Fig. 4.3b). At 6 Myr a period of quiescence starts. The partially molten depleted subcrustal mantle slowly solidifies from top to bottom within the next 20 Myr, resulting in a crust of 40 km thickness underplated by a thin mantle lithosphere of 10 km.

This cycle is now repeated twice during model runtime. Between 35 and 60 Myr a second active phase can be observed with diapirs appearing and then solidifying at mid-crustal level followed by a period of quiescence. However, this activity is less strong than during the first phase. Additionally, the lithosphere is thickening from solidification of the underplating depleted partially molten mantle to a final thickness of 40 km of crust and 20 km of mantle lithosphere (Fig. 4.3c).

At 60 Myr a third phase of activity starts. In some regions with cold and strong lithosphere, the ascending partial melt is deposited at the bottom of the lithosphere which poses a rheological barrier for the melt propagation. The magma therefore collects at the LAB and solidifies (Figs. 4.3d and 4.3e). In some regions with warm and weak lithosphere, the previously solidified lower crustal plutons can remelt and trigger crustal diapirism (Figs. 4.3e and 4.3f). These processes lead to destabilisation of the newly formed crust by eclogitisation-induced dripping (Figs. 4.3e and 4.3f).

In the case where magma collects at the LAB and then solidifies, the newly formed basaltic rock is transformed to high-density eclogite. It will then drip off into the mantle and remove part of the lithosphere as well. This process allows partial melt to ascend into the weakened lithosphere as diapirs that penetrate the lithosphere and ascend into the crust (Figs. 4.3f and 4.3g). When diapirs are able to break through the weakened lithosphere, further thickening of the crust leads to eclogitisation and dripping of the overthickened crust. The dripping initiates sheet-like delamination of the lithosphere which happens in a widening ring around the diapir centre. Together with the lithosphere, the eclogitised bottom of the crust is also delaminated (Fig. 4.3g).

Model *D20* has a $\chi_{volc} = 20\%$ and both plutonic and volcanic magmatism is activated (Table 4.2 and Fig. 4.4). Ascending melt is transported to the surface with 20% efficiency and accumulated at the Moho with 80% efficiency. As in the previous model *D0b* (Fig. 4.3) plutonic processes are more intense in the beginning. Also, because the eruption efficiency is only 20% it takes longer for volcanic crust to grow thick enough to show the typical volcanic processes and features described for the reference model *D100b* (cf. Figs. 4.2 and 4.4). The first 0.5 Myr are therefore characterised by pure plutonic ascent of diapirs in the crust (Fig. 4.4a).

Due to the activated melt-induced rheological weakening of the crust, the diapiric overturn of the crust in model *D20* occurs faster than in the two end-member cases of either pure plutonic or pure volcanic magmatism (cf. Figs. 4.2 to 4.4). In addition,

the rise of the plutonic diapirs is aided by thickening and sinking of newly formed volcanic rocks from the top. Continued diapiric uprising of the plutonic magma as well as sinking of the newly formed volcanic rocks into the crust triggers onset of crustal convection patterns concentrically broadening from the central region of the initial plume upwelling (Fig. 4.4c). Sinking crust then forms tubular eclogitised drips which sink into the mantle. These drips start new secondary mantle plumes which further enhance crustal convection. After 1.0 Myr a plume (close to the model boundary) is able to penetrate the crust and initiates a (semi-)circular delamination/subduction (Fig. 4.4d). Crustal convection still continues below the delaminating old crust which is assisted by eclogite drips and pushed downwards and forced to retreat by the spreading plume (Fig. 4.4e). After 1.4 Myr only a thin (few km) brittle upper crustal lid remains above the regions of the spreading plume and the sinking slab necks off and sinks into the mantle as separate eclogite drips (Fig. 4.4f).

4.3.3 Influence of felsic crust

The presence of lower-density felsic continental crust yields new tectonics and dynamics. Eruptions of basaltic magma onto felsic crust destabilise crustal layers and lead to a faster crustal overturn process. The denser newly formed mantle-derived mafic volcanic rocks sink while the positively buoyant felsic crust starts to rise. This scenario is observed in model *E100b* (eruption efficiency $\chi_{volc} = 100\%$, no melt-induced weakening $\lambda_{melt} = 1.0$ and $\dot{\epsilon}_{healing} = 0 \text{ s}^{-1}$, see Fig. 4.5) which has purely felsic initial crust. In the first 3 Myr the crust on top of the plume is thickened, forming a growing plug, similar to the reference model *D100b* (compare Figs. 4.2a and 4.5a). However, newly formed volcanic crust has a mafic composition and higher density than the initial crust. The thickening plug of newly formed volcanic crust therefore sinks into the initial felsic crust and after 6 Myr starts to underplate the felsic crust (Fig. 4.5b). Within the next 100 Myr mantle plumes in several locations form thickening plugs of newly formed mafic crust which then sink into the underlying felsic crust and underplate it (Figs. 4.5c to 4.5e). After 100 Myr the surface shows large domes of upwelling felsic crust, interrupted by belts of the downwelling newly formed mafic crust which is interspersed with sediments (Fig. 4.5f). A new lower crustal layer of mafic composition forms from the downwelling volcanic rocks. Both upper and lower crust are heterogeneous and have highly irregular boundaries. Due to the strong magmatism, the uppermost mantle becomes depleted forming a growing mantle lithosphere (Fig. 4.5f). The long-term

crustal tectonics continue with dominantly vertical movements. There can, however, be specific situations where whole crustal blocks start to rotate and vertical movement is translated to horizontal crustal deformation.

Model *B100b* (Fig. 4.6) makes use of this final stable crustal layering found in model *D100b* (a lower crust of mafic composition and upper crust of felsic composition, Fig. 4.5f), setting it as the initial condition. All other parameters are the same as for model *E100b* ($\chi_{volc} = 100\%$, $\lambda_{melt} = 1.0$, $\dot{\epsilon}_{healing} = 0 \text{ s}^{-1}$). Again thickening newly formed basaltic volcanic crust sinks into the felsic upper crust, reaching the gabbroic lower crust. There the newly formed volcanic crust is neutrally buoyant and sinks no further (Figs. 4.7i and 4.7j). Instead it spreads along the weak upper-lower crust interface forming a new basaltic middle crust (Figs. 4.6a to 4.6c). After 60 Myr of thickening, the crust grows to a thickness of 40 – 50 km residing on the lithosphere of 20 – 60 km (Fig. 4.6c). Both layers have a strongly varying topography interface depending on the state of the underlying upper-mantle convection. At this point the lower crust reaches the depth of the eclogite transition. Eclogitisation of the lower crust leads to its destabilisation and triggers cylindrical, cold eclogitic drips sinking into the mantle (Figs. 4.6d, 4.7f and 4.7j). Positively buoyant material of the upper crust, such as sediments or felsic crust, is entrained by the dripping. The downgoing tube has a core of felsic material and sediments with a mantle of eclogite enclosed by depleted lithospheric mantle (Fig. 4.6d). After the long period (~ 70 Myr) of quiescence and crustal and lithospheric growth, the cold downwelling thermal-chemical inhomogeneities lead to more vigorous mantle convection and therefore more hot upwellings and more sub-crustal and sublithospheric partial melting (Figs. 4.6e and 4.7g), which in turn leads to further dripping. These drips can also combine to form a sheet-like downwelling which develops into a delamination of the lithosphere and lower crust (Figs. 4.6f, 4.7c, 4.7g and 4.7k). Additionally, the lithospheric/crustal lower surface is eroded by the highly vigorous mantle convection which entrains lithospheric and crustal material (Fig. 4.6f). 30 Myr after the beginning of the vigorous phase (100 Myr), crustal and lithospheric thickness are reduced to almost their initial values with an upper felsic crust of 20 km and a lower mafic crust of 30 km, resulting in a total crustal thickness of 50 km. At this stage, the whole mantle lithosphere is removed and the lower crust is completely replaced by the newly formed and sunken mafic volcanic rocks (Figs. 4.6g, 4.7d, 4.7h and 4.7l).

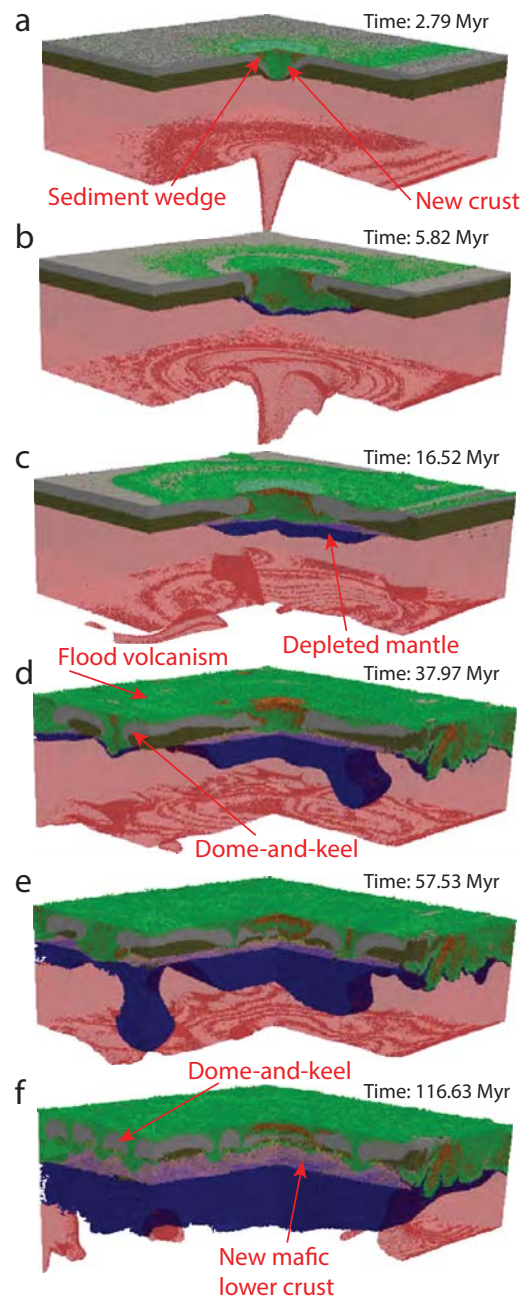


Figure 4.5: Evolution of the model *E100b* with a pure felsic crust, eruption efficiency $\chi_{volc} = 100\%$ and no melt-induced weakening ($\lambda_{melt} = 1.0$, $\dot{\epsilon}_{heating} = 0 \text{ s}^{-1}$). (a-b) Newly formed mafic crust sinks through the initial felsic crust and starts to underplate it. (c) Continuous volcanism leads to the formation of a thin lithosphere. (d-e) Doming of the initial felsic crust and sinking of the newly formed volcanic crust leads to the typical Archean dome-and-keel pattern. (f) After crustal overturn the crust consists now of a predominantly felsic upper and predominantly mafic lower layer residing on the thick mantle lithosphere. Scales are given in Fig. 4.1a.

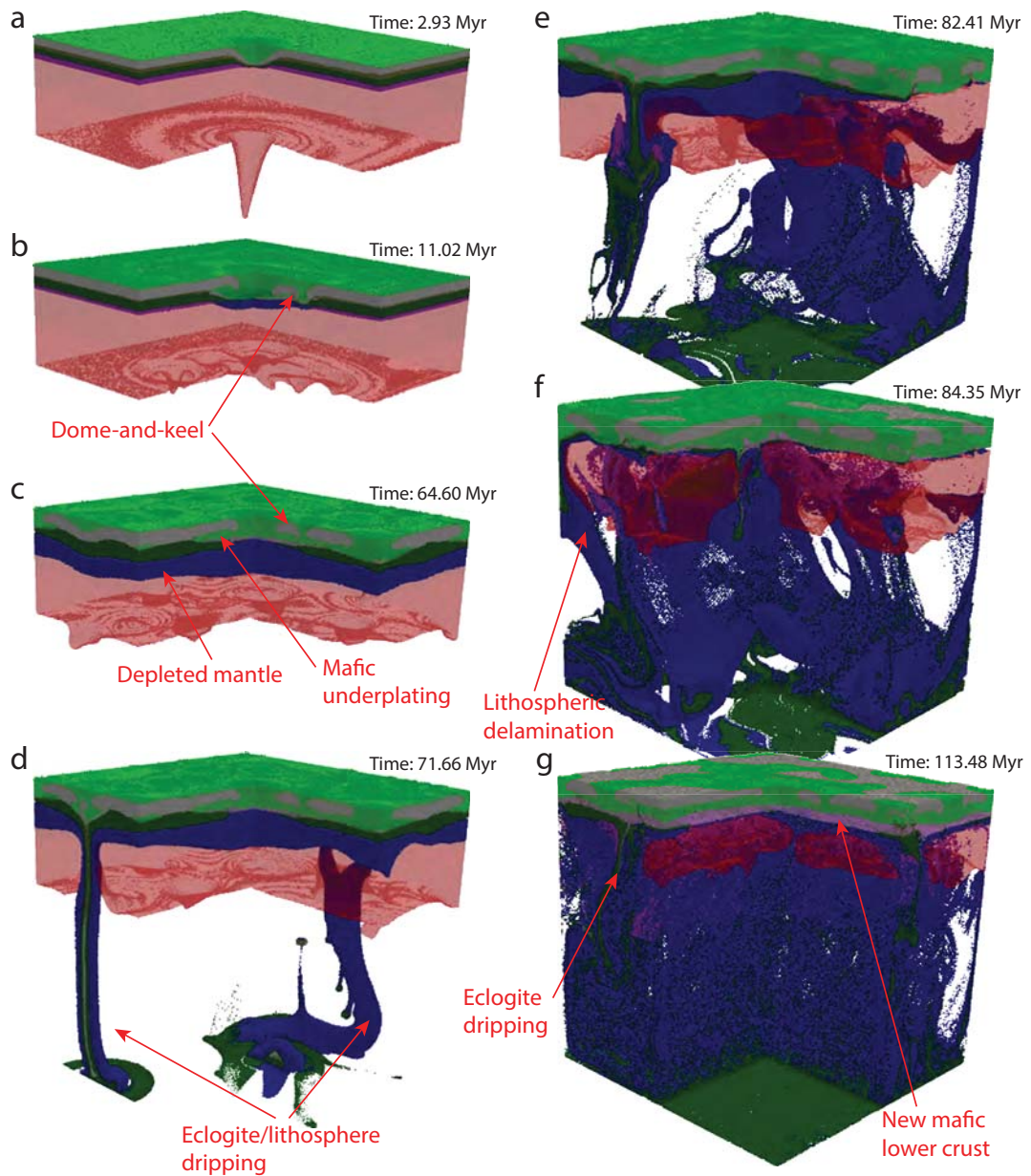


Figure 4.6: Evolution of the model *B100b* with an initial upper felsic and lower mafic crust, eruption efficiency $\chi_{volc} = 100\%$ and no melt-induced weakening ($\lambda_{melt} = 1.0$, $\dot{\epsilon}_{healing} = 0 \text{ s}^{-1}$). (a-c) Newly formed mafic crust sinks through the felsic upper crust, forming a new mid-crustal layer. The crust is thickening to 40 – 50 km and a lithosphere of 20 – 60 km is forming. (d) The overthickened crust is dripping into the mantle forming cold tubes of eclogite and lithospheric mantle peridotite. (e-g) The dripping enhances mantle convection which leads to more subcrustal partial melting and strong removal of lithosphere and lower crust via further dripping, delamination and entrainment. Scales are given in Fig. 4.1a

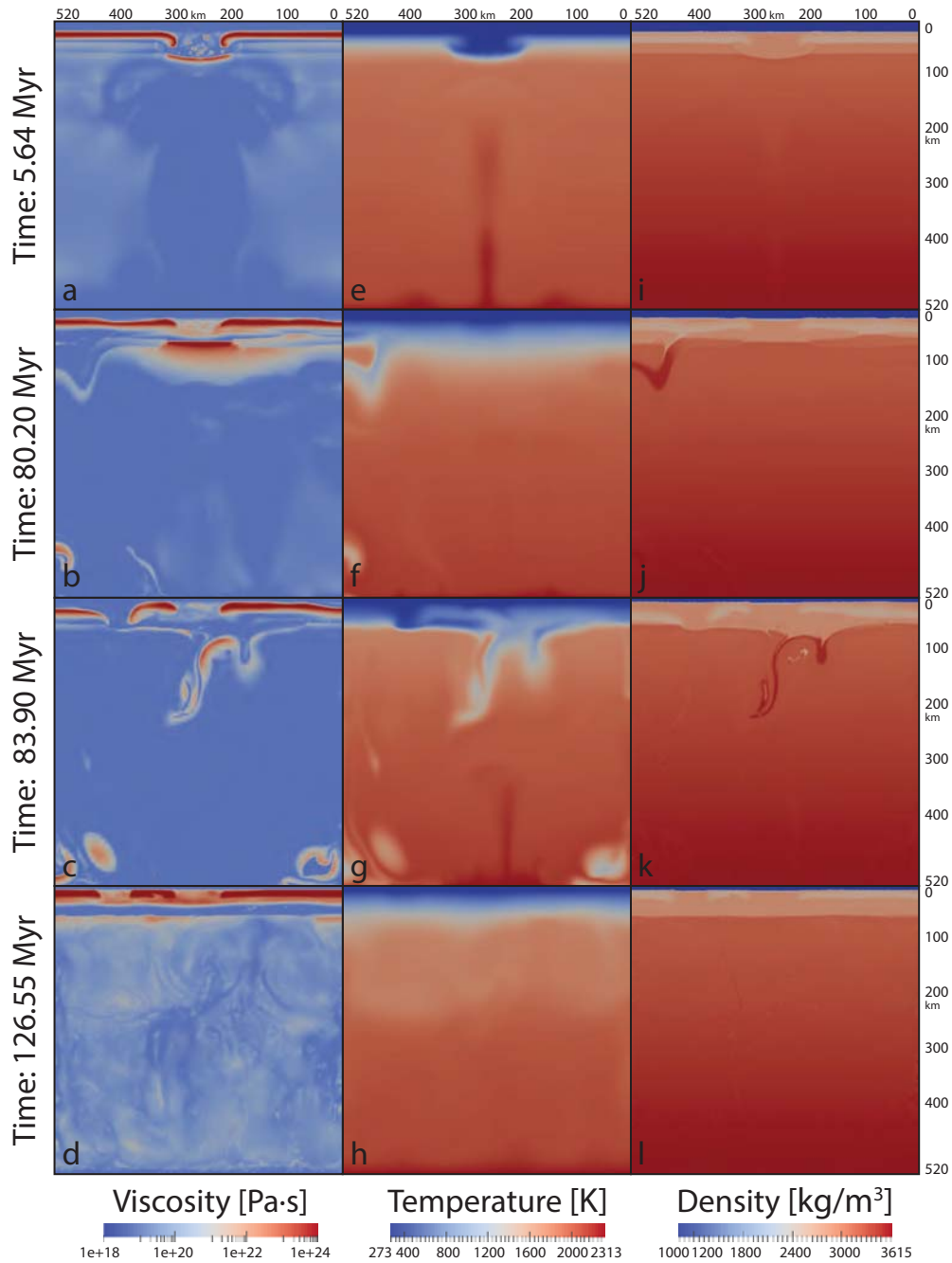


Figure 4.7: Evolution of the model *B100b* with an initial upper felsic and lower mafic crust, eruption efficiency $\chi_{volc} = 100\%$ and no melt-induced weakening ($\lambda_{melt} = 1.0$, $\dot{\epsilon}_{healing} = 0 \text{ s}^{-1}$) in 2D slices. Position of the slices is given in Fig. 4.1a. The left column (a-d) shows the viscosity, the central column (e-h) shows the temperature and the right column (i-l) shows the density. (a,e,i) A high temperature, low viscosity plume rises leading to the formation of a low viscosity, dense, cold volcanic plug on top of the plume. (b,f,j) Transformation of basalt to eclogite forms cold, dense, viscous drips. (c,g,k) An entire layer of eclogite delaminates from the crust. (d,h,l) The mantle is back in its well-mixed state and the crust shows again two distinct layers, however, the upper felsic crust is broken up by two mafic keels.

4.3.4 Influence of melt-induced weakening

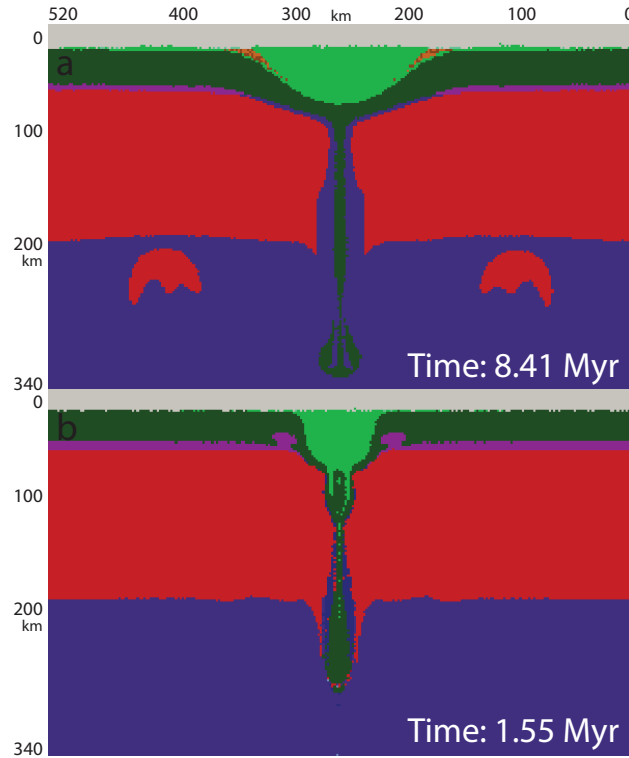


Figure 4.8: Comparison between models (a) *D100b* without melt-induced weakening ($\lambda_{melt} = 1.0$, $\dot{\epsilon}_{healing} = 0 \text{ s}^{-1}$) and (b) *D100* with melt-induced weakening ($\lambda_{melt} = 0.01$, $\dot{\epsilon}_{healing} = 10^{-14} \text{ s}^{-1}$). Both models have the same initial composition of pure mafic crust and an eruption efficiency of $\chi_{volc} = 100\%$. Both panels show a 2D slice at the time of the first eclogite drip. Position of the slices is given in Fig. 4.1a. Model development is similar but in the case of (b) melt-induced weakening it is much faster and more localised. Due to the weakened crust, partial melt is able to rise as diapirs in the lower crust.

Several models have tested the influences of the melt-induced weakening of the lithosphere (Gerya et al., 2015, Fig. 4.8, see Section 2.8 and Table 4.2). The local brittle/plastic strength field above a melting area is weakened during melt extraction episodes ($\lambda_{melt} = 0.01$) whereas previous strain of rocks is rapidly healed at the same time ($\dot{\epsilon}_{healing} = 10^{-14} \text{ s}^{-1}$). If the melt-induced weakening mechanism is suspended ($\lambda_{melt} = 1$, $\dot{\epsilon}_{healing} = 0 \text{ s}^{-1}$), the crust remains equally strong. From similar initial conditions, models with melt-induced weakening generally develop faster (compare e.g. *D100* in Fig. 4.9 with melt-induced weakening and *D100b* in Fig. 4.2 without). Even though both models have no plutonic magmatism, the small amount of crustal partial melt formed due to the initial geotherm is able to rise through the crust as a diapir in the case of melt-weakened crust (Fig. 4.8b). Model *D100* (Fig. 4.9), which has the same

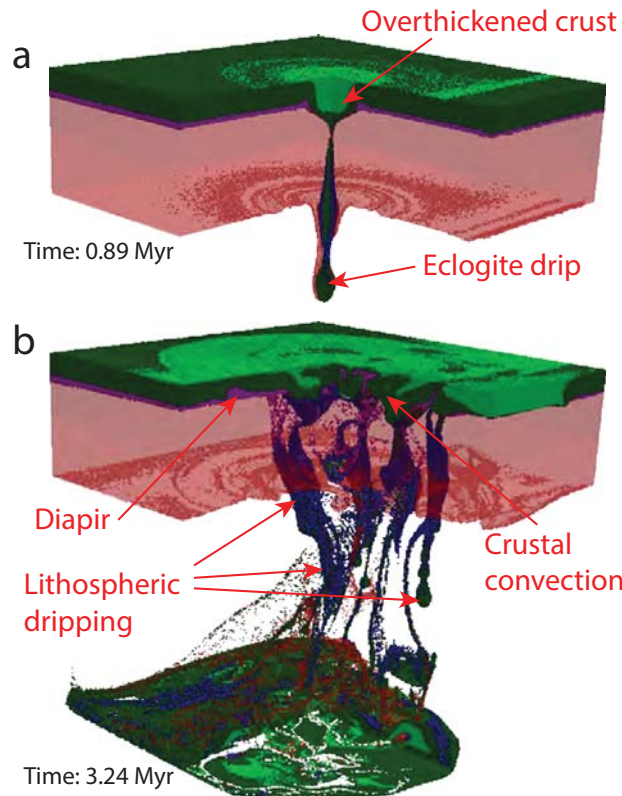


Figure 4.9: Evolution of the model *D100* with initial composition of pure mafic crust, $\chi_{volc} = 100\%$ and melt-induced weakening ($\lambda_{melt} = 0.01$, $\dot{\epsilon}_{healing} = 10^{-14} s^{-1}$). (a) Earliest model development is similar to model *D100b* (Fig. 4.2) but with clear signs of weakening. (b) Weakening of the crust leads to crustal convection and local overthickening which causes formation of eclogite drips. Scales are given in Fig. 4.1a.

model setup as *D100b* with pure mafic crust and eruption efficiency of $\chi_{volc} = 100\%$ but with activated melt-induced weakening ($\lambda_{melt} = 0.01$, $\dot{\epsilon}_{healing} = 10^{-14} s^{-1}$), shows a similar model development to model *D100b* (Fig. 4.2). In both models the crust starts to thicken above the rising mantle plume. A plug of newly formed volcanic crust is forming and as the crust reaches eclogitisation depth, eclogite drips off as a cold thermal-chemical instability (Fig. 4.9a). This process takes ~ 8 Myr without melt-weakening. In the case of melt-induced weakening, the whole process only takes ~ 1 Myr as the weakened crust percolated by melts is not able to support as much weight and the growing plug of newly formed volcanic crust can more easily sink into the initial crust. In addition, partially molten lower crust (which forms due to the steep crustal geotherm) rises through the weakened middle crust in the form of diapirs (Fig. 4.8b). After 3 Myr the strong weakening of the crust and the rising lower crustal

diapirs lead to crustal convection. In regions of newly formed downwelling crust, the crust can locally grow very thick and reach eclogitisation depth. Eclogite dripping due to overthickening therefore occurs early in model development (3 Myr, see Fig. 4.9b) whereas the same eclogite drips in model *D100b* without melt-induced weakening only occur after 60 Myr (Fig. 4.2d).

4.3.5 Influence of layered crust

In the following, three models with a dual-layer crust are introduced, with an upper crust of wet quartzite and a lower crust of plagioclase An₇₅ rheology. All three models have an eruption efficiency of $\chi_{volc} = 20\%$ and melt-induced weakening ($\lambda_{melt} = 0.01$, $\dot{\epsilon}_{healing} = 10^{-14} s^{-1}$).

Model *C20* (Fig. 4.10) contains a layered crust of upper hydrated mafic crust and lower dry mafic crust. In this type of model an intracrustal layer of partially molten upper crust as well as a deep layer of partially molten lower crust is formed. Accumulated partial melt can easily rise from the Moho through the melt-weakened lower crust and reach the midcrustal partial melt layer. The midcrustal layer destabilises as well and the diapir can reach the surface (Figs. 4.10a and 4.10b). The initial large diapir on top of the mantle plumes leads to partial melt spreading on top of the crust. The surface of the diapir is solidified while its edges are compressing the crust, pushing it downwards (Fig. 4.10a). The thickening is also aided by newly formed volcanic crust. The thickened crust along the edges of the diapir forms eclogite and drips off into the mantle in an open tube shape (Fig. 4.10a). These drips initiate further plumes which rise in a concentric pattern around the initial central plume, forming a ring of rising diapirs in the crust. Both processes occur in rapid succession, forming a striking pattern of outward growing rings comprised of alternating diapirs and eclogite drips (Fig. 4.10b). Due to the continuous strong magmatic activity, the partial melt layer is strongly depleted but no solid lithosphere is formed. Cold eclogite drips lead to freezing of the depleted hot mantle and the formation of a solid carapace of lithospheric mantle peridotite around the sinking drips (Figs. 4.10b to 4.10d). Further model development leads to a complete mixing of the crust, resulting in a thin brittle crustal lid (~ 10 km) above the lower partially molten layer (~ 30 km) which is vigorously convecting (Figs. 4.10c and 4.10d). Both layers are strongly inhomogeneous with laterally varying topography of their upper and lower boundaries.

Model *A20* has a purely felsic crust. It is two-layered with an upper crust with wet quartzite rheology and a lower crust with plagioclase An₇₅ flow law. On top of the rising mantle plume at the bottom of the crust, enough partial melt is accumulated to be able to rise through the entire crust (Fig. 4.11a). New magmatic crust is formed on top of this molten diapir and starts to sink along its edges. This downward motion triggers an upward motion further away from the model centre and with it a second ring of diapirs (Figs. 4.11a and 4.11b). As in the model *C20* described above, both crustal layers are partially molten at the bottom. Moving outwards from the central disturbance, diapirs start to rise from the upper and lower layer of partial melt independently, leading to a separate overturn of upper and lower crust (Figs. 4.11b and 4.11c). However, after ~ 1 Myr the two separately convecting layers start to mix (Fig. 4.11d), soon (~ 3 Myr) forming an upper solid layer and a lower partially molten layer (Figs. 4.11d and 4.11e). However, the crust is still strongly convecting with upwelling partial melt and sinking solid upper crust. Above regions of hot mantle upwellings corresponding to the original and secondary plumes, the initial upper crustal layer is destroyed by rising diapirs and new basaltic crust is formed (Figs. 4.11c and 4.11f). This newly formed crust sinks through the solid and partially molten felsic crust to the Moho and leaves only thin belts of mafic traces at the surface (Fig. 4.11g) comparable with models *B100b* (Fig. 4.6) and *E100b* (Fig. 4.5). In regions of cold mantle downwellings, depleted partially molten upper mantle solidifies and forms embryonic dripping mantle lithosphere (Figs. 4.11f to 4.11h).

Model *B20* (Fig. 4.12) has the same setup as *C20* (Fig. 4.10) and *A20* (Fig. 4.11) but with a hydrated felsic upper crust and a mafic lower crust. The central crustal diapir formed on top of the mantle plume is able to rise through both crustal layers. New mafic crust is formed around the edges of the diapir and a ring of secondary diapirs is initiated at the bottom of the lower crust (Fig. 4.12a). The partial melt layers of upper and lower crust start to rise separately and upper and lower crust start to overturn individually (Figs. 4.12b and 4.12c). Rising mantle plumes are able to produce enough magma such that large diapirs on top of the plumes can reach the surface. New mafic crust is produced at the surface (Fig. 4.12d), which has negative buoyancy compared to the underlying felsic crust and starts to subside as soon as plume activity ceases (Fig. 4.12e). This newly formed volcanic crust can only sink through the upper felsic layer and accumulates at midcrustal level, leaving behind thin belts of mafic material at the surface (Fig. 4.6f). After 20 Myr of model development the large-scale crustal structure becomes rather similar to the initial condition for this experiment: 20 km of

felsic upper crust and 20 km of mafic lower crust. Further model development leads to the formation of embryonic mantle lithosphere in places of mantle downwellings. After 26 Myr the lower crust reaches the eclogite transition depth and eclogitised mafic crust drips into the mantle.

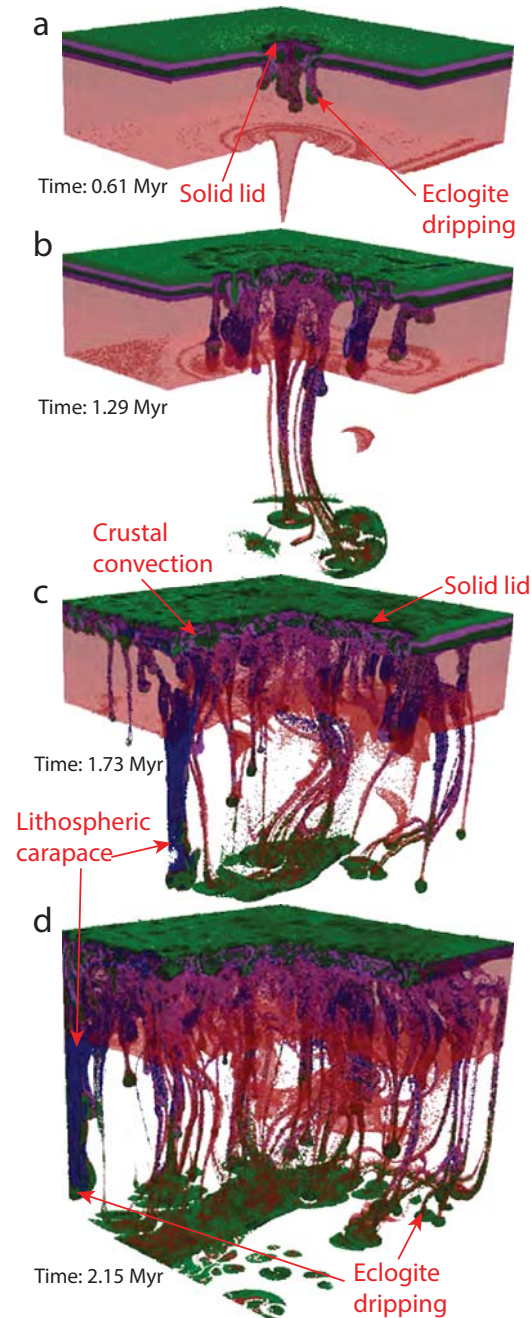


Figure 4.10: Evolution of the model *C20* with an upper hydrated mafic crust and a lower dry mafic crust. The eruption efficiency is $\chi_{volc} = 20\%$ and melt-induced weakening is activated ($\lambda_{melt} = 0.01$, $\dot{\epsilon}_{healing} = 10^{-14} s^{-1}$). (a) The melt-weakened crust allows diapirs to rise through the crust to the surface. Thickening of the crust around the rising diapir due to compression and newly formed volcanic crust leads to eclogitisation and tube-shaped drip off. (b) Dripping initiates further diapirs which rise in a concentric pattern around the initial central plume, which together with further drips form a pattern of outward growing rings comprised of alternating diapirs and eclogite drips. (c-d) Complete mixing of the crust leads to a thin brittle lid on top of the vigorously convecting crust. Scales are given in Fig. 4.1a.

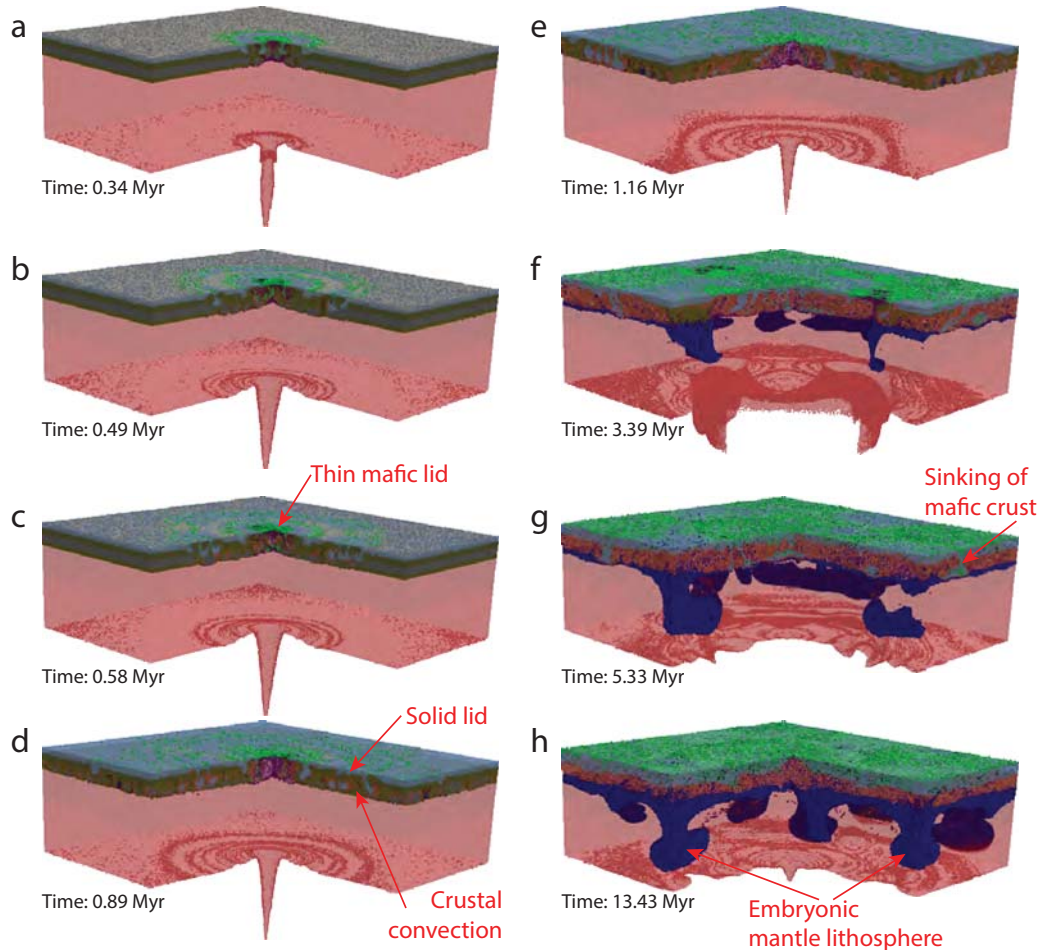


Figure 4.11: Evolution of the model *A20* with an upper hydrated and a lower dry felsic crust. The eruption efficiency is $\chi_{volc} = 20\%$ and melt-induced weakening is activated ($\lambda_{melt} = 0.01$, $\dot{\epsilon}_{healing} = 10^{-14} s^{-1}$). (a) The melt-weakened crust allows diapirs to rise through the crust to the surface. (b-c) Thickening of the crust around the rising diapir due to compression and newly formed volcanic crust leads to separate convection in the upper and lower crust. (d-e) Formation of a thin brittle upper lid introduces the whole-crustal convection regime. (f) On top of mantle plumes, the original crust is destroyed and a thin new mafic crust is formed. (g-h) The newly formed mafic crust sinks through the entire crust leaving only thin traces at the surface. Scales are given in Fig. 4.1a.

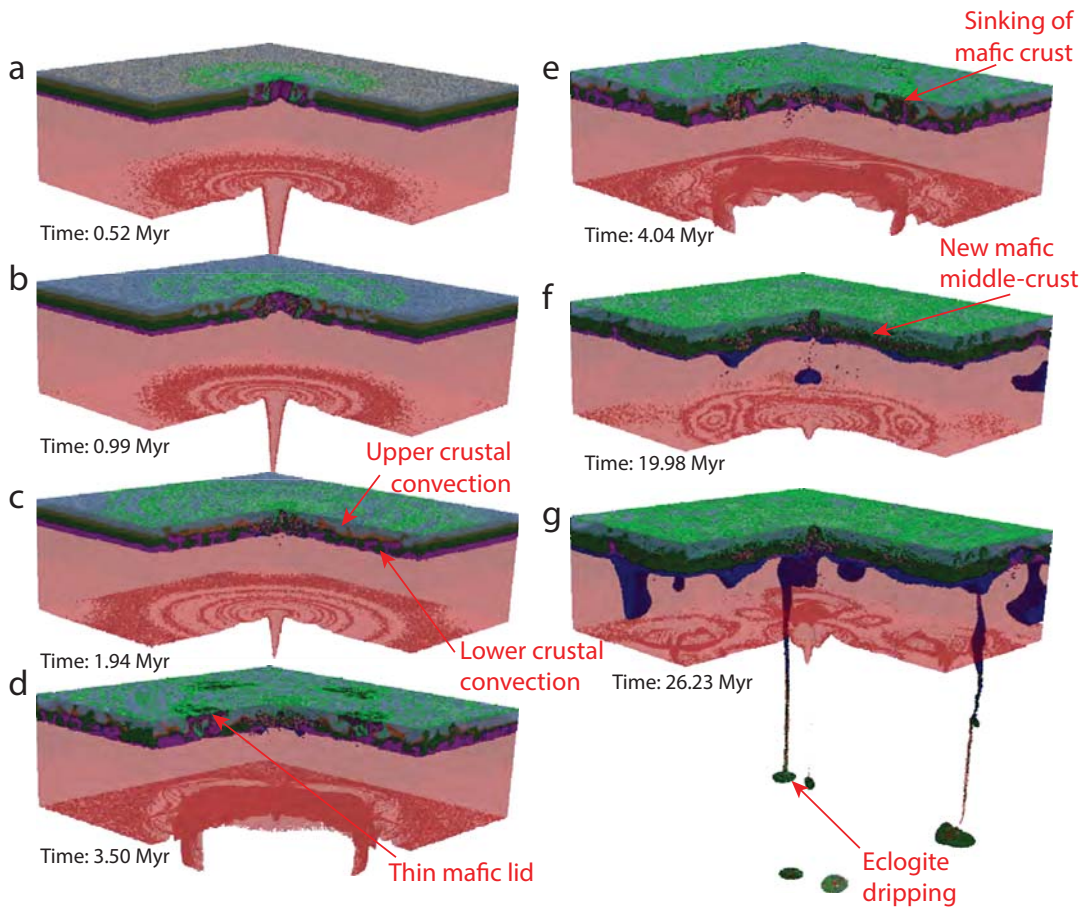


Figure 4.12: Evolution of the model *B20* with an upper hydrated felsic crust and a lower dry mafic crust. The eruption efficiency is $\chi_{volc} = 20\%$ and melt-induced weakening is activated ($\lambda_{melt} = 0.01$, $\dot{\epsilon}_{healing} = 10^{-14} s^{-1}$). (a) Diapirs rise through the melt-weakened crust to the surface. (b-c) The rising central diapir initiates separate upper and lower crustal convection. (d) On top of mantle plumes, the original crust is destroyed and a thin new mafic crust is formed. (e-f) The newly formed mafic crust sinks to the upper-lower crust boundary forming a new mafic middle crust. (g) Eclogite drips sink from the overthickened lower mafic crust into the mantle. Scales are given in Fig. 4.1a.

4.4 Discussion

4.4.1 Magmatic processes, short-term crustal thickening and over-turn, crustal tectonics

Due to the higher temperature in the early Earth, all magmatic processes are intensified. Strong volcanism is produced by heat-piping (Moore and Webb, 2013) and deposited at the surface in large volumes of high-temperature lava-flows similar to present-day flood basalts. This flood volcanism was common in the Archean (Arndt, 1999; Van Kranendonk et al., 2007, 2014b). If it occurs on top of mafic crust (models D and C20), the crust is thickened by adding newly formed volcanic rocks on the top (Smithies et al., 2009; Van Kranendonk et al., 2004, 2014b). If this flood volcanism occurs on felsic crust, an unstable layering is established which creates favourable conditions for gravitational overturns (Collins et al., 1998; Champion and Smithies, 2007; Van Kranendonk et al., 2004, 2014a,b).

At the same time, magmatic intrusions are accumulated in the lower crust and (sometimes) below the thin mantle lithosphere (Fig. 4.3), which triggers crustal diapirism developing in several phases.

Both processes – flood volcanism on felsic crust, as well as plutonic magmatism – encourage convective overturn of the crust. In a stronger crust, sinking of mafic newly formed volcanic rocks into the felsic crust and diapiric rise of the underlying felsic crust leads to a convective overturn and the formation of the typical dome-and-keel pattern observed in several cratons, e.g. East Pilbara in Western Australia (Van Kranendonk et al., 2004; Hickman, 2004), Kaapvaal in South Africa (Van Kranendonk, 2011a). In a weaker crust, where a larger part of the crust is partially molten, this diapiric sinking and rising takes on the form of a rapid intense convection, driven by the sinking of cold basaltic crust and the rising of hot plutonic partially molten rocks (Fig. 4.13a; Collins et al., 1998).

In addition, burial of radiogenic felsic crust under mafic volcanic rocks may have an important effect for creating a hotter crustal geotherm (Gerya et al., 2002; Rey et al., 2003; Sandiford et al., 2004). It is, however, difficult to evaluate this effect for studied models due to the dominance of heat advection processes by crustal overturns.

The mafic newly formed volcanic rocks sink through the felsic crust and accumulate at its bottom, thus effectively forming a new lower crust. If a lower mafic crust is already present, the sinking material is added at the upper to lower crustal interface, in this way thickening the lower crust. A similar structure has been observed for both the Pilbara and the Kaapvaal craton (Van Kranendonk et al., 2014b).

4.4.2 Crustal thickening, destabilisation and recycling into the mantle

As described above, the crust is thickening over time in several ways due to intense magmatism. Because of crustal convective overturn, the lower crust has in most cases mafic composition. As soon as the thickening crust reaches eclogite PT-conditions, the mafic lower crust transforms to eclogite and drips off into the mantle. This thermochemical instability of negatively buoyant material can trigger further instabilities of thermal and thermochemical nature leading to dripping of the mantle lithosphere and eclogitised lower crust, which may also incorporate felsic crustal rocks (Fig. 4.6d). Drips can have several forms: cylindrical triggered by overthickening, hollow cylindrical curtains e.g. triggered by plume (Gerya et al., 2015) and linear (sheet-like) curtains triggered by horizontal compression (Göğüş and Pysklywec, 2008a; Fischer and Gerya, submitted for publication). Convective mantle return flow due to dripping (Göğüş and Pysklywec, 2008b) can lead to weakening of the lithosphere and lower crust and initiate delamination along a weak zone (Göğüş and Pysklywec, 2008a) such as the Moho, the lower-upper crust boundary or even a middle crustal weak buried (meta)sedimentary layer (Figs. 4.2e and 4.2f).

4.4.3 Long-term tectonic processes

From a long-term perspective (10s to 100s of Myr), the short-term event of crustal overturn as described above occurs several times in succession as short singular events. During several overturn events the crust is thickening during the period of relative quiescence ('growth phase') until the lower crust becomes gravitationally unstable due to its thickening and eclogitisation. A short turbulent chaotic 'removal phase' follows with delamination of large parts of the lower crust and mantle lithosphere within a few Myr: a resurfacing event. After this resurfacing event, thickness of the crust changes to its original (equilibrium) value whereas mantle lithosphere is completely removed and

starts to grow again from the depleted hot upper mantle (Figs. 4.2, 4.3 and 4.6). Similar processes can also be observed in nature where Hickman and Van Kranendonk (2004) documented in the East Pilbara several active volcanic cycles of ~ 15 Ma interrupted by long periods quiescence.

4.4.4 Mantle convection patterns and lithospheric growth

The mantle in all models is vigorously convecting. In most models a two-layered mantle convection can be observed. The partially molten part of the mantle has a thickness of ~ 120 km. It is forming a separate layer (marked in red in Figs. 4.13a and 4.13b) which is convecting in a strongly unstable, chaotic manner, forming several small-scale convection cells, which are strongly influenced by rising plumes from below as well as cold sinking eclogitised crustal material from above (Fig. 4.13a). The lower part of the model forms a second convection layer with more stable, larger-scale convection cells below the partially molten mantle layer. During crustal and lithospheric growth 1 – 2 stable convection cells can be observed. However, also in this more stable layer the convection patterns change several times during the model run, either due to plumes rising from different location at the bottom boundary or due to cold crustal and lithospheric material sinking down into the mantle.

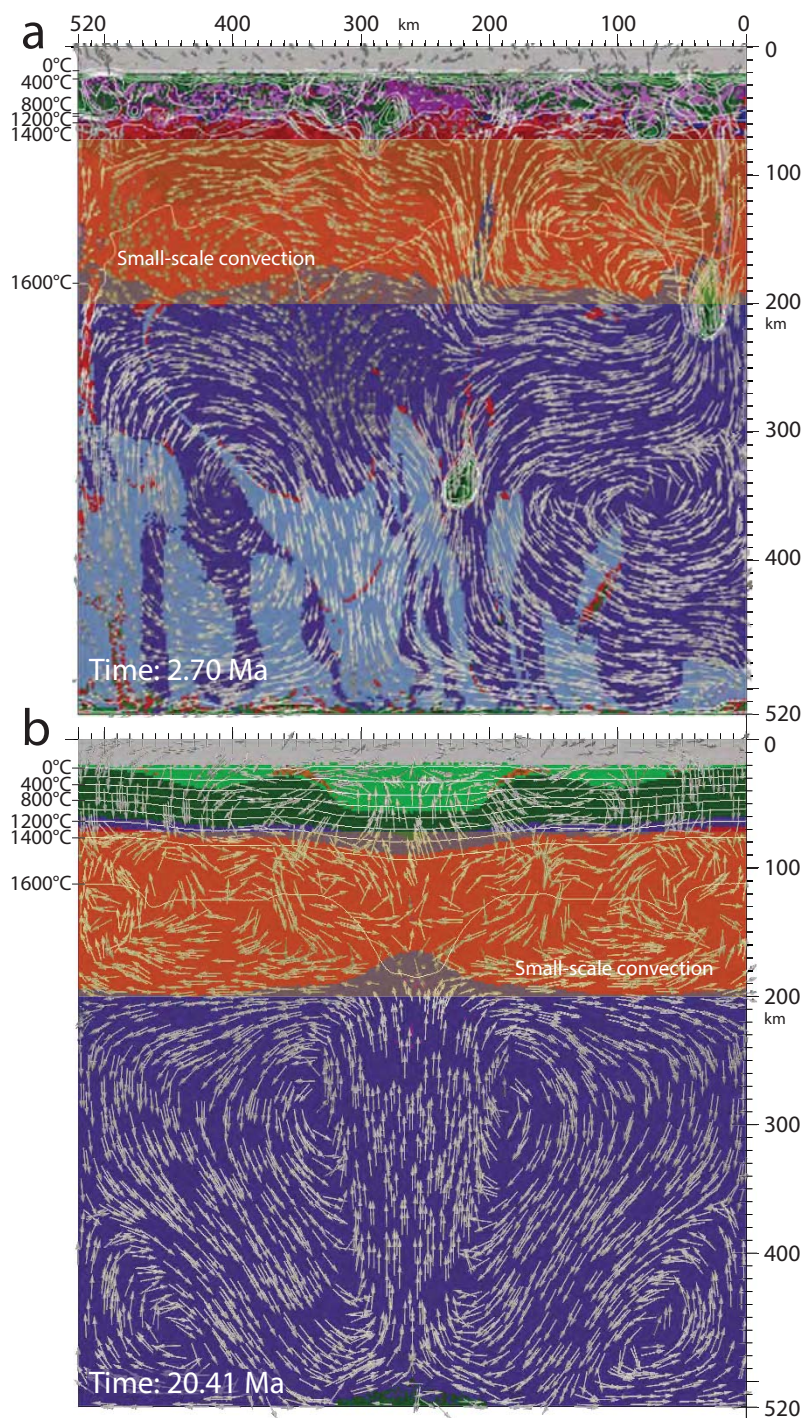


Figure 4.13: 2D compositional slice of (a) model *C20* (Table 4.2 and Fig. 4.10) and (b) model *D100b* (Table 4.2 and Fig. 4.2). Position of the slices is given in Fig. 4.1a. White isolines mark the temperature; arrows mark the velocity field. Three distinct convective layers can be observed: (1) a lower stably convecting mantle layer, (2) an upper chaotically convecting mantle layer (marked in red) and (3) the convecting crust.

4.4.5 PT-conditions for generation of TTG-crust

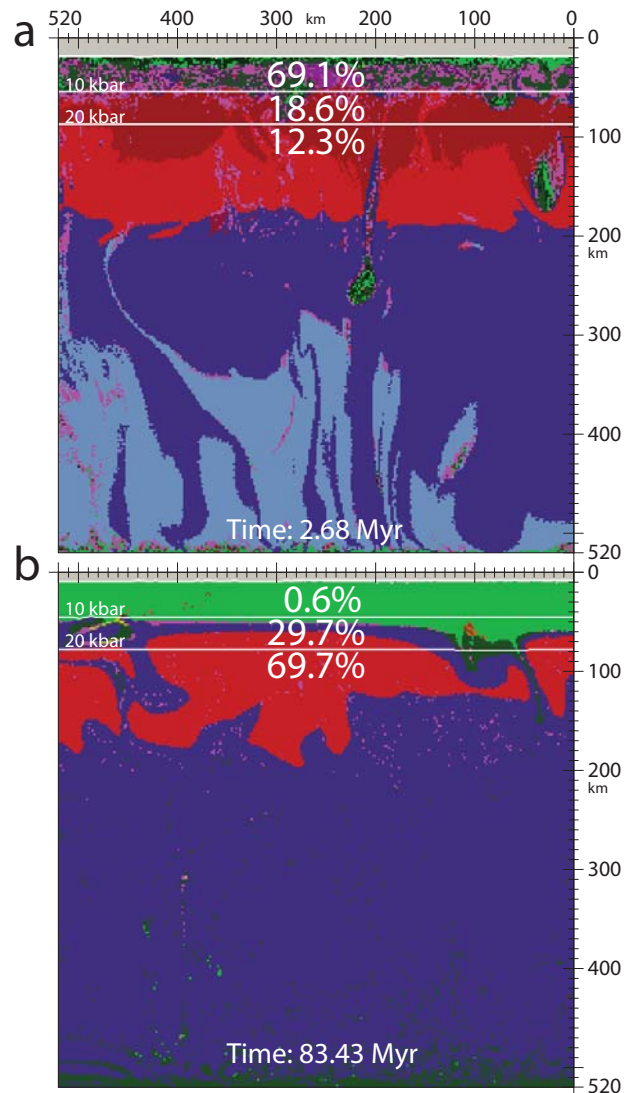


Figure 4.14: 2D compositional slice of (a) model *C20* (Table 4.2 and Fig. 4.10) and (b) model *D100b* (Table 4.2 and Fig. 4.2). Position of the slice is given in Fig. 4.1a. White isolines mark the 0, 10 and 20 kbar pressure isosurface. All hydrated partially molten mafic rocks, which act as potential TTG source melts, are marked in purple and their percentage in each pressure band is given.

The timing, volume and detailed process of the formation of felsic continental crust are strongly debatable. However, most authors agree that felsic crust and with it its early Earth representation, the TTG rocks, must have formed by successive remelting of hydrated mafic rocks (Hawkesworth and Kemp, 2006). Even though this code does not support formation of felsic rocks from basaltic partial melt, it is still possible

to evaluate the PT-conditions for occurrence of partially molten mafic rocks, which would potentially act as the source melt regions for the formation of TTGs. According to Moyen (2011) approximately 20% of all TTGs stem from sources at low pressure (0 – 10 kbar), 60% stem from medium pressure sources of 10 – 20 kbar and another 20% from high-pressure sources > 20 kbar.

Taking into account all basaltic partial melt and calculating its percentage for low-, mid- and high-pressure range for two different models *C20* (Fig. 4.14a) and *D100b* (Fig. 4.14b), however, leads to very different results. Even though both models start out with the same model setup of 35 km of mafic crust, model *D100b* at 83 Myr ends up with almost no partially molten basaltic crust in the low-pressure region, 30% in the mid-pressure region and 70% in the high-pressure region (Fig. 4.14b). Whereas in the case of model *C20* (at 2.7 Myr) the partially molten basaltic crust is distributed as follows: 70% in the low-pressure, 20% in the mid-pressure and 10% in the high-pressure region (Fig. 4.14a).

The last available timestep of model *C20* is much younger than model *D100b*. Model *C20* can therefore be interpreted as representing a very early stage of evolution of model *D100b*. This early first stage which is dominated by crustal overturn and convection mainly produces partially molten basalt in the uppermost region between 0 – 10 kbar (Fig. 4.14a). In Fig. 4.14b from model *D100b* crustal overturn and a catastrophic resurfacing event has already occurred and the model is back in its initial stage where the crust starts to thicken again. In this case, almost no partial melt is found in the crust but the major regions of basalt melting are located within deep eclogitised domains. These regions correspond either to partially molten lower crust or to partially molten remnants of dripping or delaminating crust. The total volume of partially molten basaltic rocks in *D100b* is only 15% of their volume present in *C20*. The volume of mid- and high-pressure partially molten basaltic crust is about the same, while the volume of low-pressure partially molten basaltic crust in model *C20* is almost 1000 times higher.

We, therefore, conclude that the amount of low-, mid- and high-pressure basaltic TTG source melt varies throughout the different stages of the Archean tectonic process and major TTG-crust formation episodes should correspond to short, hot and rapid overturn events (‘removal phase’, Figs. 4.3b and 4.13a) rather than to periods of relative tectono-magmatic quiescence and lithospheric thickening (‘growth phase’, Figs. 4.3e and 4.13b, see also Smithies et al., 2009).

4.4.6 Consequences for subduction initiation

The shift from early Earth plume-lid tectonics to plate tectonics is one of the major research questions (Shirey and Richardson, 2011; Van Kranendonk, 2011b; Gerya et al., 2015, and references therein). A possible answer would be plume-induced subduction (Ueda et al., 2008; Van Kranendonk, 2010; Gerya et al., 2015). Similar beginnings are observed in several models (mainly with melt-induced weakening): e.g. Fig. 4.10a, Figs. 4.3f and 4.3g, Figs. 4.4d to 4.4f and Figs. 4.2e and 4.2f. However, the sinking tube-shaped ‘slab’ is much too weak (see also van Hunen and van den Berg, 2008) to continue a subduction and tends to form a circular drip and to neck off while the crustal plateau continues to grow (Champion and Smithies, 2007; Van Kranendonk et al., 2007, 2014b; Gerya et al., 2015).

4.5 Conclusion

Archean plume-lid tectonics are predominantly tectono-magmatic and mainly driven by strong crustal and lithospheric growth. The overthickened unstable crust is removed by means of eclogite drips or drip tectonics (Herzberg, 2014) and delamination. On the one hand, asthenospheric mantle flow drives crustal growth, deformation and episodic thinning by eclogite recycling and, on the other hand, it is strongly modified by the dripping of crustal material back into the mantle. We also found that the crust forms a separate convection layer, with convection being assisted by the doming of magmatic plutons and the sinking of basaltic crust formed by flood volcanism (Arndt, 1999; Van Kranendonk, 2011a). This yields an extremely efficient way of heat removal through the crust via convection and conduction through the thinned brittle upper crustal lid and could provide an answer to the Archean paradox as described by Moresi (2013) in addition to the heat-pipe model (Moore and Webb, 2013). Furthermore we found Archean plume-lid tectonics to be separated into two distinct phases: (1) A longer and relatively quiet ‘growth phase’, where crust and lithosphere grow in thickness. (2) This is followed by a short and catastrophic ‘removal phase’, where unstable parts of the crust and lithosphere are removed first via dripping and later via delamination. This pattern of episodic overturn has already been suggested for the Archean by several authors: Kröner and Layer (1992); Zegers and van Keken (2001); van Thienen et al. (2005b); Bédard (2006).

Supplementary materials

Table 4.S1: Alternative values used for models *B100b*, *D0b*, *D100b* and *E100b* (Table 4.2). Material properties^a as well as applied rheology and melting model are listed for each of the used lithologies as given in Fig. 4.1b.

Material	Rheology [MPa ⁻ⁿ s ⁻¹], [-], [kJ], [$\frac{J}{bar}$]	ρ_0 [$\frac{kg}{m^3}$]	k [K]	Melting [$\frac{W}{m^2K}$]	H_r ^b [$\frac{\mu W}{m^3}$]	H_L [$\frac{kJ}{kg}$]	C_0, C_1 [MPa]	ϕ_0, ϕ_1 [-]	γ_0, γ_1 [-]	σ_{crit} [MPa]	C_p [$\frac{kJ}{kg}$]
Sediments	Wet quartzite flow law $B_D = 1.97 \cdot 10^{17}$, $n = 2.3$, $E_a = 154$, $V_a = 0$	2600 solid 2400 molten	$0.64 + \frac{807}{T+77}$	Granite	2.0	-	1, 1	0.2, 0.2	0.0, 0.25	0.03	1.0
Upper felsic crust		2400 molten 2750 solid			2.0	300	1, 1	-	-	-	1.0
Hydrated felsic crust	-//-	2400 molten 2700 solid	-//-	-//-	2.0	300	1, 1	-	-	-	1.0
Lower felsic crust		2400 molten 2950 solid		Basalt	1.0	300	1, 1	-	-	-	1.5
		2400 molten		-//-	2.0	380	1, 1	-	-	-	1.0
Upper mafic crust	Plagioclase An_{75} flow law $B_D = 4.80 \cdot 10^{22}$, $n = 3.2$, $E_a = 238$, $V_a = 0$	3000 solid 2800 molten	$1.18 + \frac{474}{T+77}$	Gabbro	0.25	-	10, 3	0.6, 0.0	0.0, 0.25	0.03	1.0
Lower mafic crust		3000 solid 2800 molten	-//-	-//-	0.25	380	3, 3	-	-	-	1.0
Hydrated mafic crust	-//-	2900 solid 2400 molten		Basalt	0.5	380	3, 3	-	-	-	1.0
		2400 molten	$0.64 + \frac{807}{T+77}$	-//-	1.0	380	1, 1	-	-	-	1.5
Depleted mantle	Dry olivine flow law $B_D = 3.98 \cdot 10^{16}$, $n = 3.5$, $E_a = 532$, $V_a = 1.6$ $V_{quenched} = 0.8$	3300 solid 2900 molten	$0.73 + \frac{1293}{T+77}$	Peridotite	0.022	-	10, 3	0.6, 0.0	0.0, 0.25	0.03	1.0
Resolidified mantle		3200 solid 2900 molten	-//-	-//-	0.022	400	3, 3	-	-	-	1.0
Mantle	Wet olivine flow law $B_D = 5.01 \cdot 10^{20}$, $n = 4.0$, $E_a = 470$, $V_a = 0.8$	3300 solid 2900 molten	$0.73 + \frac{1293}{T+77}$	Peridotite	0.022	-	10, 3	0.6, 0.0	0.0, 0.25	0.03	1.0
Hydrated mantle		3300 solid 2800 molten	-//-	-//-	0.024	400	3, 3	0.1, 0.0	0.0, 0.25	0.03	1.0
Serpentinite	-//-	2800 molten 3100 solid			0.022	400	3, 3	-	-	-	1.5
References ^c		4,1	1,2	3	5-10	1	1,2	0.1, 0.0	0.0, 0.25	0.03	1.0

^a for all rock types: Thermal expansion coefficient $\alpha = 3.0 \cdot 10^{-5} K^{-1}$ and compressibility $\beta = 1.0 \cdot 10^{-5} GPa^{-1}$.

^b fixed at present-day values as the influence of radiogenic heating is negligible compared to increased mantle temperature (Sizova et al., 2010).

^c (1) Turcotte and Schubert (2002), (2) Bittner and Schmelting (1995), (3) Clauser and Huenges (1995), (4) Ranalli (1995), (5) Schmidt and Poli (1998), (6) Johannes (1985), (7) Poli and Schmidt (2002), (8) Schmidt and Poli (1998), (9) Hess (1989), (10) Katz et al. (2003)

References

- M. Armann and P. J. Tackley. Simulating the thermochemical magmatic and tectonic evolution of Venus's mantle and lithosphere: Two-dimensional models. *Journal of Geophysical Research: Planets*, 117(E12):E12003, 2012.
- N. Arndt. Why was flood volcanism on submerged continental platforms so common in the Precambrian? *Precambrian Research*, 97(3–4):155–164, 1999.
- J. H. Bédard. A catalytic delamination-driven model for coupled genesis of Archean crust and sub-continental lithospheric mantle. *Geochimica et Cosmochimica Acta*, 70(5):1188–1214, 2006.
- K. Benn, J.-C. Mareschal, and K. C. Condie. Introduction: Archean Geodynamics and Environments. In *Archean Geodynamics and Environments*, pages 1–5. American Geophysical Union, 2006.
- D. Bittner and H. Schmeling. Numerical Modelling of Melting Processes and Induced Diapirism In the Lower Crust. *Geophysical Journal International*, 123(1):59–70, 1995.
- D. Breuer and W. B. Moore. Dynamics and Thermal History of the Terrestrial Planets, the Moon, and Io. In S. Gerald, editor, *Treatise on Geophysics*, pages 299–348. Elsevier, Amsterdam, 2007.
- M. Brown. Metamorphic Conditions in Orogenic Belts: A Record of Secular Change. *International Geology Review*, 49(3):193–234, 2007.
- E. Burov and T. Gerya. Asymmetric three-dimensional topography over mantle plumes. *Nature*, 513(7516):85–89, 2014.
- D. C. Champion and R. H. Smithies. Geochemistry of Paleoarchean Granites of the East Pilbara Terrane, Pilbara Craton, Western Australia: Implications for Early Archean Crustal Growth. In R. H. S. Martin J. van Kranendonk and C. B. Vickie, editors, *Developments in Precambrian Geology*, volume Volume 15, chapter 4.3, pages 369–409. Elsevier, 2007.
- C. Clauser and E. Huenges. Thermal Conductivity of Rocks and Minerals. In T. Ahrens, editor, *Rock Physics and Phase Relations*, volume 3, pages 105–126. AGU Reference Shelf, 1995.

- W. Collins, V. Kranendonk, MJ, and C. Teyssier. Partial convective overturn of Archaean crust in the east Pilbara Craton, Western Australia: driving mechanisms and tectonic implications. *Journal of Structural Geology*, 20(9):1405–1424, 1998.
- F. Crameri, H. Schmeling, G. J. Golabek, T. Duretz, R. Orendt, S. J. H. Buitter, D. A. May, B. J. P. Kaus, T. V. Gerya, and P. J. Tackley. A comparison of numerical surface topography calculations in geodynamic modelling: an evaluation of the ‘sticky air’ method. *Geophysical Journal International*, 189(1):38–54, 2012.
- J. A. Crisp. Rates of magma emplacement and volcanic output. *Journal of Volcanology and Geothermal Research*, 20(3–4):177–211, 1984.
- R. Fischer and T. Gerya. Early Earth plume tectonics: A high-resolution 3D numerical modelling approach. *Journal of Geodynamics*, in press.
- R. Fischer and T. Gerya. Regimes of subduction and lithospheric dynamics in the Precambrian: 3D thermomechanical modelling. *Gondwana Research*, submitted for publication.
- O. H. Göğüş and R. N. Pysklywec. Mantle lithosphere delamination driving plateau uplift and synconvergent extension in eastern Anatolia. *Geology*, 36(9):723–726, 2008a.
- O. H. Göğüş and R. N. Pysklywec. Near-surface diagnostics of dripping or delaminating lithosphere. *Journal of Geophysical Research: Solid Earth*, 113(B11):B11404, 2008b.
- T. Gerya. Precambrian geodynamics: Concepts and models. *Gondwana Research*, 25(2):442–463, 2014a.
- T. V. Gerya. Plume-induced crustal convection: 3D thermomechanical model and implications for the origin of novae and coronae on Venus. *Earth and Planetary Science Letters*, 391:183–192, 2014b.
- T. V. Gerya and D. A. Yuen. Characteristics-based marker-in-cell method with conservative finite-differences schemes for modeling geological flows with strongly variable transport properties. *Physics of the Earth and Planetary Interiors*, 140(4):293–318, 2003.
- T. V. Gerya and D. A. Yuen. Robust characteristics method for modelling multiphase visco-elasto-plastic thermo-mechanical problems. *Physics of the Earth and Planetary Interiors*, 163(1-4):83–105, 2007.

- T. V. Gerya, L. L. Perchuk, W. V. Maresch, A. P. Willner, D. D. V. Reenen, and C. A. Smit. Thermal regime and gravitational instability of multi-layered continental crust: implications for the buoyant exhumation of high-grade metamorphic rocks. *European Journal of Mineralogy*, 14(4):687–699, 2002.
- T. V. Gerya, R. J. Stern, M. Baes, S. V. Sobolev, and S. A. Whattam. Plate tectonics on the Earth triggered by plume-induced subduction initiation. *Nature*, 527(7577):221–225, 2015.
- V. L. Hansen and J. A. Willis. Structural Analysis of a Sampling of Tesserae: Implications for Venus Geodynamics. *Icarus*, 123(2):296–312, 1996.
- L. B. Harris and J. H. Bédard. Crustal evolution and deformation in a non-plate-tectonic Archaean Earth: Comparisons with Venus. In *Evolution of Archean Crust and Early Life*, pages 215–291. Springer, 2014.
- L. B. Harris and J. H. Bédard. Interactions between continent-like ‘drift’, rifting and mantle flow on Venus: gravity interpretations and Earth analogues. *Geological Society, London, Special Publications*, 401(1):327–356, 2015.
- C. Hawkesworth and A. Kemp. Evolution of the continental crust. *Nature*, 443(7113):811–817, 2006.
- C. Herzberg. Early Earth: Archaean drips. *Nature Geoscience*, 7(1):7–8, 2014.
- C. Herzberg, K. Condie, and J. Korenaga. Thermal history of the Earth and its petrological expression. *Earth and Planetary Science Letters*, 292(1–2):79–88, 2010.
- P. Hess. *Origins of Igneous Rocks*. Harvard University Press, 1989.
- A. Hickman. Two contrasting granite-greenstone terranes in the Pilbara Craton, Australia: evidence for vertical and horizontal tectonic regimes prior to 2900Ma. *Precambrian Research*, 131(3):153–172, 2004.
- A. Hickman and M. Van Kranendonk. Diapiric processes in the formation of Archaean continental crust, East Pilbara granite-greenstone terrane, Australia. In *The Precambrian Earth: tempos and events*, volume 12, pages 118–139. Elsevier, 2004.
- J. Hutton. Theory of the Earth; or an Investigation of the Laws observable in the Composition, Dissolution, and Restoration of Land upon the Globe. *Earth and Environmental Science Transactions of the Royal Society of Edinburgh*, 1(02):209–

304, 1788.

- W. Johannes. The significance of experimental studies for the formation of migmatites. In *Migmatites*, chapter 2, pages 36–85. Springer US, 1985.
- T. E. Johnson, M. Brown, B. J. P. Kaus, and J. A. VanTongeren. Delamination and recycling of Archaean crust caused by gravitational instabilities. *Nature Geoscience*, 7(1):47–52, 2014.
- R. F. Katz, M. Spiegelman, and C. H. Langmuir. A new parameterization of hydrous mantle melting. *Geochemistry Geophysics Geosystems*, 4(9):1073, 2003.
- A. Kröner and P. W. Layer. Crust Formation and Plate Motion in the Early Archaean. *Science*, 256(5062):1405–1411, 1992.
- A. Lenardic, L. N. Moresi, A. M. Jellinek, and M. Manga. Continental insulation, mantle cooling, and the surface area of oceans and continents. *Earth and Planetary Science Letters*, 234(3–4):317–333, 2005.
- W. B. Moore and A. A. G. Webb. Heat-pipe Earth. *Nature*, 501(7468):501–505, 2013.
- L. Moresi. Earth science: A resolution of the Archaean paradox. *Nature*, 501(7468):496–497, 2013.
- J.-F. Moyen. The composite Archaean grey gneisses: Petrological significance, and evidence for a non-unique tectonic setting for Archaean crustal growth. *Lithos*, 123(1–4):21–36, 2011.
- C. O’Neill and D. A. Wyman. Geodynamic Modeling of Late Archaean Subduction: Pressure-Temperature Constraints from Greenstone Belt Diamond Deposits. In *Archaean Geodynamics and Environments*, chapter 11, pages 177–188. American Geophysical Union, 2013.
- R. J. Phillips and V. L. Hansen. Geological Evolution of Venus: Rises, Plains, Plumes, and Plateaus. *Science*, 279(5356):1492–1497, 1998.
- S. Poli and M. W. Schmidt. Petrology of subducted slabs. *Annual Review of Earth and Planetary Sciences*, 30(1):207–235, 2002.
- G. Ranalli. *Rheology of the Earth*. Springer, 1995.
- P. F. Rey, P. Philippot, and N. Thébaud. Contribution of mantle plumes, crustal

- thickening and greenstone blanketing to the 2.75–2.65 Ga global crisis. *Precambrian Research*, 127(1–3):43–60, 2003.
- R. L. Rudnick and S. Gao. 3.01 - Composition of the Continental Crust. In H. D. H. K. Turekian, editor, *Treatise on Geochemistry*, pages 1–64. Pergamon, Oxford, 2003.
- M. Sandiford, M. J. Van Kranendonk, and S. Bodorkos. Conductive incubation and the origin of dome-and-keel structure in Archean granite-greenstone terrains: A model based on the eastern Pilbara Craton, Western Australia. *Tectonics*, 23(1):n/a–n/a, 2004.
- G. G. Schaber, R. G. Strom, H. J. Moore, L. A. Soderblom, R. L. Kirk, D. J. Chadwick, D. D. Dawson, L. R. Gaddis, J. M. Boyce, and J. Russell. Geology and distribution of impact craters on Venus: What are they telling us? *Journal of Geophysical Research: Planets*, 97(E8):13257–13301, 1992.
- M. W. Schmidt and S. Poli. Experimentally based water budgets for dehydrating slabs and consequences for arc magma generation. *Earth and Planetary Science Letters*, 163(1–4):361–379, 1998.
- S. B. Shirey and S. H. Richardson. Start of the Wilson Cycle at 3 Ga Shown by Diamonds from Subcontinental Mantle. *Science*, 333(6041):434–436, 2011.
- E. Sizova, T. Gerya, M. Brown, and L. L. Perchuk. Subduction styles in the Precambrian: Insight from numerical experiments. *Lithos*, 116(3–4):209–229, 2010.
- E. Sizova, T. Gerya, and M. Brown. Contrasting styles of Phanerozoic and Precambrian continental collision. *Gondwana Research*, 25(2):522–545, 2014.
- E. Sizova, T. Gerya, K. Stüwe, and M. Brown. Generation of felsic crust in the Archean: A geodynamic modeling perspective. *Precambrian Research*, 271:198–224, 2015.
- R. H. Smithies, D. C. Champion, and M. J. Van Kranendonk. Formation of Paleoproterozoic continental crust through infracrustal melting of enriched basalt. *Earth and Planetary Science Letters*, 281(3–4):298–306, 2009.
- R. Strom, G. Schaber, and D. Dawson. The global resurfacing of Venus. *Journal of Geophysical Research*, 99(E5):10,899–10,926, 1994.
- D. Turcotte and G. Schubert. *Geodynamics*. Cambridge University Press, 2. edition,

2002.

- K. Ueda, T. Gerya, and S. V. Sobolev. Subduction initiation by thermal–chemical plumes: Numerical studies. *Physics of the Earth and Planetary Interiors*, 171(1–4): 296–312, 2008.
- J. van Hunen and J.-F. Moyen. Archean Subduction: Fact or Fiction? *Annual Review of Earth and Planetary Sciences*, 40(1):195–219, 2012.
- J. van Hunen and A. P. van den Berg. Plate tectonics on the early Earth: Limitations imposed by strength and buoyancy of subducted lithosphere. *Lithos*, 103(1–2):217–235, 2008.
- M. J. Van Kranendonk. Two types of Archean continental crust: Plume and plate tectonics on early Earth. *American Journal of Science*, 310(10):1187–1209, 2010.
- M. J. Van Kranendonk. Cool greenstone drips and the role of partial convective overturn in Barberton greenstone belt evolution. *Journal of African Earth Sciences*, 60(5):346–352, 2011a.
- M. J. Van Kranendonk. Onset of Plate Tectonics. *Science*, 333(6041):413–414, 2011b.
- M. J. Van Kranendonk, W. Collins, A. Hickman, and M. J. Pawley. Critical tests of vertical vs. horizontal tectonic models for the Archaean East Pilbara granite–greenstone terrane, Pilbara craton, western Australia. *Precambrian Research*, 131(3):173–211, 2004.
- M. J. Van Kranendonk, R. H. Smithies, A. H. Hickman, and D. C. Champion. Chapter 4.1 Paleoarchean Development of a Continental Nucleus: the East Pilbara Terrane of the Pilbara Craton, Western Australia. In R. H. S. Martin J. van Kranendonk and C. B. Vickie, editors, *Developments in Precambrian Geology*, volume Volume 15, pages 307–337. Elsevier, 2007.
- M. J. Van Kranendonk, A. Kröner, J. E. Hoffmann, T. Nagel, and C. R. Anhaeusser. Just another drip: Re-analysis of a proposed Mesoarchean suture from the Barberton Mountain Land, South Africa. *Precambrian Research*, 254:19–35, 2014a.
- M. J. Van Kranendonk, R. H. Smithies, W. L. Griffin, D. L. Huston, A. H. Hickman, D. C. Champion, C. R. Anhaeusser, and F. Pirajno. Making it thick: a volcanic plateau origin of Palaeoarchean continental lithosphere of the Pilbara and Kaapvaal cratons. *Geological Society, London, Special Publications*, 389, 2014b.

- P. van Thienen, J. van Summeren, R. Van der Hilst, A. Van den Berg, and N. Vlaar. Numerical study of the origin and stability of chemically distinct reservoirs deep in Earth's mantle. *Geophysical monograph*, 2005a.
- P. van Thienen, N. J. Vlaar, and A. P. van den Berg. Assessment of the cooling capacity of plate tectonics and flood volcanism in the evolution of Earth, Mars and Venus. *Physics of the Earth and Planetary Interiors*, 150(4):287–315, 2005b.
- T. E. Zegers and P. E. van Keken. Middle Archean continent formation by crustal delamination. *Geology*, 29(12):1083–1086, 2001.
- G. Zhu, T. V. Gerya, P. J. Tackley, and E. Kissling. Four-dimensional numerical modeling of crustal growth at active continental margins. *Journal of Geophysical Research: Solid Earth*, 118(9):4682–4698, 2013.

Chapter 5

Evolution of TTG source regions in plume-lid tectonics¹

Abstract

Geological-geochemical evidence points towards higher mantle potential temperature and a different type of tectonics, known as plume-lid tectonics, in the early Earth. In order to investigate tectono-magmatic processes associated with plume-lid tectonics and felsic TTG-like crust formation, we conduct a series of 3D high-resolution magmatic-thermomechanical models. The numerical experiments show two distinct phases in coupled crust-mantle evolution: a long quiet growth phase followed by a short catastrophic overturn phase. Results of the detailed model analysis presented here suggest that TTGs mainly form during the overturn event. We therefore conclude that TTGs are produced in pulses of ~ 100 Myr.

5.1 Introduction

The present-day crust of the Earth follows a bimodal distribution in both compositional and spatial domain. 41% of the surface area consists of continental crust which has a surface elevation slightly above sea level and an average thickness of 35–40 km (Cawood et al., 2013, and references therein). Evidence from both geological and geophysical data reveal that the continental crust is typically three-layered with a felsic upper crust formed of sediments and granites, a middle crust consisting mainly of gneisses at amphibolite to granulite facies and a lower crust at granulite facies with basic intrusive rocks (Cawood et al., 2013, and references therein). The bulk composition of the crust is andesitic.

A similar bimodal distribution at least in composition can also be observed for Archean crust. Archean granite-greenstone terrains show two different types of crust. One more mafic crustal rock type is forming winding belts of greenstone composition; the other

¹This material is unpublished as of yet

more felsic type is found in upwelling domes of TTG. The timing and mechanism of the formation of felsic crust is still a highly debated and controversial topic. Generally two stages of differentiation are invoked regarding the formation of felsic crust. In a first stage, extraction of basaltic magma from the mantle, melting of the ultramafic peridotitic mantle material leads to the formation of a less mafic melt with higher SiO_2 content, lower MgO values, and lower Mg\# (where $\text{Mg\#} = \text{Mg}/(\text{Mg} + \text{Fe})$) (Lee et al., 2011; Hawkesworth and Kemp, 2006). The remaining depleted residue has a lower SiO_2 content, higher MgO values, and higher Mg\# (Lee et al., 2011). Felsic crust is formed from this early basaltic crust by remelting or fractional crystallisation, possibly augmented by sedimentary processes (Hawkesworth and Kemp, 2006). Moyen (2011) shows that TTGs fall into three different categories according to the PT-conditions of their source magma. He categorises them into high-, medium- and low-pressure TTGs, where the high-pressure group is marked by higher values for SiO_2 and Al_2O_3 and lower values for MgO as well as a lower Mg\# . The low-pressure group shows opposite features while the medium-pressure group shows values in-between. From an extensive database of 1700 samples 75% were identified to be TTGs and within these TTG samples the percentage of high- to medium- to low-pressure samples was found to be 20% to 60% to 20% (Moyen, 2011).

5.2 Methods

In order to better understand the formation of felsic TTG-like crust in the early Earth regime of plume-lid tectonics as proposed by Fischer and Gerya (in press); Sizova et al. (2015); Gerya et al. (2015), we perform a detailed analysis of our 3D high-resolution magmatic-thermomechanical models discussed in Chapter 4.

According to Moyen (2011) source melt of TTGs is formed under certain favourable conditions which can be grouped into three distinct PT-windows (see Fig. 5.1):

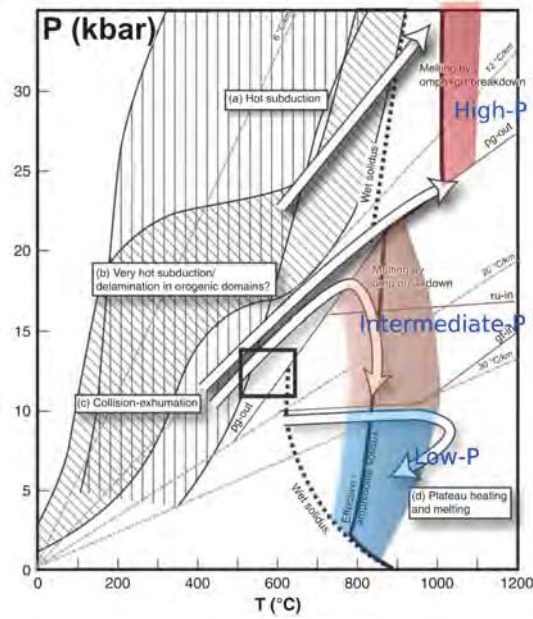


Figure 5.1: PT-conditions for formation of source melts of low-, medium- and high-pressure TTGs. Figure modified from Moyen (2011, Fig. 12)

$$LP(P, T) = \begin{cases} T \geq 760.0 + 273.15 - 60.0 \cdot \left(\frac{P - 1e9}{1e9} \right)^2 \\ T \leq 1000.0 + 273.15 - 150.0 \cdot \left(\frac{P - 1.2e9}{1.2e9} \right)^2 \\ P \geq -5e8 \cdot \frac{T - (870.0 + 273.15)}{220.0} \\ P < 1e9 \end{cases} \quad (5.1)$$

$$MP(P, T) = \begin{cases} T \geq 760.0 + 273.15 - 60.0 \cdot \left(\frac{P - 1e9}{1e9} \right)^2 \\ T \leq 1000.0 + 273.15 - 150.0 \cdot \left(\frac{P - 1.2e9}{1.2e9} \right)^2 \\ P \geq 1e9 \\ P \leq 1.5e9 + 7e8 \cdot \frac{T - (700.0 + 273.15)}{200.0} \end{cases} \quad (5.2)$$

$$HP(P,T) = \begin{cases} T \geq 1000.0 + 273.15 \\ T \leq 1100.0 + 273.15 + 50.0 \cdot \left(\frac{P - 3.5e9}{3.5e9} \right) \\ P \geq 2.35e9 + 1.5e8 \cdot \frac{T - (1000.0 + 273.15)}{100.0} \\ P \leq 5e9 \end{cases} \quad (5.3)$$

These three pressure groups form a continuous evolution from high to low pressure, which is mainly visible in the HREE contents but also in the change of MgO content from lower to higher values (Moyen, 2011).

The 3D numerical magmatic-thermomechanical I3ELVIS code (Gerya and Yuen, 2007) as used in Chapter 4 does not support self-consistent formation of felsic TTG crust. Though by taking into account the PT-regions for high-, medium- and low-pressure TTG source melt, the potential for the formation of new TTG crust can be assessed. Only partial melt from hydrated mafic (basaltic) crust which is found within one of the three distinct PT-windows is taken into account for the formation of high- (HP, Eq. (5.3)), medium- (MP, Eq. (5.2)) or low-pressure (LP, Eq. (5.1)) TTG crust respectively.

5.3 Results and discussion

5.3.1 Occurrence of mafic hydrated partial melt and TTG source regions

All mafic rock types which follow basaltic (Eq. (2.8)) or gabbroic (Eq. (2.9)) melting rules (see Table 4.1) are considered to form hydrated partially molten mafic crust which can potentially produce TTG-like melts. The initial temperature conditions in the mantle are high enough to form a thick sublithospheric layer of partially molten mantle. To not yield any unrealistic results, this initial partially molten mantle layer is ‘pre-depleted’ and its melt fraction is decreased to the minimum of $M_{min} = 2\%$. Any further increase in the mantle-derived melt volume and in the related partially molten hydrated crust volume (Fig. 5.2) must arise from model dynamics. As can be seen from Fig. 4.14, the reference model *B100b* shows a peak in the volume of partially molten hydrated mafic crust after 2–3 Myr (Fig. 5.2b) which results from the ascending plume

initiated by the initial thermal perturbation. Within the next 15 Myr the volume of hydrated partially molten mafic crust decreases again and at 20 Myr stabilises at a low value (Fig. 5.2a). For the next 60 Myr no new hydrated mafic partially molten crust is formed. At 80 Myr the total volume of mafic hydrated partially molten crust strongly increases and stabilises at a high value for the rest of the model run. The evolution of the total volume of mafic hydrated partially molten crust in models *D100b* and *D0b* closely follows the reference model, while model *E100b* shows no initial peak but a continuous growth in the total mafic hydrated partial melt volume.

Mafic hydrated partially molten crust which occurs within any of the defined PT-windows is assumed to act as a source region for potential TTG melt. The occurrence of TTG source regions for the reference model *B100b* closely follows the volume of mafic hydrated partially molten crust. Generally $\sim 30\%$ of the total volume of mafic hydrated partially molten crust falls into the category of TTG source regions, except for the initial melting pulse in the beginning of the model (Fig. 4.14).

Evolution for the TTG source regions for models *D100b* and *D0b* is again very similar to the reference model. However, as both model runs are stopped shortly after the strong melting pulse at 80 Myr, almost no (*D100b*) to no TTG source regions are formed. $\sim 30\%$ of the mafic hydrated partially molten crust in model *E100b* falls into the defined PT-windows. The evolution of the TTG source regions volume for model *E100b* therefore shows continuous growth.

5.3.2 Distribution of TTG source regions into distinct PT-windows

In Fig. 5.3 the total volume of available TTG source regions as displayed in Fig. 5.2 by dashed lines is scaled to 100% for each timestep. The percentage of TTG source regions falling into HP, MP or LP windows is shown for each timestep, indicated by a solid line for the percentage of HP TTG source regions and a dashed line for the sum of HP and MP TTG source regions.

Generally LP and MP TTG source regions are much more abundant than HP TTG source regions. In the reference model *B100b*, no HP TTG source regions are observed in the beginning of the model and percentages between MP and LP source regions vary strongly within the first 20 Myr (Fig. 5.4a). Within the next 60 Myr relative proportions of the MP TTG source regions are increasing up to 100%. At 80 Myr a

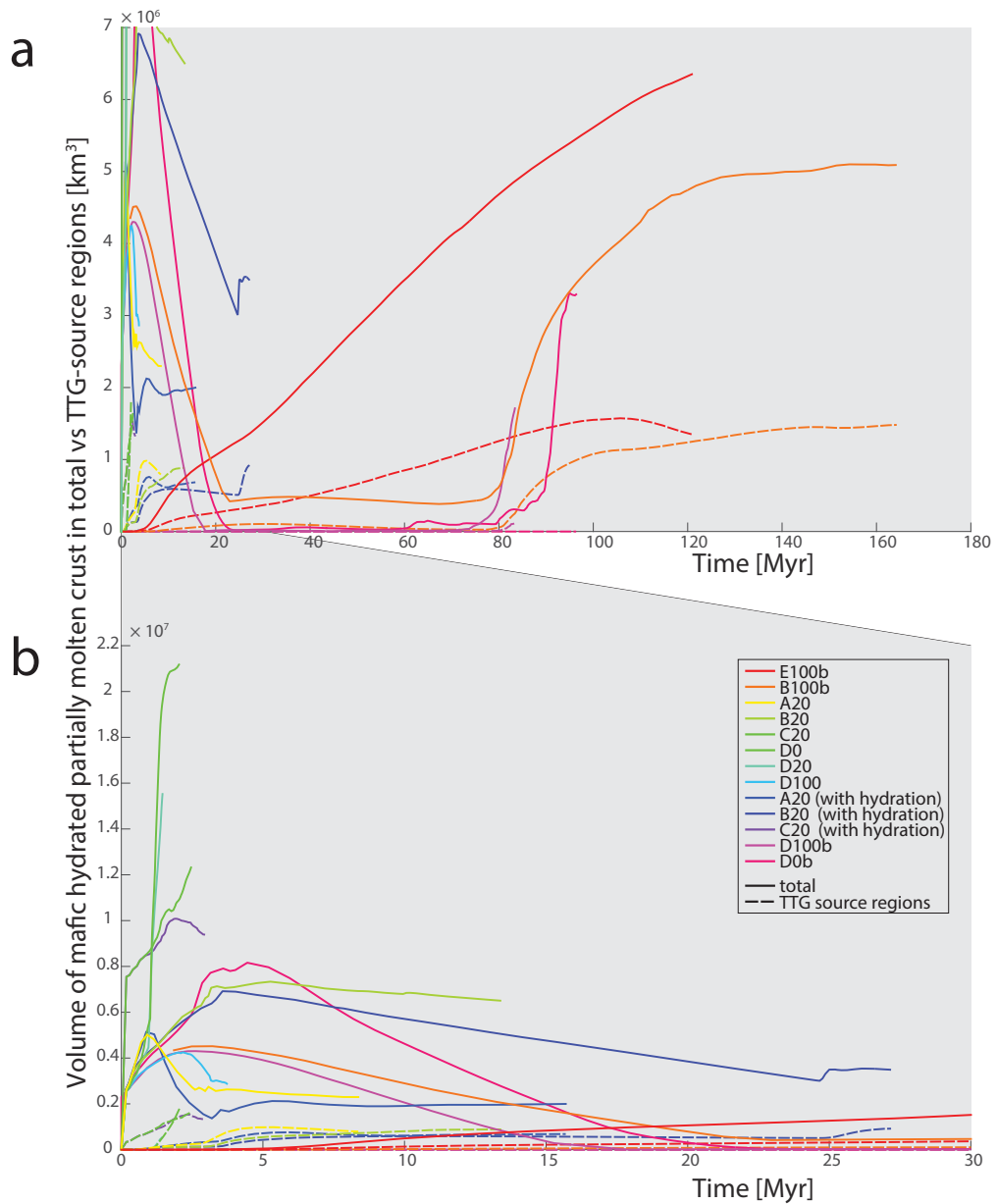


Figure 5.2: (a) The total volume of partially molten hydrated mafic crust over time is shown in solid lines for each model given in Table 4.2. The dashed lines indicate the volume of partially molten hydrated mafic crust which falls in any of the defined PT-categories and is therefore equal to the volume of TTG source regions. (b) A zoom-in of the first 30 Myr of model development is shown.

dominant peak can be observed where both HP and LP TTG source regions increase rapidly to a percentage of 5% HP, 70% MP and 25% LP TTG source regions. After this short episode (~ 10 Myr) of strong variation, the percentage of HP TTG source regions

goes back to 0% while the percentage of LP TTG source regions slowly increases and finally stabilises at a value of $\sim 40\%$.

In model *D100b* no TTG source regions are available for most of the time. Otherwise it shows mainly 100% MP TTG source regions. However, for a short peak of 10 Myr close to 80 Myr a strong increase in HP and LP TTG source regions can be observed which leads to a percentage of 20% HP, 50% MP and 30% LP TTG source regions (Fig. 5.4b). Model *E100b* again shows mainly MP TTG source regions and no HP TTG source regions at all. In the first 20 Myr of model development there is a peak in LP TTG source regions at 30%. This value stabilises later at 10% (Fig. 5.4c). Nothing can be said about model *D0b* as no mafic hydrated partially molten crust is found in any of the defined PT-windows.

5.3.3 Interpretation of TTG source region development with regard to geodynamic model development

No TTG source regions are formed during the first plume upwelling triggered by the initial thermal perturbation prescribed at the model bottom (Fig. 4.1a). The following period of inactivity between 20 – 80 Myr falls together with a tectonically quiet period of strong crustal and lithospheric growth (Figs. 4.6b to 4.6d). Newly formed mafic volcanic crust sinks through the felsic upper crust only to be halted at the depth of neutral buoyancy in the middle crust, where it forms a small but slowly growing reservoir of TTG source regions which mainly adds to the LP TTG source regions. This long growth phase is terminated by a catastrophic overturn event. The overturn event takes ~ 10 Myr and peaks at 80 Myr. Increasingly more frequent eclogite drips combine to a linear curtain which starts delamination of the lithosphere and lower crust (Figs. 4.6e and 4.6f). Mafic lower crust is now in direct contact with the hot mantle and able to form the LP TTG source regions peak. The delaminating cold lithosphere also strengthens mantle convection and sublithospheric small-scale convection which increases formation of partial melt. Melting of the delaminating crust in greater depth is able to produce HP TTG source regions. After the catastrophic overturn event, further sinking of mafic crust continuously replenishes the lost lower mafic crust forming a new partially molten mafic lower crust and TTG source regions percentages return to the values found before the overturn event.

Model *D100b* has a single mafic layer as initial condition. When compared to the reference model *B100b*, newly formed mafic volcanic rocks don't sink but stay at the surface and no midcrustal melt-layer is formed (Fig. 4.2a). The consequence is no partial melt formation in the initial stages of the model. Further model development, however, is very similar to the reference model. In a quiet growth phase the crust is thickening (Figs. 4.2b to 4.2d) until it becomes unstable and delaminates in a catastrophic overturn event (Figs. 4.2e and 4.2f). This overturn event triggers formation of additional HP and LP TTG source regions leading to a percentage of 20% HP, 50% MP and 30% LP TTG source regions.

Model *E100b* initially has a single felsic layer. As already discussed for the reference model *B100b*, newly formed mafic crust sinks through the felsic crust and forms a reservoir of partial melt at the depth of neutral buoyancy (Figs. 4.5a and 4.5b). As this model consists of a single layer of felsic crust, neutral buoyancy depth is deeper than in the reference model and percentages of TTG source regions of model *E100b* compared to model *D100b* are shifted towards MP TTG source regions for the first 50 Myr. But as the whole crust consists of low density felsic material, the underplating mafic rocks do not reach eclogite transformation depth, no drips or delamination of crustal material into the mantle are observed and no overturn event takes place (Fig. 4.5). Consequently, a characteristic spike in HP and LP TTG source regions at 80 Myr, as it can be observed for the two models with pure mafic crust (*D100b*) and lower mafic crust (*B100b*), does not exist.

Model *D0b* has the same model setup as *D100b* consisting of a single mafic layer as the initial condition. However, compared to the other models discussed, magmatism is purely plutonic. The curve for the volume of total mafic hydrated partially molten crust is very similar to the other two models with a mafic crust. The initial melting pulse is related to the initial mantle plume initiated by the initial thermal perturbation and no TTG source regions are formed at this stage. Between 20 – 80 Myr the model exhibits a quiet growth phase where almost no mafic hydrated partially molten crust is formed at all (Figs. 4.3b to 4.3e). A strong increase in mafic hydrated partially molten crust volume at 80 Myr indicates the end of the quiet growth phase (Figs. 4.3f and 4.3g). The plutonic crust formation mechanism leads to the formation of deep-seated plutonic intrusions which are able to start crustal and lithospheric overturn (Figs. 4.3f and 4.3g). However, these deep-seated reservoirs of hydrated partially molten mafic crust do not fall into any of the defined PT-categories for TTG source regions.

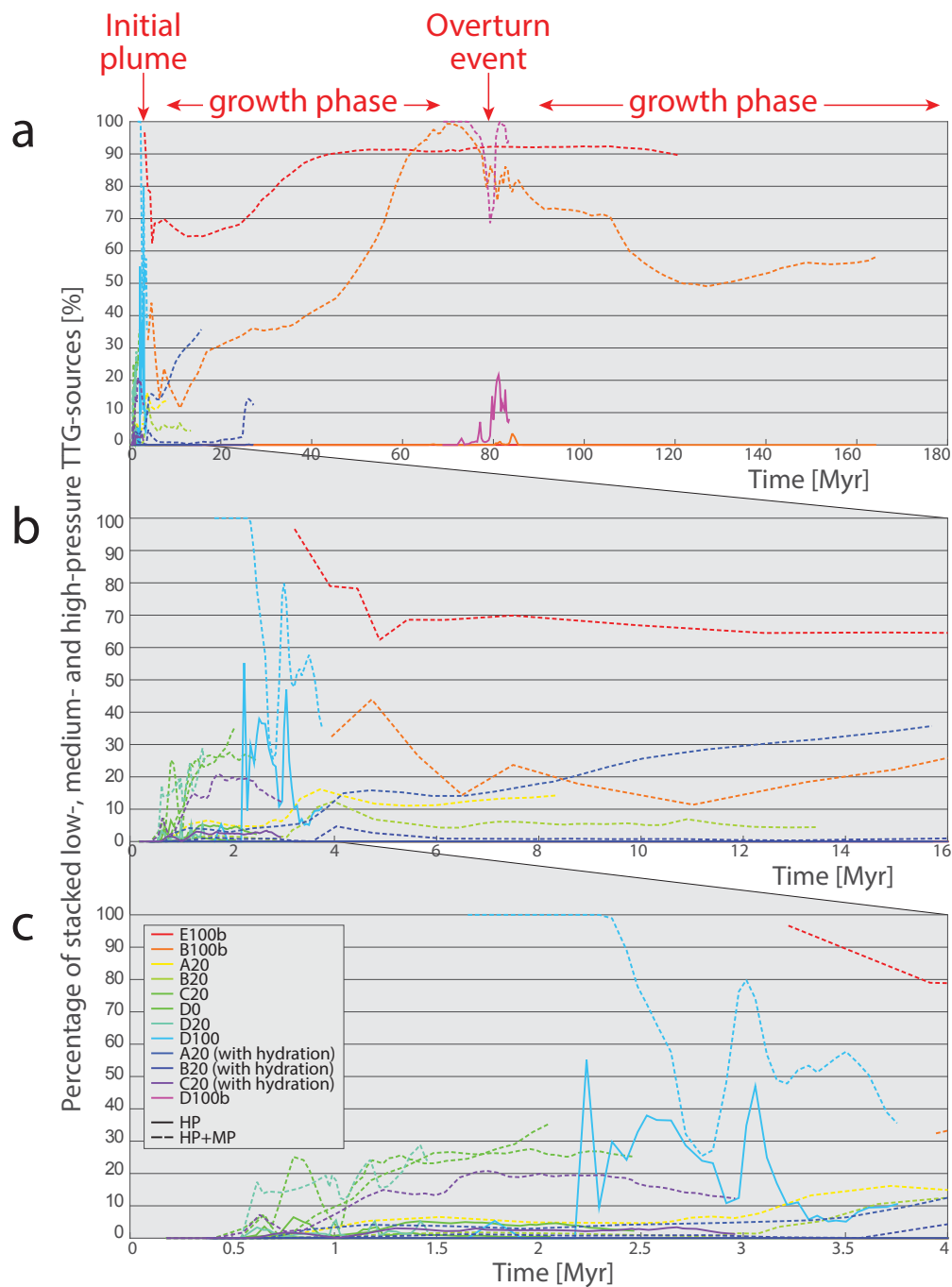


Figure 5.3: (a) The stacked percentages of high- to medium- to low-pressure TTG source regions are shown over time for each model given in Table 4.2. The solid line indicates the percentage of high-pressure TTG source regions while the dashed line indicates the percentage of the sum of medium- and high-pressure TTG source regions. (b) A zoom-in of the first 16 Myr of model development is shown. (c) A zoom-in of the first 4 Myr of model development is shown.

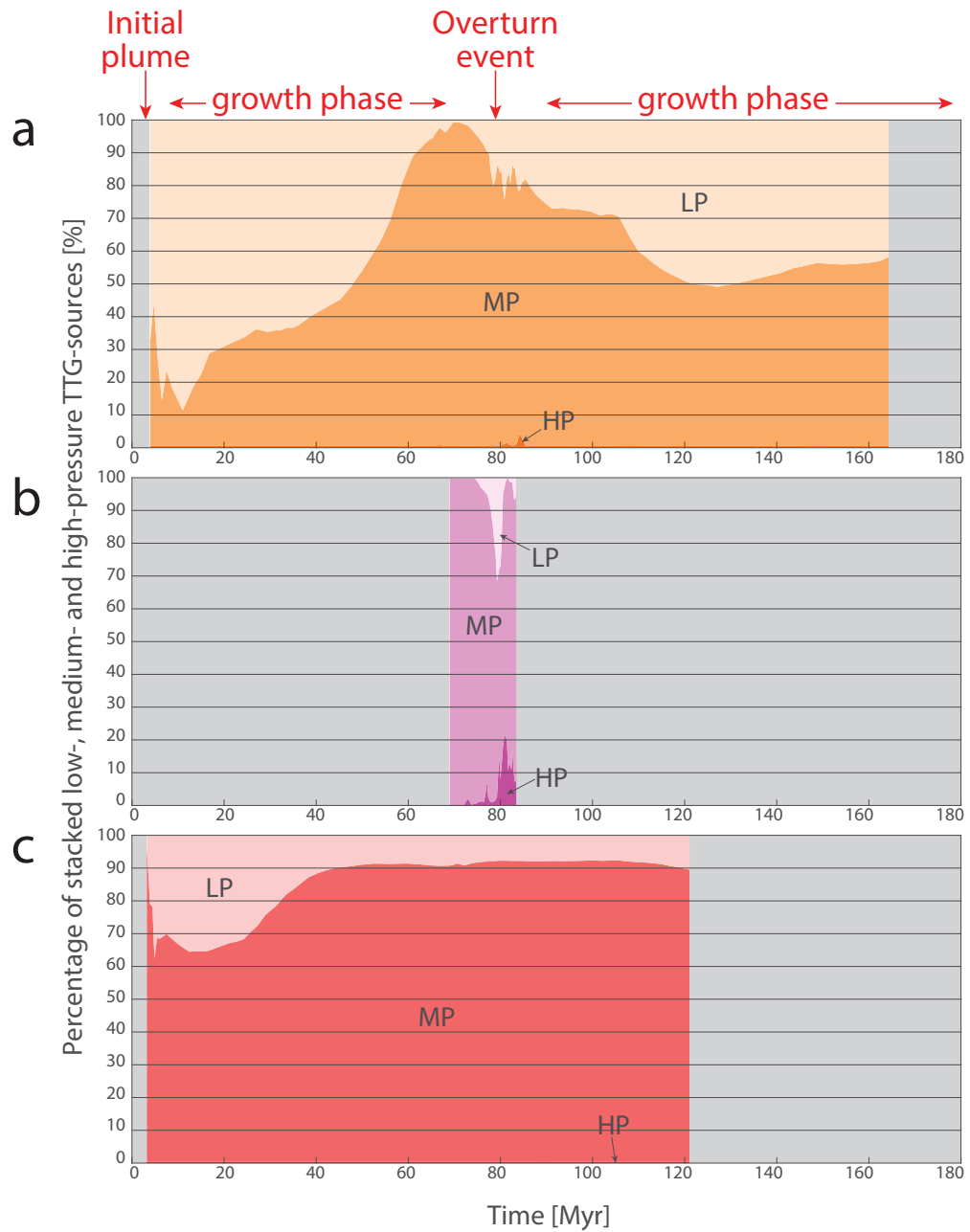


Figure 5.4: The stacked percentages of high- to medium- to low-pressure TTG source regions over time are shown separately for each reference model: (a) *B100b*, (b) *D100b* and (c) *E100b*. See Fig. 5.3 for details. Data is only available when partially molten hydrated mafic crust is found in any of the defined TTG source regions (see dashed line in Fig. 5.2).

5.4 Conclusion

In conclusion we can say that both the available volume of potential TTG source regions as well as its distribution into low-, medium- and high-pressure regions varies strongly during an active plume-lid tectonics cycle of a long quiet growth phase followed by a short catastrophic overturn phase (see Chapter 4). The percentage of LP/MP/HP TTG source regions during the growth phase mainly depends on the initial crustal composition and ranges from 0 – 70% LP and 100 – 30% MP TTG source regions while no HP TTG source regions are present.

During an overturn event, the available volume of potential TTG source regions is strongly increased and at least for models with mafic crust the percentages of LP/MP/HP TTG source regions come close to the values measured by Moyen (2011) with 20% HP, 60% MP and 20% LP TTGs. The occurrence of a strong increase in the volume of potential TTG source regions at 80 Myr and later stabilisation at a higher level (Fig. 5.2a) together with the conspicuous peaks in percentage of LP/MP/HP TTG source regions at the same time could be an indication that this signal will then be preferentially found in TTG rocks.

We suggest that the TTGs in Archean granite-greenstone terrains with their typical dome-and-keel structure might have developed during the short ~ 10 Myr bursts of the overturn phase of the plume-lid tectonics cycle and conclude that TTGs form in pulses of ~ 100 Myr.

References

- P. Cawood, C. Hawkesworth, and B. Dhuime. The continental record and the generation of continental crust. *Geological Society of America Bulletin*, 125(1-2):14–32, 2013.
- R. Fischer and T. Gerya. Early Earth plume tectonics: A high-resolution 3D numerical modelling approach. *Journal of Geodynamics*, in press.
- T. V. Gerya and D. A. Yuen. Robust characteristics method for modelling multiphase visco-elasto-plastic thermo-mechanical problems. *Physics of the Earth and Planetary Interiors*, 163(1-4):83–105, 2007.

- T. V. Gerya, R. J. Stern, M. Baes, S. V. Sobolev, and S. A. Whattam. Plate tectonics on the Earth triggered by plume-induced subduction initiation. *Nature*, 527(7577): 221–225, 2015.
- C. Hawkesworth and A. Kemp. Evolution of the continental crust. *Nature*, 443(7113): 811–817, 2006.
- C.-T. A. Lee, P. Luffi, and E. J. Chin. Building and destroying continental mantle. *Annual Review of Earth and Planetary Sciences*, 39:59–90, 2011.
- J.-F. Moyen. The composite Archaean grey gneisses: Petrological significance, and evidence for a non-unique tectonic setting for Archaean crustal growth. *Lithos*, 123 (1–4):21–36, 2011.
- E. Sizova, T. Gerya, K. Stüwe, and M. Brown. Generation of felsic crust in the Archean: A geodynamic modeling perspective. *Precambrian Research*, 271:198–224, 2015.

Chapter 6

Conclusion and outlook

The main objective of this thesis was to understand and describe the style of tectonics at work during the early Earth, mainly the Archean, and comprehend how tectonics evolved through Earth history up to the system of plate tectonics we find in present-day Earth. This goal was achieved by means of high-resolution 3D magmatic-thermomechanical numerical models at varying mantle potential temperatures. The following chapter gives a summary of the most significant achievements of this work and discusses possible areas of future research.

6.1 Main achievements

Geological-geochemical evidence points towards higher mantle potential temperature and a different type of tectonics in the early Earth compared to the present day. We investigated the variation in tectonic style for oceanic plate subduction under an active continental margin by varying mantle potential temperature T_p ($\Delta T_p = 0 - 250$ K, compared to present-day conditions). Results of numerical experiments correspond to modern-style subduction at present-day mantle temperatures ($\Delta T_p = 0$ K), whereas at higher temperature conditions, important systematic changes in the style of both lithospheric deformation and mantle convection occur. For $\Delta T_p = 50 - 100$ K a regime of dripping subduction emerges which is still very similar to present-day subduction but is characterised by frequent dripping from the slab tip and a loss of coherence of the slab, suggesting a close relationship between dripping subduction and episodic subduction. At further increasing $\Delta T_p = 150 - 200$ K dripping subduction is observed together with unstable dripping lithosphere which corresponds to a transitional regime. For $\Delta T_p = 250$ K, presumably equivalent to early Archean, the dominating tectonic style is characterised by small-scale mantle convection, unstable dripping lithosphere, thick basaltic crust and small plates. Even though the initial setup is still defined by present-day subduction, this final regime shows many characteristics of plume-lid tectonics. Transition between the two end-members, plume-lid tectonics and plate tectonics, occurs gradually, and at intermediate temperatures elements of both tectonic regimes are present. We conclude that tectonics, starting out from plume-lid tectonics,

evolved gradually into what we can observe today as plate tectonics and subduction. Therefore an abrupt geodynamic regime transition point can probably not be specified.

The plume-lid tectonics regime is characterised by predominantly tectono-magmatic processes and mainly driven by strong crustal growth. To examine the proposed plume-lid tectonics regime further, a new numerical model setup was devised without any external plate tectonic forces to isolate 3D effects of various plume-lithosphere and crust-mantle interactions. Results of the numerical experiments show that overthickened unstable crust is removed by means of eclogite drips or drip tectonics (Herzberg, 2014) and delamination. On the one hand, asthenospheric mantle flow drives crustal growth, deformation and episodic thinning by eclogite recycling and, on the other hand, it is strongly modified by the dripping of crustal material back into the mantle. We also found that the crust forms a separate convection layer with convection being assisted by the doming of plutonic magma and the sinking of basaltic crust formed by flood volcanism (Van Kranendonk, 2011; Arndt, 1999). This yields an extremely efficient way of heat removal through the crust via convection and conduction through the thinned brittle upper crustal lid and could provide an answer to the Archean paradox as described by Moresi (2013) in addition to the heat-pipe model (Moore and Webb, 2013). In conclusion we found that plume-lid tectonics shows two distinct phases in coupled crust-mantle evolution: (1) A long (80–100 Myr) and relatively quiet ‘growth phase’ which is marked by growth of crust and lithosphere, followed by (2) a short (~ 20 Myr) and catastrophic ‘removal phase’ where unstable parts of the crust and mantle lithosphere are removed by eclogitic dripping and later delamination, forming a pattern of episodic overturn as has already been suggested for the Archean by several authors: Kröner and Layer (1992); Zegers and van Keken (2001); Bédard (2006); van Thienen et al. (2005).

Detailed analysis of the plume-lid tectonics models studied allows a conclusion to be drawn concerning the potential of formation of different types of TTGs. We have assessed the potential source regions of low-, medium- and high-pressure TTGs according to their PT-conditions, assuming mafic hydrated partial melt as source melt. Results of the detailed model analysis suggest that TTGs mainly form during the overturn event and values for percentages of source regions come close to natural values measured by Moyen (2011). We therefore conclude that TTGs are produced in a plume-lid tectonics setup during the short (10 Myr) overturn phases and in pulses of ~ 100 Myr.

6.2 Areas of future research

6.2.1 Implementation of felsic crust formation in I3ELVIS

The formation mechanism of original continental crust from mafic crust and mantle material is still unclear. Possible crust formation mechanisms include multiple remelting or fractional crystallisation of mafic crust, potentially enhanced by sedimentary processes (Hawkesworth and Kemp, 2006). The records of preserved Archean or Hadean crust are very sparse. The oldest isotopically dated rocks on Earth are the Acasta gneisses of Northwest Canada which mainly consist of highly deformed TTGs and are about 4.0 Ga old (Condie, 2005). The oldest minerals found are detrital zircons with an age of 4.0 Ga. However, fractions of these zircons show ages of up to 4.4 Ga which indicates the presence of felsic crust at this very early time (Condie, 2005). As both the method for felsic crust formation as well as the early Earth tectonic regime are still under debate, it is clear that many different mechanisms and different growth paths for the volume of continental crust have been proposed by various authors (see Condie, 2005, and references therein).

In Chapter 5 the possibility of TTG formation is discussed by assessing the potential of mafic hydrated partial melt to form TTG source melt. Even though this study gave interesting insights into the felsic crust formation process, it has several drawbacks: Potential regions of TTG source melt are identified, but no felsic crust is formed. Further model development therefore continues with no felsic crust or with the fixed volume of felsic crust given as the initial condition. However, the presence of felsic crust is an important element in the plume-lid tectonics regime described (Section 4.3.3). Formation of felsic crust is, therefore, an important feature to add.

Formation of felsic crust has already been added to the 2D version, I2ELVIS, of this code (Gerya and Yuen, 2003). Sizova et al. (2015) devised a numerical system which reproduces the process of remelting and fractional crystallisation for the production of felsic crust (see Fig. 6.1). Melt is extracted from melt-bearing mantle peridotite and deposited as either volcanic or plutonic basalt. The melt-bearing basaltic crust can then form dacitic (felsic) crust.

Implementation of this method suggested by Sizova et al. (2015) into the 3D code I3ELVIS will not be without problems. The code used in the plume-lid tectonics setup

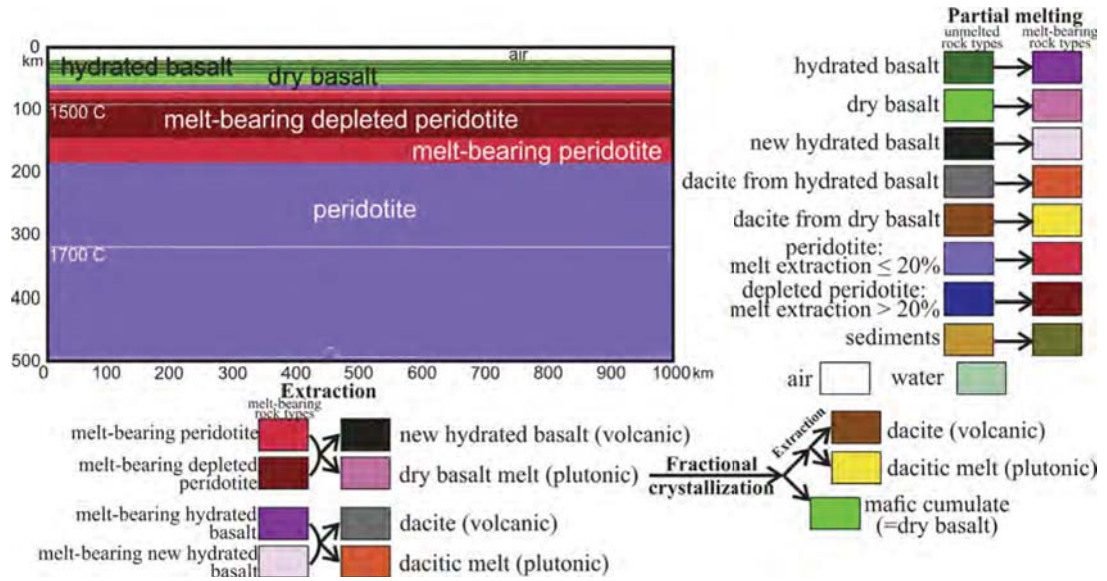


Figure 6.1: Implementation of felsic crust formation in I2ELVIS (Sizova et al., 2015).

as described in Section 4.2 is highly computationally expensive. The large amounts of melt produced as well as the high velocities and sharp viscosity contrasts lead to very small timesteps of < 100 yr. To observe overturn events of the plume-lid tectonics regime after > 80 Myr, compute times of > 12 months are necessary. Implementation of felsic crust formation will not only further increase the compute time, but also the size of the original data files. Model data is stored in binary files, one for each timestep, ranging in size from 6 – 9 GB for model resolutions as described in Section 4.2. For each melt extraction process, additional new markers are created and the data file consequently grows in size rapidly. This does not pose such an avid problem in the 2D case where the data files are smaller to begin with, due to smaller node numbers.

To make implementation of felsic crust formation possible, it might be necessary to add additional code speed-up routines. For example one could think about adding a ‘marker thinning routine’ similar in idea to adaptive mesh refinement. When a predefined property (carried by markers) over a group of markers only varies within a certain threshold, this group is replaced by one marker.

6.2.2 Outlook II: Refertilisation of depleted mantle by delamination of eclogite

The concept of plume-lid tectonics and felsic crust formation as discussed in Chapters 4 and 5 is also promoted and investigated in detail by Bédard (2006) from a geochemical perspective (see also Bédard, 2003; Bédard et al., 2013; Bédard and Harris, 2014; Harris and Bédard, 2014, 2015). Bédard (2006) shows that lower crustal anatexis of the dominant mafic lithology, tholeiitic metabasalt, in the Minto Block (northeastern Superior Province, Canada) leads to the formation of felsic tonalite-trondhjemite (TT) magma and a garnet-eclogite restite (see Fig. 6.2a). Bédard (2006) then speculates that the thick layer of restite which is formed will delaminate back into the depleted mantle (Fig. 6.2b). Mixing of delaminating eclogitic restite and depleted mantle material will lead to a refertilisation of the latter and allow further melt extraction (Fig. 6.2c) which in turn triggers further eclogite delamination (Fig. 6.2d, Bédard (2006)).

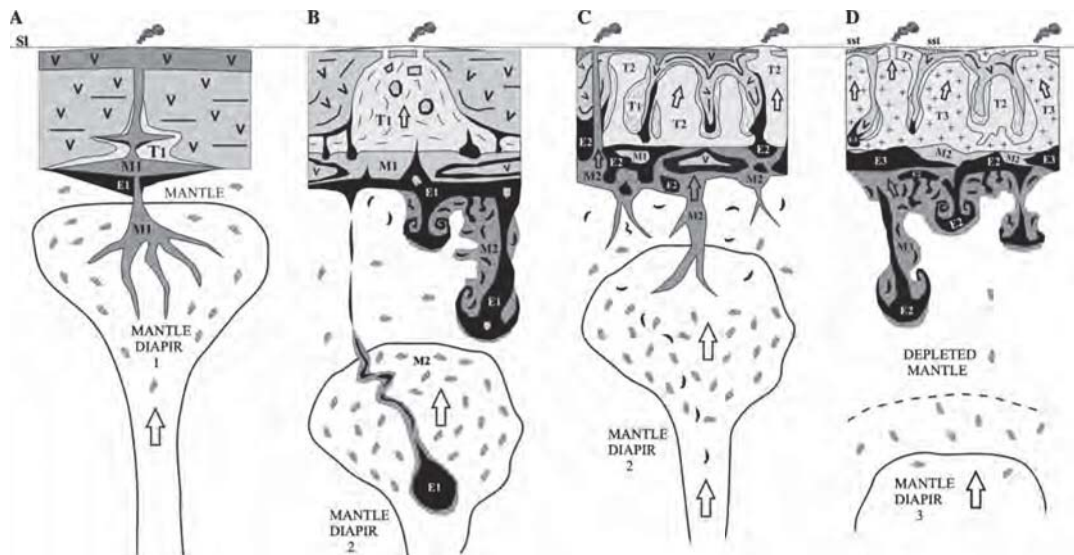


Figure 6.2: (a) Melt (M1) from a mantle plume produces a thick mafic crust. Further heating from the plume causes remelting of the mafic crust and differentiation into a felsic magma (T1) and an eclogitic restite (E1). (b) Delamination and mixing of the restite (E1) triggers additional melting of the mantle (M2). (c)-(d) More volcanic crust and eclogitic restite is produced which triggers again further mantle melting. Figure from Bédard (2006).

The plume-lid tectonics regime is mainly driven by tectono-magmatic processes. Several mechanisms as discussed by Bédard (2006) are already implemented in the current version of I3ELVIS. However, felsic crust formation (Section 6.2.1) and mantle refertilisation provide an important addition. The most simple option would be to only

implement mantle refertilisation by eclogite addition which would not necessarily require formation of new markers (see discussion Section 6.2.1). Instead the presence of eclogite in depleted mantle peridotite could lead to a decrease in the accumulated amount of extracted melt $\sum_n M_{ext}$, which is basically the opposite process to melt extraction as described in Section 2.6, and finally to the consumption of the eclogite.

6.2.3 Outlook III: Long-term global models

The final goal would be to model the proposed type of plume-lid tectonics in a 3D spherical shell. The minimum requirements would include the processes outlined in Chapter 2, basically including melting, depletion of mantle material, formation of basaltic crust and the eclogite phase transition. A ‘short-term’ global model would require an expected model run time of ≥ 80 Myr to investigate dynamics of crustal and lithospheric growth and catastrophic overturn. In this scenario felsic crust could be part of the initial model setup but felsic crust formation is not strictly necessary. The final goal, however, would be to model the ‘long-term’ evolution of plume-lid tectonics and hopefully be able to observe several overturn events. Interesting new questions will concern the formation of continental nuclei and the mechanism of continental growth. In this type of model setup, formation of felsic crust and probably also refertilisation of depleted mantle by delamination of eclogite are necessary mechanisms. In addition, enrichment of radiogenic material in the crust as well as a decrease in radiogenic heating over time should be taken into account.

References

- N. Arndt. Why was flood volcanism on submerged continental platforms so common in the Precambrian? *Precambrian Research*, 97(3–4):155–164, 1999.
- J. H. Bédard. Evidence for Regional-Scale, Pluton-Driven, High-Grade Metamorphism in the Archaean Minto Block, Northern Superior Province, Canada. *The Journal of Geology*, 111(2):183–205, 2003.
- J. H. Bédard. A catalytic delamination-driven model for coupled genesis of Archaean crust and sub-continental lithospheric mantle. *Geochimica et Cosmochimica Acta*, 70(5):1188–1214, 2006.

- J. H. Bédard and L. B. Harris. Neoproterozoic disaggregation and reassembly of the Superior craton. *Geology*, 42(11):951–954, 2014.
- J. H. Bédard, L. B. Harris, and P. C. Thurston. The hunting of the snArc. *Precambrian Research*, 229(0):20–48, 2013.
- K. C. Condie. 8 - Crustal and Mantle Evolution. In *Earth as an Evolving Planetary System*, pages 265–VI. Academic Press, Burlington, 2005.
- T. V. Gerya and D. A. Yuen. Characteristics-based marker-in-cell method with conservative finite-differences schemes for modeling geological flows with strongly variable transport properties. *Physics of the Earth and Planetary Interiors*, 140(4):293–318, 2003.
- L. B. Harris and J. H. Bédard. Crustal evolution and deformation in a non-plate-tectonic Archaean Earth: Comparisons with Venus. In *Evolution of Archaean Crust and Early Life*, pages 215–291. Springer, 2014.
- L. B. Harris and J. H. Bédard. Interactions between continent-like ‘drift’, rifting and mantle flow on Venus: gravity interpretations and Earth analogues. *Geological Society, London, Special Publications*, 401(1):327–356, 2015.
- C. Hawkesworth and A. Kemp. Evolution of the continental crust. *Nature*, 443(7113):811–817, 2006.
- C. Herzberg. Early Earth: Archaean drips. *Nature Geoscience*, 7(1):7–8, 2014.
- A. Kröner and P. W. Layer. Crust Formation and Plate Motion in the Early Archaean. *Science*, 256(5062):1405–1411, 1992.
- W. B. Moore and A. A. G. Webb. Heat-pipe Earth. *Nature*, 501(7468):501–505, 2013.
- L. Moresi. Earth science: A resolution of the Archaean paradox. *Nature*, 501(7468):496–497, 2013.
- J.-F. Moyen. The composite Archaean grey gneisses: Petrological significance, and evidence for a non-unique tectonic setting for Archaean crustal growth. *Lithos*, 123(1–4):21–36, 2011.
- E. Sizova, T. Gerya, K. Stüwe, and M. Brown. Generation of felsic crust in the Archaean: A geodynamic modeling perspective. *Precambrian Research*, 271:198–224, 2015.

- M. J. Van Kranendonk. Cool greenstone drips and the role of partial convective overturn in Barberton greenstone belt evolution. *Journal of African Earth Sciences*, 60(5):346–352, 2011.
- P. van Thienen, N. J. Vlaar, and A. P. van den Berg. Assessment of the cooling capacity of plate tectonics and flood volcanism in the evolution of Earth, Mars and Venus. *Physics of the Earth and Planetary Interiors*, 150(4):287–315, 2005.
- T. E. Zegers and P. E. van Keken. Middle Archean continent formation by crustal delamination. *Geology*, 29(12):1083–1086, 2001.

Acknowledgements

This thesis was been completed with the contribution and help of many people; I would like to thank them and express my gratitude.

First and foremost, I would like to express my sincere gratitude to my supervisor, Prof. Dr. Taras Gerya. It was his lecture in numerical modelling that I attended during my master's degree at ETH which piqued my interest in modelling and geodynamics. Therefore, I was very pleased not only to be able to complete my master's thesis under his supervision but also my PhD studies. During my time here at ETH I benefited very much from his broad experience, continuous supervision, helpful advice and great enthusiasm for science. I would like to thank him for introducing me to the world of geodynamics and numerical modelling and for many discussions over a good cup of tea.

I am very grateful to Prof. Dr. Paul Tackley for giving me the opportunity to work in the GFD group as a PhD student and to participate in seminars and conferences all over the world. His lecture, 'Numerical modelling in Fortran' was one of my highlights during my master's at ETH. I would also like to thank him for agreeing to examine my work.

I would also like to thank Dr. Jeroen van Hunen for agreeing to examine my defence and reviewing this thesis and I would like to extend my gratitude to him for a very detailed review of my first paper.

In late summer 2014, I had the opportunity to visit and study an Archean craton. I am very grateful to Prof. Dr. Alfred Kröner for organising the geological excursion to the Barberton greenstone belt. I would also like to thank Prof. Dr. Dirk van Reenen for organising a field trip to the Limpopo belt.

During my PhD I had the chance to work with many great people in the GFD group and I would like to thank them all. But in particular I would like to thank Prof. Dr. Gregor Golabek who helped to get me started with the I3ELVIS code and patiently explained all its quirks to me.

And of course I thank my family who always supported me with great patience. I thank my mother for long hikes and discussion in the Alps which piqued my interest

in all things related to the Earth and its curious workings. And I thank my father for dropping that folder at my desk and making me learn DataFlex which got me started on programming.

And last but not least I thank my lovely husband Raphael for his everlasting support and for countless discussions about computer science.

Curriculum Vitae



RIA FISCHER

Institute of Geophysics – ETH Zurich
Sonneggstrasse 5 – 8092 Zürich – Switzerland
phone: +41 44 633 32 48 – mail: ria.fischer@erdw.ethz.ch
web: <http://jupiter.ethz.ch/~rfischer/>

EDUCATION

<i>Current</i> Nov 2012	Ph.D. student at ETH Zurich , Switzerland Thesis: <i>“From early Earth Plume-lid tectonics to present day Plate tectonics: A high-resolution 3D numerical modelling approach”</i> Advisor: Prof. Dr. Taras GERYA
SEP 2010-SEP 2012	Master of Science ETH in Earth Sciences, ETH Zurich , Switzerland Major: Geophysics Thesis: <i>“Adaptive Multigrid. How to couple Adaptive Mesh Refinement with the Multigrid method and Self-consistent modelling of planetary differentiation and onset of mantle convection on Mars. A comparative study in 2D and 3D”</i> Advisor: Prof. Dr. Taras GERYA
SEP 2007-JUN 2010	Bachelor of Science ETH in Earth Sciences, ETH Zurich , Switzerland Major: Geophysics Thesis: <i>“Pseudo-3D Ground Penetrating Radar imaging of past and present landslides in the Urserental”</i> Advisors: Dr. Stefan CARPENTIER, Dipl.-Geophys. Heinrich HORSTMAYER
SEP 2005-JUN 2007	Bachelor studies in Physics ETH Zurich , Switzerland
AUG 1998-JUL 2004	Eidgenössisches Maturitätszeugnis (Swiss university-entry diploma) Kantonsschule Alpenquai Luzern , Switzerland Major: Physics and Applied Mathematics

PERSONAL DATA

DATE OF BIRTH: 11 July 1985
PLACE OF BIRTH: Zürich ZH, Switzerland
CITIZENSHIP: Switzerland

PROFESSIONAL EXPERIENCE

<i>Current</i>	Scientific Assistant at ETH Zurich , Zurich, Switzerland
Nov 2012	Ph.D. Student in the Geophysical Fluid Dynamics group at Institute of Geophysics
JUL 2002-FEB 2012	Programmer and web developer/designer, P.A.Blackburn AG , Lucerne, Switzerland Implementation and maintenance of customer relationship management application and setup, design and maintenance of company websites including development of corresponding web applications

FIELD EXPERIENCE

20-28 JUL 2014	Geological excursion to Witwatersrand Supergroup and Barberton Greenstone Belt, South Africa Guided by: A. KRÖNER, Beijing SHRIMP Centre, CAGS, Beijing, China A. HOFMANN, University of Johannesburg, South Africa C. HEUBECK, University of Jena, Germany Martin VAN KRANENDONK, University of New South Wales, Sydney, Australia
6-9 SEP 2014	Field trip to Limpopo belt, South Africa Guided by: Prof. Dirk VAN REENEN, Univ. Johannesburg, South Africa

RESEARCH VISITS

22-26 APR 2013	Visit with Prof. Dr. Stéphane LABROSSE to Laboratoire de géologie de Lyon at ENS, Lyons , France
17-19 DEC 2013	Visit with Prof. Dr. Stéphane LABROSSE to Laboratoire de géologie de Lyon at ENS, Lyons , France

PUBLICATIONS

- S. Carpentier, M. Konz, **R. Fischer**, G. Anagnostopoulos, K. Meusburger, and K. Schoeck. Geophysical imaging of shallow subsurface topography and its implication for shallow landslide susceptibility in the Urseren Valley, Switzerland. *Journal of Applied Geophysics*, 83(0):46–56, 2012.
- R. Fischer** and T. Gerya. Regimes of subduction and lithospheric dynamics in the Precambrian: 3D thermomechanical modelling. *Gondwana Research*, 2016a. Submitted for publication.
- R. Fischer** and T. Gerya. Early Earth plume-lid tectonics: A high-resolution 3D numerical modelling approach. *Journal of Geodynamics*, 2016b. In press.
-

CONFERENCES ATTENDED

- R. Fischer** and T. Gerya. Self-consistent modelling of planetary differentiation and onset of mantle convection on Mars. A comparative study in 2D and 3D. In *10th Swiss Geoscience Meeting*, 2012. Oral contribution.
- R. Fischer** and T. Gerya. Was plate tectonics different in a hotter Earth? – 3D numerical modelling of Precambrian tectonics. In *Crystal2Plate 4th workshop*, 2013a. Poster contribution.
- R. Fischer** and T. Gerya. History and evolution of Subduction in the Precambrium. In *LUCKY13: XIII International Workshop on Modelling of Mantle and Lithosphere Dynamics*, 2013b. Poster contribution.
- R. Fischer** and T. Gerya. 3D Numerical study of the evolution of Subduction in the Precambrium. In *International Meeting on Precambrian Evolution and Deep Exploration of the continental Lithosphere*, 2013c. Oral contribution.
- R. Fischer** and T. Gerya. Was plate tectonics different in a hotter Earth? – History and evolution of Subduction in the Precambrium. In *11th Swiss Geoscience Meeting*, 2013d. Poster contribution.
- R. Fischer** and T. Gerya. Was plate tectonics different in a hotter Earth? – History and evolution of Subduction in the Precambrium. In *AGU Fall meeting*, 2013e. Poster contribution.
- R. Fischer** and T. Gerya. History and Evolution of Precambrian plate tectonics. In *EGU General Assembly*, 2014a. Poster contribution.
- R. Fischer** and T. Gerya. Evolution of Subduction in the Precambrian and consequences on the formation of continental crust. In *IMA 2014: The 21st General Meeting of the International Mineralogical Association*, 2014b. Poster contribution.
- R. Fischer** and T. Gerya. Early Earth tectonics: A high-resolution 3D numerical modelling approach. In *German Swiss Geodynamics Workshop*, 2014c. Oral contribution.
- R. Fischer** and T. Gerya. Early Earth tectonics: A high-resolution 3D numerical modelling approach. In *12th Swiss Geoscience Meeting*, 2014d. Poster contribution.
- R. Fischer** and T. Gerya. Early Earth tectonics: A high-resolution 3D numerical modelling approach. In *AGU Fall meeting*, 2014e. Poster contribution.

- R. Fischer** and T. Gerya. Early Earth tectonics: A high-resolution 3D numerical modelling approach. In *EGU General Assembly*, 2015a. Poster contribution.
- R. Fischer** and T. Gerya. Early Earth tectonics: A high-resolution 3D numerical modelling approach. In *GeoBerlin 2015 "DYNAMIC EARTH – from Alfred Wegener to today and beyond"*, 2015b. Oral contribution.
- R. Fischer** and T. Gerya. Early Earth tectonics: A high-resolution 3D numerical modelling approach. In *AGU Fall meeting*, 2015c. Poster contribution.